CRANFIELD UNIVERSITY

NATHAN OWEN

THE INVESTIGATION OF A NON-TRANSITION METAL FLUORIDE AS A CATHODE MATERIAL FOR LITHIUM BATTERIES

SCHOOL OF APPLIED SCIENCES

PhD THESIS

Academic Year: 2009 - 2012

Supervisor: Q Zhang

December 2012

CRANFIELD UNIVERSITY

SCHOOL OF APPLIED SCIENCES

PhD THESIS

Academic Year 2009 - 2012

N OWEN

The investigation of a non-transition metal fluoride as a cathode material for lithium batteries

Supervisor: Q Zhang

December 2012

Abstract

Lithium ion batteries are fast becoming the consumer choice for powering their electronic devices. However, current lithium batteries energy densities are not sufficiently high, and cost per kWh sufficiently low, to be widely accepted as batteries in electric vehicles.

In order to reduce the cost and increase the energy density it may be necessary to move away from intercalation electrode materials, that are limited by the number of vacant lithium interstitial sites available, to conversion reaction materials that can allow multiple electron transfer. This thesis looks to investigate the use of a non-transition metal fluoride as a cathode material in a primary or secondary lithium battery.

Initial results for the ball milled material show specific energy densities over 2050 Wh/kg. The initial energy density rapidly faded over a period of a few cycles due to the structural change of the material and unwanted reactions with the electrolyte. These were identified by investigating the mechanism of the one stage discharge and charge profile. To further improve the cycling results nanorods were synthesised which improved the rate capability to provide an energy density of over 1250 Wh/kg at a discharge rate of 0.25C. The capacity over repeated cycling was also improved but the same problems that plagued the ball milled samples were also apparent in the nanorod samples.

It was found during the initial investigation of the non-transition metal fluoride material that it is rechargeable, but for a limited number of cycles partly due to its poor kinetics. It has the potential to be a good rechargeable battery material but if not can satisfactorily compete with commercial primary batteries in terms of energy density and cost, as it is a very cheap material.

Acknowledgements

For their support during my PhD and their wise words throughout my studies I would like to thank my parents.

For the help with my experimental work and guidance in the development of this thesis I would like to thank my supervisor Dr Qi Zhang.

For their endless time and patience setting up experiments and changing equipment for me I would like to thank Mr Andrew Stallard and Mr Matt Taunt who made my results so much easier to achieve.

Contents

List of Figures

List of Tables

Abbreviations

A	Amperes
Al	Aluminium
AlF_3	Aluminium fluoride
BM	Ball milled powder sample
BM_c	Ball milled powder coated sample
CP	Commercial powder Sample
CV	Cyclic voltammetry
D_{Li}	Lithium diffusion coefficieint
e^-	Electron
E	Potential
EDX	Energy dispersive X-ray
EIS	Electrochemical impedance spectroscopy
F	Fraday constant
FT-IR	Fourier transform infra red spectroscopy
g	gram
h	hours
HRTEM	High resolution TEM
IHP	Inner helmholtz plane
IPA	Isopropanol
J	Joules
kg	kilogram

kJ	kilojoules
Li	Lithium
LiF	Lithium fluoride
mA	miliamp
mV	milivolt
M_w	Molecular weight
NC	Nanocomposite sample
NHE	Normal hydrogen electrode
NR	Nanorod sample
NR_c	Nanorod coated sample
NTA	Nanoparticle tracking analysis
OHP	Outer helmholtz plane
PVDF	Polyvinylidene fluoride
SAED	Selected area electron diffraction
SEI	Solid electrolyte interphase
SEM	Scanning electron microscope
SOC	State of charge
TEM	Tunnelling electron microscope
V	Volt
V_m	Molecular volume
W	Watts
Wh	Watt hours
XRD	X-ray diffraction

Chapter 1

Introduction

This thesis represents the work carried out to investigate whether aluminium fluoride is a suitable cathode material for use in lithium and lithium ion batteries. It will start off with an introduction to lithium batteries, their applications, current problems and limitations and which ones this project looks at solving. The subsequent parts of the thesis look at how the problems are tackled.

1.1 Background

The search for bigger, faster, longer lasting and more powerful portable consumer electronics over the last few decades has resulted in intense research in battery technology, in particular lithium batteries due to their high energy density as seen in Figure 1.1.

A battery is a device that can convert chemical energy into electrical energy, depending on the type of battery the electrical energy can then be converted back to chemical energy. The battery is made up of a number of electrochemical cells which store the materials that create the chemical energy. A rechargeable electrochemical

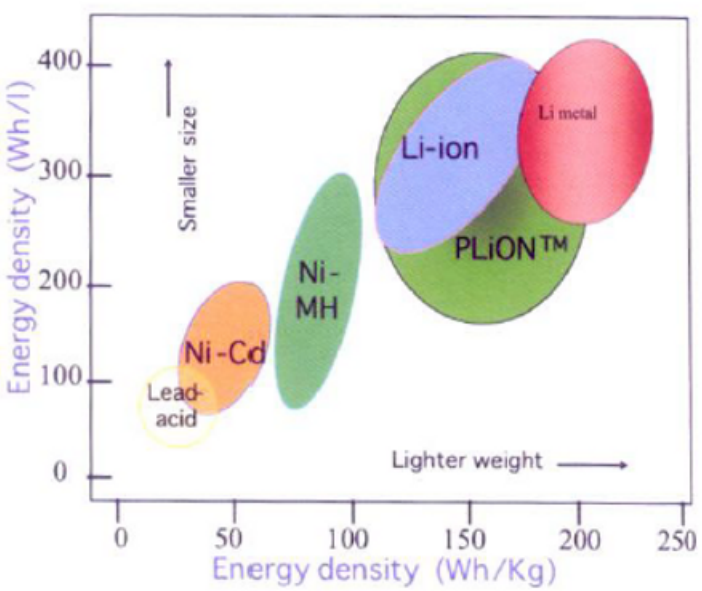

Figure 1.1: A Ragone plot of lithium ion batteries compared to other battery technologies [1].

cell is not only able to convert the chemical energy into electrical energy it is able to convert electrical energy into chemical energy. Primary electrochemical cells can only convert the chemical energy into electrical energy.

There are a number of electrochemical cell technologies such as nickel cadmium, lead acid, nickel zinc and lithium which all have different internal working mechanisms on how the chemical energy is generated. However the basic principle is that there are two electrodes separated by an electrolyte. A redox reaction occurs at each electrode, one electrode oxidises and the other reduces releasing electrons which migrate round the connected circuit to conserve charge neutrality and power the attached device.

There is an abundance of literature on the different cell technologies which will not be discussed in this thesis, however, Table 1.1 shows a brief comparison with a number of those different battery technologies with respect to their theoretical

capacity and energy.

Table 1.1: Comparison of the theoretical electrochemical properties of different battery systems [2].

Battery System	Negative electrode (anode)	Positive electrode (cathode)	Open circuit voltage of reaction (V)	Theoretical capacity (Ah/kg)	Theoretical specific energy (Wh/kg)
Lead-acid	Pb	PbO_2	2.1	83	171
Nickel-cadmium	Cd	NiOOH	1.35	162	219
Nickel-metal hydride	Metal hydride alloy	NiOOH	1.35	178	240
Sodium-sulfur	Na	S	1.78 - 2.1	377	754
Sodium-metal chloride	Na	$NiCl_2$	2.58	305	787
Lithium ion	Li_xC_6	$Li_{1-x}CoO_2$	3.0 - 4.2	79	316
Lithium-polymer	Li	VO_x	2.0 - 3.0	340	884

A lithium primary battery is a battery that uses metallic lithium as the anode and another material as the cathode. The chemical reaction that occurs to reduce the cathode is one that is not reversible and so only allows the battery to be used once.

A lithium ion battery is a rechargeable secondary battery as opposed to a primary battery that can only be used once.

Current typical lithium ion batteries consist of a graphite anode, a lithium metal oxide cathode and an electrolyte soaked separator, which is usually a lithium salt in an organic solvent. The electrodes are mixed with a binder, conductive additives such as Super P, a solvent and then spread onto a current collector. The conductive additives are used to enhance electrical contact between the electrode particles and the binder is used to increase adhesion between the electrode components. The electrolyte and porous plastic film separator act as an electrical insulator while allowing ion flow [3].

When an electrical conductor connects the anode and cathode there is a flow of electrons due to a potential difference between the electrodes, resulting in a current flow from the cathode to the anode. The electrons flow in the opposite direction to the external current. They flow from the anode through the electrical circuit into the cathode. In order to conserve charge neutrality within the cell there has to be a flow

of cations. This is the flow of Lithium ions from the anode to the cathode through the electrolyte soaked separator. During charging a current is passed through the cell in the direction of anode to cathode. As the electrons flow in the opposite direction of the applied current they move from the cathode to the anode. As charge neutrality has to be conserved lithium ions flow through the separator and into the anode. The lithium ions always flow in the same direction as the electrons. Figure 1.2 shows the workings of a lithium ion battery.

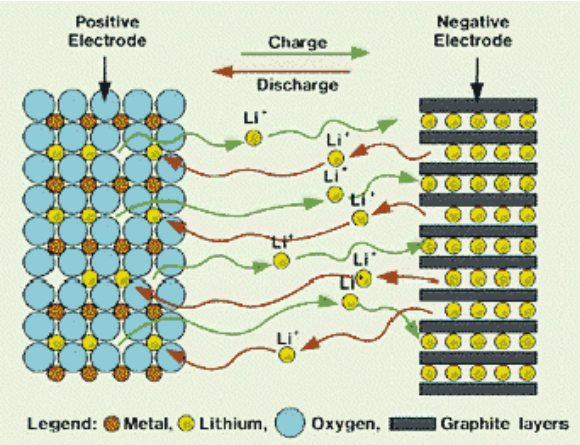

Figure 1.2: A diagram to show the workings of a lithium ion battery [4].

The anode and cathode materials are chosen so that the cell voltage is maximised. The cell voltage is calculated by the difference between the electrode potentials of the cathode and anode. The electrode potential of a material is its tendency to donate or accept electrons. When the battery is placed in an external circuit the anode undergoes oxidisation where it loses electrons. At the same time as losing electrons it creates cations. These cations and electrons meet at the cathode where they undergo reduction. Over time the chemical processes occurring in the cell causes an overconcentration of electrolyte on or near the electrodes as well as corroding the electrodes resulting in a depletion of active material, which reduces the energy of the cell, causing it to eventually become unusable.

The characteristics of the cell are determined by the intrinsic properties of each

of the anode, cathode and electrolyte. The cell potential, the capacity of the cell and the energy density are related to the materials of the electrodes. The cycle-life and lifetime are related to the interfaces between the electrodes and electrolyte [5]. Safety is related to the stability of the electrode materials and interfaces during the charge and discharge process. The power density is related to the materials and the interfaces.

The capacity determines the amount of current that the cell can produce in a given time and is related to the amount of lithium that can be reversibly intercalated. The capacity can only be increased to the theoretical capacity of the material being used and it is the cathode material which is the limiting factor in terms of energy density. This is because current cathode materials such as lithium iron phosphate ($LiFePO_4$) have only limited number of lithium vacancies that can be intercalated into. Increasing the number of lithium ions that can be transferred can increase the capacity. The power density or rate capability is determined by the interface between the electrode material and the electrolyte. A solid electrolyte interphase layer forms and it is the diffusion of ions through this layer that limits the rate capability of the battery.

Lithium and lithium ion batteries are used in a wide range of technological applications from ones that use low current such as laptops, music players, phones, watches etc to the applications that need high currents, hybrid and electric cars, power tools and some military applications. This large market has intensified the research in this area. For low current applications the goal for the battery is to have a high energy density on one charge and then be able to recharge a number of times without losing run time. It is not a necessity but an advantage if the battery can be charged in the shortest time possible. For high current applications it is a necessity that the power density of the battery is high. As well as the power density being high it is desirable for the energy density to be high and in the case for rechargeable batteries

need to be recharged quickly and recharged a large number of times.

1.2 Current Challenges

The challenges of current research in lithium batteries are based on their applications. Each field requires different specifications that the battery needs to fulfill for the application it is being used in. However, there are three main areas that if improved would bring great benefits. These areas are; the batteries energy density, power density and cyclability. Whilst these areas are trying to be improved it is necessary to think about the financial and environmental aspects of the battery. There is no point having an extremely high energy and power density battery that can be cycled unlimited times if it is unaffordable and there isn't an abundant supply of the material.

1.2.1 Energy Density

Energy density can be split into volumetric energy density and gravimetric energy density. The gravimetric energy density is the amount of energy per unit mass and the volumetric is the amount of energy per unit volume.

Current gravimetric energy densities of commercial lithium batteries are around the 150Wh/kg mark. This is a low energy density which requires more cells to be used in order to produce a battery with an acceptable performance. In electric vehicles the battery with an energy density of around 150 Wh/kg usually makes up for around 50% of the vehicle mass. It also requires more of the material to be used increasing the cost of the battery. Low energy density materials result in more expensive and heavier batteries. If the energy density could be increased the amount of expensive material used would be less and the mass of the vehicle (or any other application

it may be used for) could be reduced, reducing cost. The energy density can be increased by either a material with a high specific capacity of mAh/g or a high voltage, as energy density is the product of voltage and capacity.

1.2.2 Power Density

The power density of current commercial batteries allows full charge in a few hours and a partial charge in around 10 minutes, enough to get you to the nearest point where you can charge your battery for a full charge. The main sticking point for the power density is the consumers acceptance of a reasonable charge rate. The ease of filling up a petrol or diesel car in a matter of a few minutes and traveling the same distance again is what power density rates need to achieve. If consumers can only fully charge their battery overnight they will not be accepted by the majority. The low power density results in less acceptance of electric vehicles and is one of the main reason behind them not being as successful as they should be.

1.2.3 Cyclability

The cyclability of the battery is important as it determines the amount of servicing and replacing the battery pack will need. As the battery pack is nearly 50% of the vehicle mass it is not a cheap easily replaceable unit and needs to be operating at full capacity for as long as possible. The longer the battery can be charged and discharged for without losing functionality the cheaper it will be for the consumer and the more acceptable it will be.

1.3 Aims and Objectives

This leads onto the current aims and objectives of this thesis. The idea is to fabricate a positive electrode or cathode material that has an improved energy density with satisfactory power density and cyclability to show that there is a proof of concept, in order for further work to improve the material. Metal fluorides have been chosen as they have a higher energy density than current commercialised materials, due to their low atomic weight and high conversion reaction. If the power density and cyclability is perfected it could open up a use in electric vehicles and a provide them with a new acceptance as the ranges would be comparable to vehicles that use combustion engines. It is the theoretical possibilities of metal fluorides, their cheap price, environmental stability at low temperatures that made them appealing for high energy applications. The metal fluoride batteries may be able to utilise carbon anodes in order to save on cost and improve safety.

1.3.1 Aim

The aim of this project is to develop a material that has a higher energy density than currently commercialised cathode materials, with the potential of having a high power density and long cycle life.

1.3.2 Objectives

In order to fulfill the aim the following objectives will need to be met:

1. Fabricate a cathode material that has a specific energy density higher than 850 Wh/kg for at least one discharge charge cycle.

   Current commercialised cathode materials are based on the intercalation mech-

anism and have maximum energy densities of 850 Wh/kg (VO_x cathode in lithium polymer battery [2]). The energy density is the product of cell voltage and electrode capacity. As it is a proof of concept stage the objective is to see if the suggested material has an experimental energy density close to its theoretical energy density.

2. Fabricate a cathode material that can be discharged in less than 20 hours and charged within 100 hours with an 85% capacity on the second discharge.

   The power density is the rate at which the battery can be charged and discharged. A high power density would allow the battery to be charged quickly and reduce the need for long overnight charges. However, for a new material at the proof of concept stage an acceptable discharge rate is 20 hours, this is enough to show that the intrinsic material kinetics are sufficient to provide a respectable discharge capacity. For charge rates to ensure full redox reactions occur a slower charge rate is defined in order to prove the concept.

3. Fabricate a cathode material that can be charged and discharged over 10 cycles at a discharge rate of 0.05C and charge rate of 0.01C without losing more than 60% of the initial capacity.

   The lifetime of a battery is determined by the number of charge/discharge cycles. For a new material and proof of concept this is an acceptable objective. It would then need further work to improve on but the proof of concept is there.

1.4 Report Organisation

This report comprises of nine chapters excluding the introduction and will be as follows.

- Literature Review

- Metal Fluorides as Cathode Materials for Lithium Batteries
- Experimental Methods
- Aluminium Fluoride as a Novel High Capacity Cathode Material
- Investigation of the Redox Reaction of Aluminium Fluoride
- A Facile Synthesis of Aluminium Fluoride Nanorods
- Aluminium Fluoride Nanorods as an Improved High Capacity Cathode Material for Lithium Batteries
- Discussion
- Conclusion

The thesis will report the research undertaken and the results of this project. Chapter 2 will review current state of the art research on the problems addressed in the introduction, mainly, energy density, power density and cyclability. Chapter 3 will specifically address metal fluoride materials used as cathode materials and chapter 4 will explain the experimental methods used to analyse the recorded results. The final chapters will concentrate on the results generated and analysed followed by future work and ideas on how the project can be taken forward.

Chapter 2

Literature Review

This chapter describes current state of the art research in the three main areas described in the introduction, energy density, power density and cyclability, with respect to positive electrode materials. It will describe the theory behind each area, current issues that can be dealt with and possible solutions whilst taking into consideration the scalability, economical viability and the environmental suitability of the proposed process.

2.1 Energy Density

The gravimetric or volumetric energy density is defined as in chapter 1.1. It is equal to the product of the cell voltage and the specific capacity. The voltage of the cell is directly related to the chemistry of the materials and the chemical potential difference of lithium between the electrode materials. The negative electrode, usually graphite, lithium metal or a lithium alloy is where the lithium ions reside at high chemical potentials, where μ^{anode} (μ^a) is the electrochemical potential of the anode and $\mu^{cathode}$ (μ^c) is the electrochemical potential of the cathode [6]. The positive electrode is chosen so that it has a low chemical potential that can host the lithium

ions. The operating voltage can be calculated from the electrochemical series and equation 2.1, n is the number of moles of reaction and F is the Faraday constant.

$$E_{cell} = -\frac{\mu^c - \mu^a}{nF} \tag{2.1}$$

So by using the electrochemical series one can calculate an operating voltage that is suitable for batteries. However, the type of electrolyte must be taken into consideration and the highest occupied molecular orbital (HOMO) of the electrolyte. This is because if the positive electrode lies below the highest occupied molecular orbital of an organic solvent used in electrolytes, oxidation occurs on the surface of the material. This is due to the transfer of electrons from the electrolyte HOMO to the material [7]. This transfer of electrons results in a formation of an SEI layer that becomes severe and aggressive. The electrolyte and material then degrades causing a loss in capacity and columbic efficiency during cycling.

The specific capacity of the electrode material can be calculated using equation 2.2 [6].

$$\text{Specific Capacity } = \frac{\Delta x F}{M} \times \frac{1000}{3600} \text{ (mAh/g)} \tag{2.2}$$

where Δx is the number of moles that can participate in the electrochemical reaction. F is the Faraday constant and M is the molar mass of the electrode compound. Depending on the type of reaction taking place, intercalation or conversion Δx indicates how much lithium ions can be reversibly charged into the host structure without change in the voltage window. It depends on the crystal structure of the material and the number and size of empty interstitial sites.

There are three types of mechanisms that effect the number of lithium ions that can participate and hence provide the specific capacity of the material, these mech-

anisms are the insertion, conversion and lithium alloying mechanism. However, the only mechanisms that this thesis will be concerned with the insertion and conversion mechanisms as they are the only ones applicable to cathode materials. The lithium alloying mechanism occurs at low voltages, which are only relevant to anode materials. Table 2.1 shows a comparison of energy densities of some insertion and conversion materials.

Table 2.1: Cathode materials that are entering commercial production or undergoing intensive research for electric vehicles. The range of experimental results is given for each category.

Material	Mechanism	Capacity (mAh/g)	Voltage Potential vs Lithium (V)	Energy density (Wh/kg)
Layered	Intercalation	140 - 160	3.6 - 4.2	500 - 650
Spinel	Intercalation	140 - 160	4.0 - 5.0	600 - 700
Olivine	Intercalation	150 - 170	3.2 - 5.1	500 - 850
Other	Intercalation	150 - 400	2.8 - 3.8	420 - 1520
Metal fluoride	Conversion	500 - 950	1.4 - 2.7	700 - 2000
Sulfur	Conversion	1675	2.1	3517
Air	Conversion	1790	2.91	5209

2.1.1 Insertion Mechanism

In order to maximise the energy density of a battery we are looking for a material which has a large number of electrons transferred per mole of reaction and a low molecular mass, and/or a high operating voltage. The number of electrons that can be transferred per mole of reaction is limited by the number of ions that can also be transferred in order to conserve charge neutrality. For an insertion compound the material has a particular structure where lithium ions can insert themselves into unoccupied sites depending on the structure of the material. The benefit of the insertion compounds is that there is no real structural change when the lithium ions are inserted or removed from the material. However, the capacity of an insertion compound is limited by the concentration of Li that can be inserted reversibly [8]. The main issue with intercalation compounds are the low energy densities. The

insertion mechanism follows equation 2.3.

$$\mathrm{xLi} + \mathrm{MX}_y \Leftrightarrow Li_x MX_y \tag{2.3}$$

The following are some examples of the more researched insertion materials and the structures they form. Doping these materials with other materials allow infinite different combinations to be made, some which may have more useful properties than others.

Layered Oxides

Layered oxides come in the form of $\mathrm{LiMO_2}$ where M is usually a transition metal. The cathode half reaction takes the form of:

$$LiMO_2 \rightleftharpoons Li_{1-x}MO_2 + xLi^+ + xe^- \tag{2.4}$$

They typically have alternating layers (111) of lithium $\mathrm{Li^+}$ and transition metal $\mathrm{M^{3+}}$ ions which occupy octahedral sites in a distorted cubic close-packed oxygen ion lattice, resulting in a layer sequence of O-Li-O-M-O along the c-axis as in Figure 2.1 [10]. This rock salt structure framework provides a two-dimensional interstitial space where lithium ions can be extracted and inserted easily. The lithium ion sites are connected through $\mathrm{LiO_6}$ octahedral which edge share and lie between the $\mathrm{MO_2}$ layers. This provides a high conductivity of the lithium ions. As the edge-shared $\mathrm{MO_6}$ octahedral has a direct M-M interaction a high electronic conductivity can be achieved. These properties of the layered structure made it the first commercialised lithium ion battery [11]. However, The $\mathrm{LiMO_2}$ compounds can sometimes show non-stoichiometry which occurs due to there being excessive amounts of transition metal M. The transition metal cations occupy the same structural sites as the lithium ions

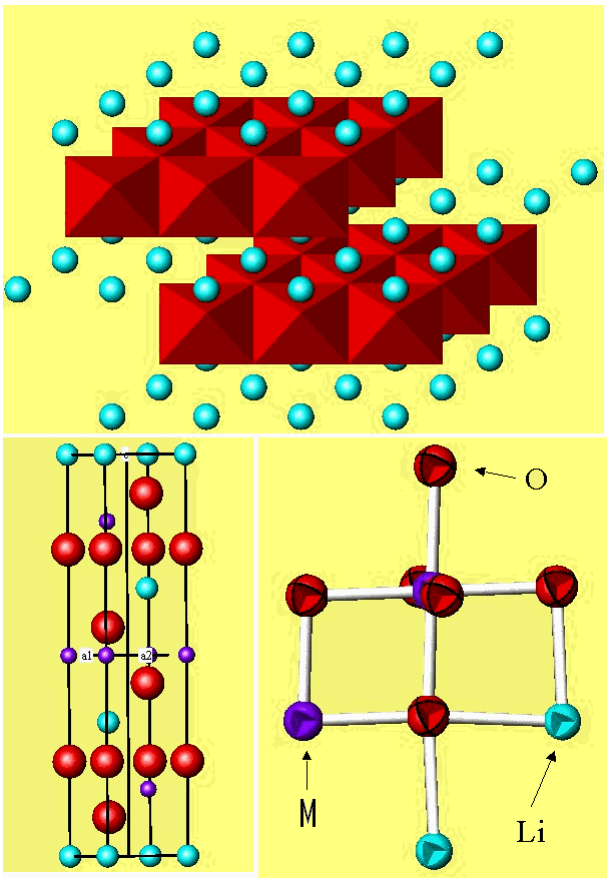

Figure 2.1: The structure of the layered oxide $LiMO_2$ where M is a transition metal [9].

and the specific capacity and electrochemical performance is reduced. It requires great care when being synthesised as to keep this effect minimal. Some examples of layered oxides are $LiCoO_2$ and $LiNiO_2$.

Olivines

Olivines take the form of $LiMPO_4$ where M is usually a transition metal. The cathode half reaction is:

$$LiMPO_4 \rightleftharpoons Li_{1-x}MPO_4 + xLi^+ + xe^- \tag{2.5}$$

The olivine structure is orthorhombic with space group *Pnma*. It has PO_4 tetrahe-

dra with M^{2+} ions on corner sharing octahedral positions and the Li^{+} ions occupy the edge sharing octahedral position, which form one-dimensional chains along the (010).

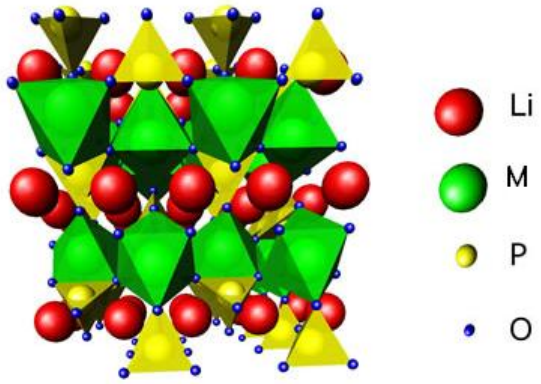

Figure 2.2: The structure of the Olivine $LiMPO_4$ where M is a transition metal [1].

These olivine structures have good thermal stability as the phosphates of the crystal stabilise the whole framework. Even though some types of olivines are in commercial development for next generation electric vehicles, it has a low intrinsic conductivity due to its one dimensional unidirectional tunnel [12]. Some examples of olivine structures are $LiFePO_4$ and $LiMnPO_4$

Spinel Oxides

The spinel structure occurs from oxides with the general structure LiM_2O_4. The Li^{+} and the $M^{3+/4+}$ ions occupy the 8a tetrahedral and 16d octahedral sites of the cubic close packed oxygen array. The Li^{+} ions can be reversible extracted from the tetrahedral sites without collapsing the $[M_2]O_4$ spinel framework due to strong edge-shared octahedral $[M_2]O_4$. Theoretically there is also an empty 16c octahedral site where lithium can be inserted into, but an electrostatic repulsion between the 8a and 16d Li^{+} ions displace the tetrahedral ions into the neighboring empty 16c sites, resulting in an ordered rock salt structure [13]. As in the layered oxides the edge sharing MO_6 octahedral sites with direct M-M contact provides good

electrical conductivity and the interconnected three-dimensional spinel framework provide good lithium ion conductivity. As a result the spinel $LiMn_2O_4$ has been actively researched as a battery for electric vehicles [13]. Some examples of spinels are $LiMn_2O_4$ and $LiNi_{0.5}Mn_{1.5}O_4$.

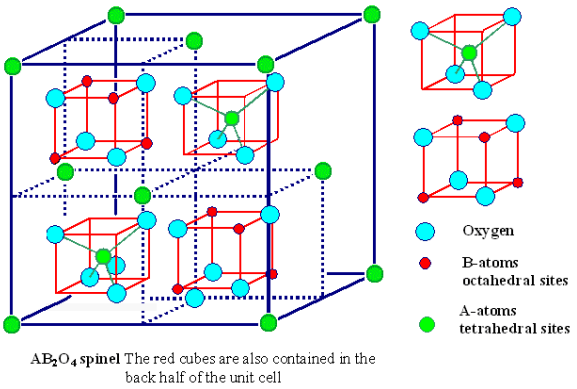

Figure 2.3: The structure of the Spinel LiM_2O_4 where M is a transition metal [14].

2.1.2 Conversion Mechanism

Another type of mechanism is the conversion mechanism. Most positive electrodes are intercalation compounds which retain their crystal structure as the lithium inserts. Although there may be a slight distortion, expansion or contraction depending on whether the lithium is entering or exiting the material the host structure remains intact [15]. Although transition metals which are commonly used in all the intercalation compounds are capable of multiple electron transfer it is the limited lithium vacancies that inhibit the incorporation of more lithium and thus the charge transfer of more electrons to the structure. Also, the covalency of the transition metal dichalcogenide bond reduces the voltage of the reaction. The conversion process enables full utilisation of all the redox potentials of the host metal as it reduces fully to the metallic state. There are a few current technologies that utilise the conversion reaction, lithium sulfur reaction, lithium air and metal fluorides [16]. Figure 2.4 shows the workings of a lithium ion battery involved in a conversion reaction. The

materials separate and a lithium compound is formed along with the other material. Upon charge the lithium ions break from the lithium compound and the two remaining materials react to form the original compound.

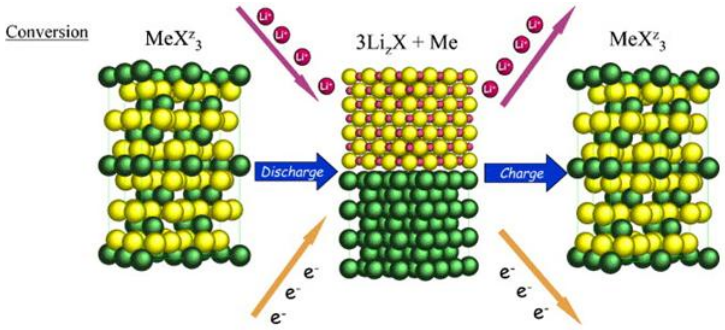

Figure 2.4: A diagram to show the workings of a lithium ion battery involved in a conversion reaction [15].

Lithium Air

The Lithium Air cell is similar to the Li-S cell as it represents a conversion reaction but is based on the reaction of Lithium with Air rather than Sulfur. The average voltage is slightly higher than Li-S but is limited to a one electron reduction per oxygen atom to form Li_2O_2. The reaction is $O_2+2Li^+/2e^- \longleftrightarrow Li_2O_2$. The first non-aqueous air battery was reported by Abraham et al in 1996 [17] but was only later to be found to be rechargeable by Bruce et al [18]. It was determined that Li_2O_2 was the principle product after discharge and O_2 was found as the oxidation product on charge confirming reversibility. The calculated voltage of the lithium air cell is around 2.91V and the capacity is around 1790mAh/g.

The reaction at the positive electrode employs porous carbon or porous metal as the current delivery system for O_2 reduction and as host for the product [19]. When discharging, the reaction fills the voids with Li_2O_2 and terminates when the voids are full. The intermediate super oxide is insoluble and doesn't react with the electrolyte or the surface of the electrodes. However, the Li_2O_2 reaction requires a catalyst and the triple phase boundary governs reactivity which is determined by the necessity

of simultaneous contact of the electron delivery network; the reactants O_2 and Li^+ via the electrolyte and the catalyst necessary to act out the redox reaction.

High over potentials along with substantial hysteresis on discharge-charge are observed, with there being recorded results showing a discharge potential between 0.3 - 0.4 volts lower than theoretical and about 1 volt higher when charging. The problem of the catalytic sites being blocked by the formation of Li_2O_2 remains a serious challenge. On reduction, extensive nucleation of the product on the catalyst particle will block further catalytic activity and on oxidation the lack of intimate contact of the Li_2O_2 with the catalyst can inhibit reactivity. Using an aqueous media has circumvented some problems but results in lower voltages and lower volumetric capacity as well as the problem of the extreme reactivity of metallic Li with H_2O which requires a protected Lithium anode that allows air to penetrate.

Figure 2.5 shows the workings of a lithium air cell, where the oxygen reacts with the lithium anode. The lithium ions then travel through the electrolyte and react with a composite porous cathode upon discharging.

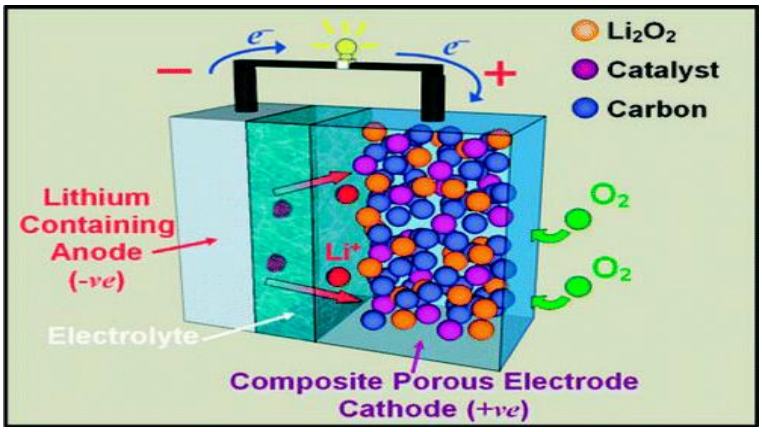

Figure 2.5: Diagramatic representation of a lithium air battery [20].

Due to the highly complex challenges of stopping metallic lithium reacting with the aqueous media whilst being able to contact the air as well as the cost of the catalyst required and the constant clogging of the catalyst has made some research groups move towards a different kind of conversion reaction, the lithium sulfur cell.

Lithium Sulfur

Lithium sulfur cells are attractive because they are low equivalent weight, low cost and high capacity. The sulfur electrode involves a reversible chemical reaction with lithium to form another material. This occurs via a redox cascade of intermediate poly sulfides $Li_2S_8 \longleftrightarrow Li_2S_6 \longleftrightarrow Li_2S_5 \longleftrightarrow Li_2S_4$ followed by the formation of insoluble Li_2S_2 and finally Li_2S [21, 22].The reaction $S_8 + 16Li \longleftrightarrow 8Li_2S$ describes the overall redox couple and lies at an average of 2.1V with respect to Li^+/Li°. This potential is slightly lower than intercalation positive electrodes by about 40% but this is offset by the nontopotactic integration process which results in a high theoretical capacity of 1675mAh/g. This then allows the gravimetric energy density of Li-S batteries to be at least a factor of 3 - 5 times higher than the intercalation positive electrodes. Theoretical values can approach 2500 Wh/kg or 2800 Wh/l [23], assuming complete reaction to Li_2S. The high oxidation states between $S^0 \longleftrightarrow S^{0.5-}$ have fast kinetics in the reaction compared to those of the lower oxidation states. The energy required for nucleation of the solid state phase hinders the reaction of $S^{0.5-} \longleftrightarrow S^{1-}$ to form insoluble Li_2S_2. The sluggishness of the solid state diffusion in the bulk material also impedes the interconversion of Li_2S_2 to Li_2S [24].

The benefits of Li-S cells can only be realised once all the issues that plague the cells have been fixed. The poor electronic conductivity of sulfur and its discharge products is the main problem. Recent progress in improving the conductivity is by enhancing the contact with carbonaceous materials on the nanoscale level, using multi walled carbon nano tubes, however this process is very expensive.

Another major challenge is reducing the solubility of the polysufide ions that are formed on reduction of S_8 or upon oxidation of Li_2S, which escape from the sulfur electrode and enter the electrolyte. These polysulfide ions diffuse to the lithium electrode where they react directly with the lithium and create lower order polysulfides. The new species then diffuse back to the positive electrode and are reoxidised

into the original high order polysulfides. This process continues constantly in the cell and reduces the coulombic efficiency. Impedance also increases as some of the process is irreversible and builds up layers on both electrodes. On the completion of each discharge cycle some of the polysulfides self discharge onto the Li anode and are subjected to deep reduction to form solid Li_2S_2 and/or Li_2S which form a thick layer on the surface, and over prolonged cycling becomes electrochemically inaccessible and cause active mass loss and capacity fading. The deposition on the positive electrode can also block ionic pathways into the parts of the sulfur electrode that impedes further electrochemical reactions.

The most advanced state of Li-S batteries encompass interwoven carbon/sulfur composites that comprise high pore volume carbons with 1D or 3D channel nanostructures [25]. Capillary forces incorporate sulfur from the melt and shrinks upon solidification to provide open pathways for electrolyte/Li^+ ingress as shown in figure 2.6.

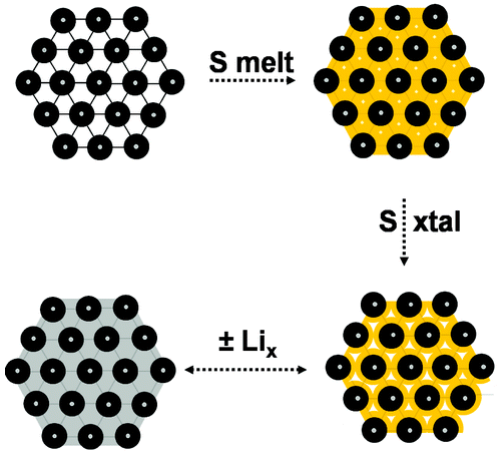

Figure 2.6: Diagram of the sulfur (yellow) confined in the interconnected pore structure of mesoporous carbon. [16].

The conductive carbon framework constrains the sulfur within it's channels and generates essential electrical contact. The polysulfides formed in the redox reaction are trapped in the carbon and are not able to diffuse out of the framework due to the carbons sorbtion properties, full reduction then occurs to Li_2S_2/Li_2S (or oxidation

to S_8 on charge) is achieved within the carbon framework. To further provide a chemical gradient that restricts diffusion of these large anions out of the electrode to facilitate a more complete reaction a polymer modification of the carbon surface has been seen to work. Reversible capacities of around 1320mAh/g have been achieved for the first few cycles indicating a suppression of polysulfide concentration in the electrolyte [25].

However, due to the cycling problems and the high cost of the synthesis method to incorporate the carbon network the metal fluoride conversion reaction has been studied.

Metal Fluorides

The problems with lithium air and lithium sulfur batteries have required research groups to look for simpler conversion reactions. One such reaction is the conversion mechanism of metal fluorides. The redox potentials approach that of free ions in solution because the transition behaves quasi-ion like as the metal fluoride compounds are highly ionic. The metal fluoride conversion reaction leads to LiF and Me products that are on the scale of 2 - 5 nm [26]. Due to the extremely small diffusion distances between these thermodynamically very stable products, reversibility and thus reformation of the MeF structure can occur on the following charge.

$$x\mathrm{Li}^+ + x\mathrm{e}^- + \mathrm{MeF}_x \longleftrightarrow x\mathrm{LiF} + \mathrm{Me} \tag{2.6}$$

The practical implications of this is a theoretical specific capacity improvement from around 270 mAh/g for $LiCoO_2$ [27] to greater than 700 mAh/g for the reversible conversion metal trifluorides [15]

There has been a number of reversible metal fluorides tested since they have been

identified in the 1970's . NiF_2 was shown to have a limited degree of reversibility but have over 50% utilisation of material and little self discharge during storage. It wasn't until 30 years later that physical proof that fluorides could reversibly convert was demonstrated with TiF_3 [28]. Higher voltage metal fluorides which are usually more insulating were looked at. However due to their insulating nature nanocomposites were fabricated with conductive carbon matrices. These nanocomposites had a relatively low surface area with nano crystalline regions of the metal fluoride encapsulated by an amorphous carbon matrix [26]. FeF_3 was demonstrated to have a reversible capacity of over 600mAh/g. Many of the MeF_3 structures are related to the PdF - ReO structures. They consist of corner shared octahedrons and empty ″A″ sites which means there is little to prevent shearing of the crystal structure leading to a range of crystallographic distortions as one moves from the ReO3 structure to the PdF structure. These structures which consist of corner shared MeF6 octahedrons form vacant octahedral interstices that allow the diffusion of lithium ions. In the light of cation vacancies many MeF_3 have a stage of intercalation. It was later found that the MeF_x compounds supported a $1e^-$ intercalation region followed by the $2e^-$ conversion reaction resulting in equation 2.7 [29].

$$\begin{aligned} &Li^+ + e^- + MeF_3 \longleftrightarrow LiMeF_3, \\ &2Li^+ + 2e^- + LiMeF_3 \longleftrightarrow 3LiF + Me \end{aligned} \tag{2.7}$$

Synthesis of the metal fluoride nanocomposite electrode materials have been reported through a novel mechanochemical induced reaction [30]. Insulating CF_1 and MeF_2 compounds were reacted using high energy milling techniques resulting in a solid state redox reaction. This reaction was induced by the oxidation of the MeF_2 compound to the MeF_3 by the oxidising power of HT CF_1. The resulting product was a fine nanocomposite of MeF3 in a matrix of conducting carbon.

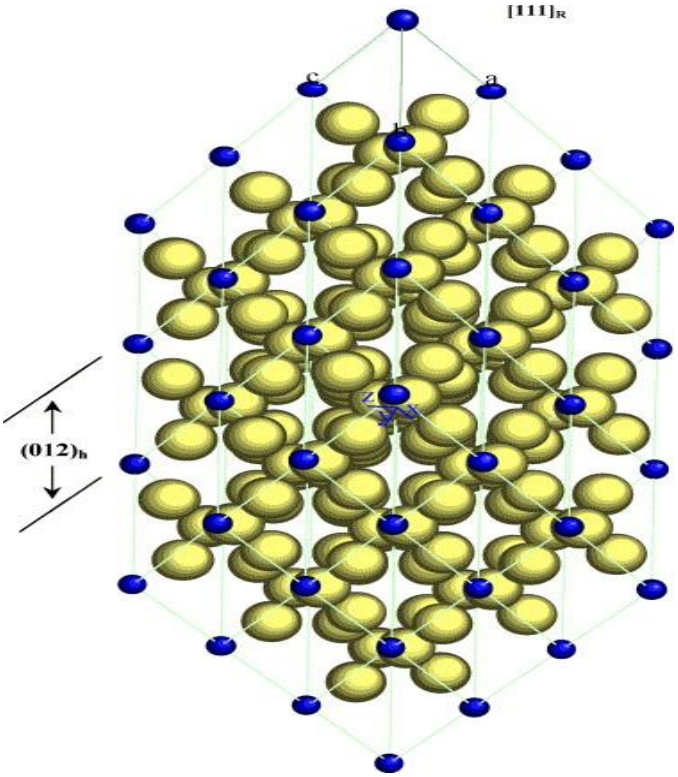

Figure 2.7: Diagram showing the R-3C structure of FeF_3.

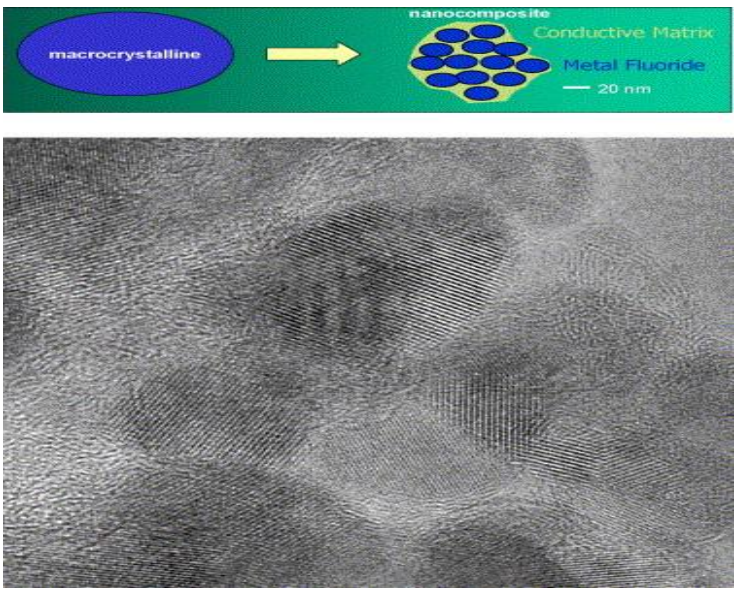

Figure 2.8: HRTEM image of a FeF_2 nanocomposite showing 10 - 20 nm nanocrystallites of FeF_2 in a matrix of amorphous carbon. [15].

$$CF_1 + MeF_2 \longrightarrow C + MeF_3 \tag{2.8}$$

The resulting metal fluoride nanocomposites produced good reversible capacities of around 600mAh/g. This technique worked for all metal fluorides with $Me^{2+} \longrightarrow Me^{3+}$.

Table 2.2: Theoretical average voltage, specific capacity and specific energy density expected during a conversion reaction with Li for a variety of tested divalent and trivalent dichalcodenides and fluorides [15].

$Me^{2+}X$	Voltage (V)	Specific Capacity (mAh/g)	Specific energy density (Wh/kg)
VF_3	1.86	745	1386
V_2O_3	0.95	1073	1014
CrF_3	2.28	738	1683
Cr_2O_3	1.09	1058	1153
MnF_3	2.65	719	1905
Mn_2O_3	1.43	1018	1455
FeF_3	2.74	712	1951
Fe_2O_3	1.63	1007	1641
BiF_3	3.13	302	945
Bi_2O_3	2.17	345	749

2.2 Power Density

The power density is defined as the battery power per unit weight (W/kg). It is the energy density divided by the time it takes to discharge the cell. The power density is reliant on the kinetics of the electrode materials and is poor in many materials due to slow lithium ion and electron diffusion.

The power density of an electrode is governed by mainly four primary resistances:

1. Ionic transport in the electrolyte.
2. Ionic transport in the electrode.
3. Electrochemical reactions in the electrode.

4. Electron conduction in the electrode.

Out of the resistances the only one that doesn't concern the electrode material is item 1. The others can be reduced by improving the material that is being used.

2.2.1 Polarisation

The four primary resistances cause polarisation in the cell. The polarisation of a cell is the amount by which the voltage of a cell when delivering a current deviates from its equilibrium value. The polarisation voltage, E_{pol} associated with two principle causes, ohmic and electrode losses [10], is shown in Equation 2.9 for cell discharge. During cell charge the potential is shown in Equation 2.10 where E_t is the thermodynamic voltage:

$$E_{cell} = E_t - E_{pol} \tag{2.9}$$

$$E_{cell} = E_t + E_{pol} \tag{2.10}$$

Ohmic

This is the total internal resistance of the bulk phases within the cell and the contributors are shown in Table 2.3. Theoretically if the current distribution is uniform the ohmic potential E_{ohmic} is the total of a current i through a cell with j sequential phases as in Equation 2.11, where x is the thickness of the phase, A is its cross-sectional area and σ is the conductance:

$$E_{ohm} = i \sum_{j} (x_j / A_j \sigma_j) \tag{2.11}$$

However, through all the phases the current distribution is not usually uniform and requires complex calculations of cell geometry and the characteristics of the electrode surface. It is possible to determine an experimental average but usually it is difficult to distinguish between ohmic and electrode polarisation.

Table 2.3: Table to show the internal resistance contributions of a cell taken from [12].

Type of Resistance	Internal resistance of cell (R_i = ionic resistance + electrical resistance + interfacial resistance)
Ionic	Electrode (cathode and anode) particle
	Electrolyte
Electrical	Electrode (cathode and anode) particle
	Conductive additives
	Percolation network of additives in electrode
	Current collectors
	Electrical taps
Interfacial	Between electrolyte and electrodes
	Between electrode particles and conductive additives
	Between electrode and current collector
	Between conductive additives and current collector

Electrode losses

The electrode losses include the activation and concentration overpotentials. Activation polarisation or activation overpotential is caused by the potential determining ions being inhabited to pass through the electrode electrolyte phase boundary. Polarisation at low current densities is due to this activation overpotential. The formation of a foreign substance on the electrode surface consisting of electrolyte anions and cations, oxides or hydroxides or other organic or inorganic electrolyte component causes the electrode to become passive and increases the resistance. If the situation where ionic transfer through the electrode electrolyte interface is possible, but the movement of electrons is not, the magnitude and direction of current at an electrode with the deviation from the equilibrium potential can be expressed in the Butler-Volmer equation [31]:

$$i = i_0 \left[e^{-\frac{\alpha F \eta_a}{RT}} - e^{\frac{(1-\alpha) F \eta_a}{RT}} \right] \tag{2.12}$$

Where i_0 is the exchange current density, α is the charge transfer coefficient, F is the Faraday constant, R the universal gas constant, T absolute temperature and η_a is the activation overpotential which is defined as electrode potential - equilibrium potential. The activation overpotential is used to overcome the activation energy which is required to drive the surface electrode processes at a current i. In the cases where the electron transfer is slow and where the activation overpotential is small the charge transfer resistance (R_{ct}) can be deduced from Equation 2.13 to give:

$$R_{ct} = \frac{RT}{Fi_o} \tag{2.13}$$

In the other case where η is large, the reaction effectively only occurs in one direction leading to Tafel behaviour, an indicator for totaly irreversible kinetics [32, 33] and the activation overpotential can be written as:

$$\eta_a = \frac{RT}{\alpha} \ln i_0 - \frac{RT}{\alpha F} \ln i \tag{2.14}$$

The concentration overpotential describes the restriction in the current which is a result of concentration changes of the electroactive species at the electrode surfaces. This effect is most important at high current densities. In liquid electrolytes the electroactive molecules or ions supplied to the electrode surface are a result of mass transport through the bulk of the electrolyte phase or by a chemical reaction near the electrode electrolyte interface. The mass transport mechanism is diffusion due to a concentration gradient or migration if there is an electric field present [10]. The reason this only has a real effect at high current densities is that, at high discharge rates, the chemical reaction in the battery proceeds at a faster rate. This faster rate gives less time for the reactants to mix and a concentration gradient arises which results in a greater resistance and greater energy loss. The concentration overpotential can be

written as [33]:

$$\eta_c = \frac{RT}{nF} \ln\left(\frac{c_s}{c^b}\right) \tag{2.15}$$

Where R, T, n and F have the same meanings as described earlier, c_s is the concentration of the active ion at the surface and c^b is the concentration of the active ion within the electrolyte.

Figure 2.9 shows the polarisation attributed to activation and concentration overvoltage in a cell. The ohmic drop across the cell can be minimised by selecting highly conductive electrolytes and by fabricating cells that have minimal inter-electrode separation. The lowering of the overpotentials can be achieved by designing electrodes that minimises diffusion distances and maximises the surface area in contact with the electrolyte.

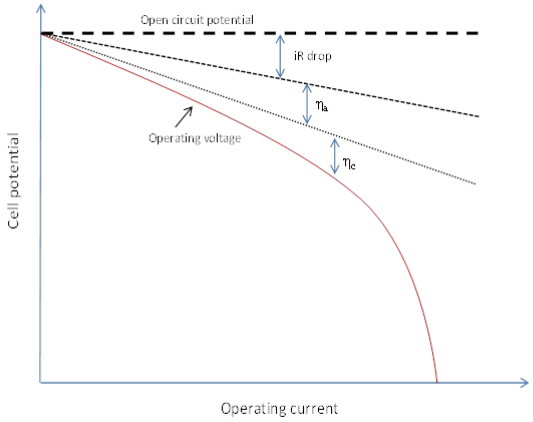

Figure 2.9: Polarisation in a galvanic cell indicating the activation overvoltage η_a, concentration overvoltage η_c and the ohmic drop iR [34].

Equation 2.16 shows the relation of mean diffusion time τ_{eq} of Li^+ with diffusion coefficient D and diffusion length L [35].

$$\tau_{eq} = \frac{L^2}{2D} \tag{2.16}$$

One approach is to decrease L. This is possible by the nanostructuring of the electrode materials [36]. This is because at high discharge rates, high insertion flux density and slow transport result in the polarization within the electrode material. The cell voltage drops and this results in termination of the discharge before the maximum capacity of the electrode material is used. By keeping the mass constant and decreasing the diffusion distance increases the surface area of the electrode and lowers current density. The result is a delay of polarization within the electrode material at higher current values and increased electrode rate capability [37].

The use of nanostructures has given rise to low diffusion lengths and high surface areas so that capacities close to theoretical and increased rate capability can be seen. There are a number of advantages of nanomaterials for lithium ion batteries [38, 39, 40, 41].

1. The reduced dimension allows for the lithium ions to travel shorter distances improving the rate of lithium insertion and removal.

2. Electron transport is also improved due to the same mechanics of lithium ion transport.

3. High lithium ion flux across the electrode electrolyte interface can be achieved due to high surface area allowing high contact area with electrolyte resulting in a larger amount of ions moving in the same distance in nanosized particles than micrometer sized particles.

4. For intercalation mechanisms the smaller structures do not degrade and collapse when they are subject to repeated cycling where their structure changes due to the removal and insertion of lithium ions.

There is a point however where particles can become too small so other process rather than surface reaction become rate limiting, and the high reactivity can re-

duce stability and safety during long operational lifetimes [42], therefore intermediate particle size may be the most appropriate around 100nm. Of most of the nanostructures it has been shown that the mesoporous micron sized particles perform better than nanoparticles [43]. Particle shape can also improve electrochemical performance. In general rod/needle like particles have shown good performance during cycling and high discharge currents whereas plate like particles seem to accommodate expansion/contraction during intercalation/deintercalation and reduce cracking [44, 45, 46, 47].

Another approach to improving the kinetics of the electrode material is by particle coating. Coatings have been shown to increase power density as the ions can move across the surface and through the material with a lot less resistance [48]. The mechanism is not fully understood but coating with non-conductive material seems to increase cycle life and coating with a conductive species increases material diffusivity [49]. The main substance used to coat is carbon as this improves the conductivity a great deal. A carbon source is usually added to the mixing stage with the precursors and is then burnt off under an inert atmosphere to leave a carbon coating around the particles that had been coated by the carbon source. However, the disadvantage with this is that sometimes it is the agglomerates that are coated and not individual particles. This has moved research onto synthesising carbon nanocomposites with active material [26]. The nanosized crystals have a high total material volume on the surface which contain defects that contribute to enhanced kinetics and the carbon network electrically connects the particles [50]. Instead of each particle or agglomerate being coated, the active material particles are embedded within a carbon composite.

Lithium ions in insertion electrodes diffuse via an interstitial mechanism and the motion of the ions is strongly impeded by the potential created by neighboring ions [12]. Doping the material with suitable ions could decrease the potential and

increase the diffusion coefficient. When doping the material care would need to be taken in deciding which materials are compatible to the material being doped. The idea is to reduce the valent states of the electron and reduce the energy band gap to decrease the energy required to free an outershell electron to become a mobile charge carrier and make the material more conductive.

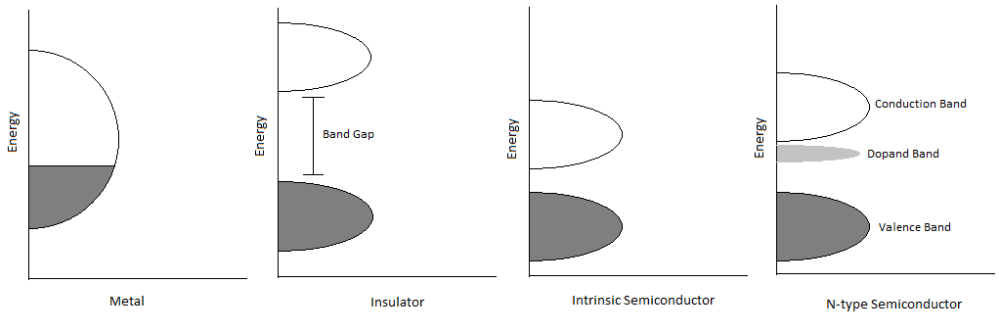

Figure 2.10: A simplified diagram of an energy band gap diagram for a conductor, insulator, semiconductor and a doped semiconductor.

In conversion electrodes it is the M_nX_m which is electrochemically reduced upon uptake of lithium [51]. Once the material is reduced the material converts to form a different compound. The effect of doping the material may improve the structural stability upon reduction and would increase the electronic conductivity of the material.

A recent line of research has focused on not only improving the electrode kinetics but also the kinetics of the current collector. As the current collector is highly conductive and a large part of the cell that is in contact with the electrode material it is only practical to improve this interface so that the electrons can diffuse more quickly to the material.

A novel method that has been invented is a three dimensional discontinuous bulk electrode. Common electrodes consist of a metallic current collector where the active material slurry is spread on top. This results in electron diffusion only occuring in two dimensions. The discontinuous electrode has been shown to charge batteries in around 2 minutes, which is a charge rate of around 30C. The electrode provides a

three dimensional interconnected electrolyte filled pore network that enables rapid ion transport, a short solid state diffusion length, a large electrode surface area and high electron conductivity, which results in the high charge rate. The electrode is fabricated by a self assembly technique and electrodeposition. First opal templates are prepared by vertical deposition and is followed by nickel plating of the opal template. The third step is to pulse electropolish nickel inverse opal followed by the pulsed electrodeposition of nickel oxyhdroxide and manganese oxide depending on what type of battery is being used, nickel metal hydride of Lithium Manganese oxide. Figure 3.2 shows the discontinuous battery electrode [52].

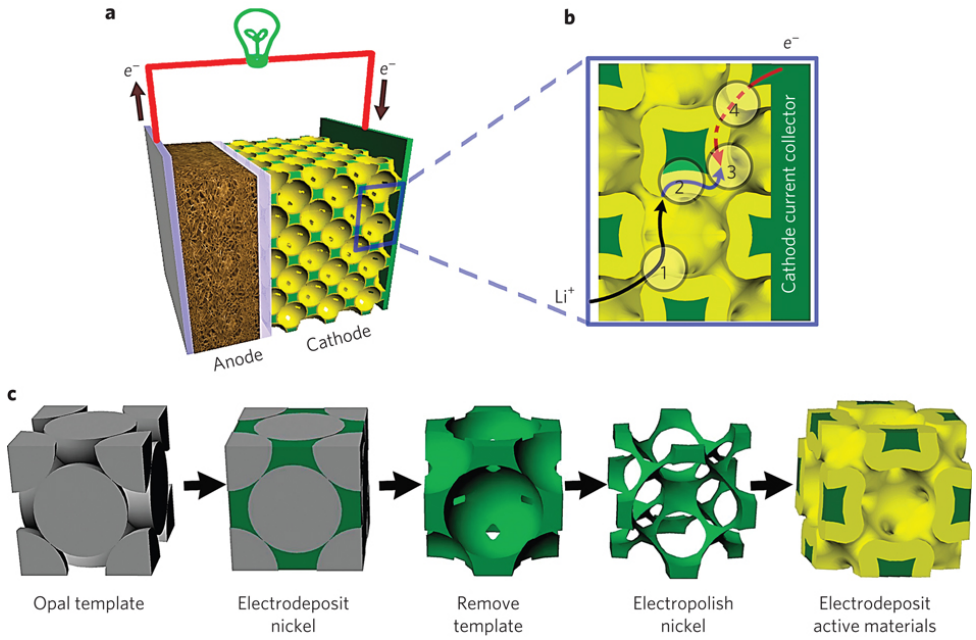

Figure 2.11: Diagram of a battery containing a bicontinuous cathode (a). Illustration of the four primary resistances in a battery electrode (b). Bicontinuous electrode fabrication process (c). The electrolytically active phase is yellow and the porous metal current collector is green. The electrolyte fills the remaining pores [52].

2.3 Cyclability

During the lifetime of lithium batteries reactions take place between the electrolyte and the electrode materials. There are many factors that determine the cycle life

of the cell. The stability of the electrolyte, the strucutral stability of the electrode and the formation of a stable solid electrolyte interphase (SEI) layer that helps to protect the electrode material from uneccessary electrolyte reaction. These factors can reduce the amount of electrode material which then reduces the amount of lithium ions that can be stored and thus reduces the capacity (energy density) of the battery. The main idea to reduce the effect of capacity fade is to coat the electrode material so that electrode electrolyte reactions do not take place. However, the coating would need to be a good ion and electron conductor in order to keep the power density as high as possible. Another effort to reduce capacity fade is to reduce the impedance in the electrode material and the polarization throughout when a current is applied [36].

Cycle life is also reduced by structural changes that take place during lithiation and delithiation, where impurities can occupy ion sites in the crystal structure. Nanoparticles have critical nucleation radii that are larger than the particle diameter. If nanoparticles have particle radius smaller than the critical nucleation radii then the structural transition can be eliminated. This results in the structural changes being accommodated during lithiation and delithiation and the capacity staying constant [53].

Mesoporous intercalation structures are composed of micron sized particles which contain pores of between 2 and 50nm. Unlike nanoparticles that can become disconnected from one another during lithiation and delithiation as they expand and contract, mesoporous materials are in essence a bulk material which have the same dimensions as nanosized particle cathodes. The porosity of the material permits the electrolyte to flood the particles to ensure a high contact area and facilitates lithium transfer across the interface as well as having short diffusion distances for transport within the walls. It has been shown to have improved capacity and improved capacity retention at high rates [54].

2.4 Electrolyte

When electrodes come into contact with an electrolyte a redox reaction takes place at either electrode. This redox reaction provides the voltage of the cell which is determined by different materials on the standard redox potential list. The electrode which undergoes oxidation loses electrons. The other electrode undergoes reduction and gains electrons. The electrode where oxidation takes place becomes more electropositive and the electrode where reduction takes place becomes more electronegative. The ions in the electrolyte move to neutralise the charge balance. The electrolyte is made of materials that are good ion conductors and poor electron conductors. This relies on a connection being made so that the electrons can move from the more electropositive region to the more electronegative region. The flow of ions through the electrolyte keeps the charge neutral and a current flows. If the electrolyte could conduct electrons then no electrons would flow through the external circuit and no current would flow.

Current lithium ion battery electrolytes are organic liquids made from a lithium salt and organic solvents. The electrolyte needs to be stable in the voltage window of the redox pair of the electrode materials so that when a current is being passed through a cell the voltage that the reactions the redox couple take place at is compatible with the electrolyte. Current organic solvents decompose on the electrodes upon charging so that a solid electrolyte interphase (SEI) layer forms. This SEI layer as explained before is electrically insulating but is conductive for lithium ions. The SEI layer prevents any more electrolyte from decomposing and in some instances increases the stability during structural changes of the electrode material.

Research is intensifying in the field of electrolytes as they play an important part in the safety and performance of lithium ion cells. Currently there are groups looking for high voltage electrolytes that are compatible with some higher voltage cath-

ode materials [6] and ones that want to decrease the safety risks associated with flammable organic solvents. Some of the areas include polymer gel and solid electrolytes, Table 2.4 shows a few properties of common types. Electrolytes can take on many forms depending on the application, such as thin films, solid state and polymer gels. Each one has their own advantages and disadvantages depending on the required application.

Table 2.4: A comparison of voltage windows and ionic conductivities of variety of electrolytes [6].

Type of electrolyte	Example	Ionic conductivity (S/cm)	Electrochemical window vs Lithium (V)		Notes
			Redox	Oxidation	
Liquid Organic	1M $LiPF_6$ in EC:DMC (1:1)	10×10^{-3}	1.3	4.5	Flammable
Ionic Liquids	1M $LiBF_4$ in EMI-BF_4	8×10^{-3}	0.9	5.3	Non Flammable
Polymer	LiTFSI-(PEO/MEEGE)	1×10^{-4}	0	4.7	Flammable
Inorganic solid	$0.05Li_4SiO_4$ + $0.57Li_2S$ + $0.38SiS_4$	1×10^{-3}	0	8	Non Flammable
Ionic liquid and Polymer	1M LiTFSI + P_{13}TFSI+PVdF-HFP	1.8×10^{-4}	0	5.8	Less flammable than Liquid organic

2.4.1 Solid Electrolyte Interphase

When the electrolyte comes into contact with lithium a passivating layer is formed to slow the corrosion of the lithium against the solvent it is thermodynamically unstable towards. This layer is formed instantaneously upon contact of the metal and contains reduction products of the electrolyte component [55]. It has the properties of a highly electronically resistive solid electrolyte and acts as an interphase between the electrolyte and the lithium metal.

This SEI (solid electrolyte interphase) layer forms by three consecutive steps, electron transfer at the metal SEI interface, a migration of cations from one interface to

the other and ion transfer at the solid-electrolyte interphase/solution. The final step was found to be the rate determining step as well as the rate of nucleation being affected by the interfacial resistance. This SEI layer was also found to form on most electrode materials. It is an important factor in lithium batteries as it determines the cycle life, power capability, safety and shelf life of the battery.

Using a lithium metal electrode is significantly different from using a carbon or different metal electrode when it comes to the reversible process in the cell. The metallic lithium negative electrode allows lithium ions to be made available from both the electrode and the electrolyte, however with other types of negative electrodes lithium ions are only available from the electrolyte, which is made from lithium salts dissolved in aprotic, nonaqueous solvents. During the formation of the SEI layer in a rechargeable cell with a carbon or non lithium metal electrode a lithium ion is potentially removed from the electrolyte. In order to maintain charge neutrality an anion must be removed from the electrolyte or the positive electrode must provide another lithium ion to replace the one consumed in the formation of the SEI layer. As an anion cannot be removed from the electrolyte it is the positive electrode that provides the lithium ion. The lithium ions that are provided by the positive electrode can no longer participate in the electrochemical reactions with the positive electrode and results in irreversible capacity loss which often occurs during the first cycle. Using a lithium metal negative electrode results in an excess of lithium ions so no irreversible capacity loss due to SEI formation occurs.

Transition metal layered compounds such as $LiMnO_2$ are often used as positive electrodes in Li-ion cells where the redox potential is between four and five volts vs Li/Li^+. At this voltage an oxidation type reaction occurs on the layered oxide compounds due to the removal of electrons from nonaqueous solvents (oxidative cleavage of organic solvents with ring structures). The positive electrode SEI can also form from the formation of radical species due to the electrolyte solvents or nucleophilic

reactions between the materials in the positive electrode and the electrolyte. This surface film that forms at the positive electrode / electrolyte interface can also determine cycling performance and thermal stability of the cell as the lithium ions must diffuse through this layer which if poorly conducting could become rate limiting [56, 57].

Lithium fluoride, lithium alkyl carbonates and polymeric phases are encountered in the positive electrode SEI layer. The lithium fluoride phase occurs due to fluorinated polyatomic anions such as $LiPF_6$ reacting with trace amounts of water to produce HF which etches the lithiated transition metal oxide phase. The lithium alkyl carbonate is thought to grow on the negative electrode which then via dissolution with the electrolyte is precipitated on the positive electrode if the electrolyte becomes saturated enough. Nucleophilical reactions with the electrophilic moloeculs of the electrolyte may occur with the lithiated transition metal compounds to produce alkly carbonate-like phases such as $LiMO_2$ + EC $\rightarrow$ $MOOCH_2CH_2OCO_2Li$ [56]. Ethylene carbonate (EC) is known to passivate carbonaceous materials in negative electrodes and is a common cyclic organic carbonate solvent found in electrolytes. The alkyl carbonate anions may undergo nucleophilic reactions to produce polycarbonate species on solvent molecules. The polymeric phases can then occur by ring opening of solvent molecules due to radicals being formed. Due to loss of oxygen from the metal oxide the delithiated transition metal oxide can be chemically oxidising toward the electrolyte solvent.

The SEI formed at the negative electrode and the positive electrode are distinctly different as it is the formation of the SEI at the negative electrode (when lithium is not used) which is more responsible for the first cycle capacity loss found in rechargeable cells. Capacity fade over a large number of cycles is more greatly associated with the formation of the SEI layer at the positive electrode due to the different phases that are formed and the rate of lithium ion diffusion through a

polyhetero microphase SEI versus a phase where the polymeric species dominate. The formation processes of the SEI on the positive electrode also intensifies due to prolonged storage and elevated temperatures or both, which results in greater resistance of the SEI contributing to capacity fade.

2.5 Summary

In summary research in cathode materials is based around materials with a high energy density, power density and cyclability. However, in this day and age it is important that the processes involved in manufacturing the material is scalable, economical and the materials used are as environmentally friendly as possible. Regarding the energy density it is important to find a material that has a high specific capacity or a high operating voltage. However, when finding a material with a high operating voltage there are a number of issues regarding electrolyte compatibility that need to be addressed. Many materials that can either intercalate / convert lithium ions in the electrochemical window of between zero and five volts can be used with more common electrolytes for initial research purposes. The voltage of a electrode material can initially be estimated by the Nernst equation, and whilst looking for an initial high capacity electrode the amount of valent states should be taken into account as well as the molar mass.

In improving the power density effort should be made to increase the ionic and electron conductivity of the active material and its surface interaction with the electrode. This is to decrease the four primary resistances that are responsible for low power densities. The increase in ionic and electronic conductivity can come from coating, doping and synthesising small particles of the electrode material. The surface interaction can be achieved by designing a three dimensional high surface area electrode. However, this needs to be balanced so that the cyclability is optimised

with the power density. By increasing the surface area of the electrode material there is a larger risk that more material could dissolute into the electrolyte so the coating would not only need to increase conductivity but acts as a coating to stop dissolution into the electrolyte.

Metal fluorides give a good group of materials to work with in order to find one that has not been studied intensively and has a high energy density. This is due to the large number of electrons that can be transferred compared to intercalation compounds. The next chapter will review work on metal fluorides as cathode materials for lithium batteries.

Chapter 3

Metal Fluorides as Cathode Materials for Lithium Batteries

As the first few chapters of this thesis states the aim is to find a reversible high capacity electrode. The first objective is to find a cathode material that has the potential to deliver a high capacity. This chapter will describe the process and reasoning for trying to develop aluminium fluoride as a novel high capacity cathode material.

3.1 Introduction

Lithium batteries are used in a wide variety of portable applications due to their superior energy density to other battery technologies. However for their acceptance in the use of electric vehicles and to bring down the costs of other consumer electronics their energy density per dollar needs to be increased, which currently stands around $400 per kWh. Figure 3.1 shows the breakdown of costs for a lithium battery. The majority is made up of raw materials and material processing. Those can be further broken down into the costs of the materials and the percentages they make up for

the raw materials. It is the cost of the cathode material that is the most dominant factor. In order to reduce the cost per kWh the cost of the raw materials has to become cheaper, one method is to find a cheaper alternative to current cathode materials.

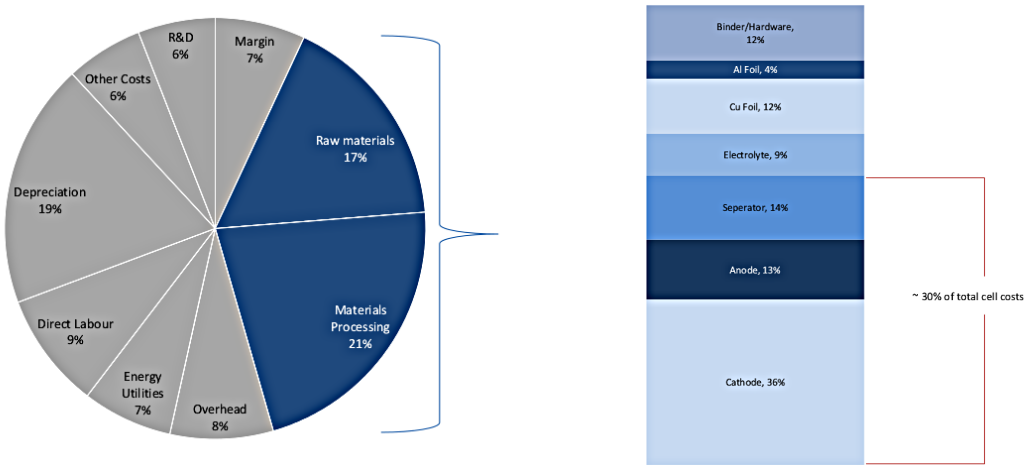

Figure 3.1: The breakdown of the cost of lithium batteries and the cost of the material components [58].

As mentioned earlier current cathode materials look at using the insertion mechanism. This limits the total capacity of the material as it is the amount of vacant lithium sites that can be exploited. Current capacities range from around 150 to 250 mAh/g. This is not enough to reduce the cost per kWh to a consumer accepted value. In order to increase the capacity of the cathode material a different mechanism would have to be utilised. The conversion mechanism as stated before allows the use of all redox states of the host metal until it is reduced to the metallic state. This can achieve capacities up to 1672mAh/g for sulfur.

The electrochemical conversion reaction utilises all the available oxidation states of a high valence metal compound and allows a large specific capacity to be realised.

A number of metal fluorides, oxides, sulfides and nitrides have been shown to follow the electrochemical conversion reaction mechanism.

The strong ionic character of the M-F bond has been of particular interest due to the metallic cations occupying high oxidation states allowing for high specific capacity and the high redox voltage of the fluorine being offset by the low redox voltage of the metal allowing for a voltage suitable for battery applications. The main issue with metal fluorides that has hampered their development is the poor conductivity of the material.

3.2 Early Work

Early work on reversible metal fluorides began with transition metals and a reversible capacity of 80mAh/g was reported for TiF_3 and VF_3 at 2.5V and 2.2V in the late 1990's [59]. It was not until over five years later that a complete reduction was observed at 1 and 0.5V respectively producing a sloping plateau with specific capacity of over 900mAh/g [28]. The analysis showed that the reaction products were amorphous, but crystalline TiF_3 was reformed upon oxidation at 3.5V confirmed via TEM. CrF_3 carbon nanocomposties and MnF_3 have also been electrochemically tested at elevated temperatures and in the case of CrF_3 produced reversible specific capacities of 440mAh/g [30]. MnF_3 was found to produce an initial discharge capacity of 1120 mAh/g but at a voltage of 0.02V with no evidence of a rechargeable capacity.

Nickel and cobalt have also been investigated as reversible conversion electrodes with a disparity of potentials found in NiF_2. Depending on the material preparation discharge voltages range from 0.7V for films prepared via pulsed laser deposition [60] and 2V for NiF_2 carbon nanocomposites [26]. This discrepancy was attributed to the poor electronic conductivity of the ionic compounds. However, the thin films

were capable of producing capacities close to 500mAh/g after 35 cycles despite the over-potential. CoF_2 is also dependant on preparation conditions with 2V discharge plateau being reported for nanocomposite electrodes [61] and 1V reported for thin films [26], again at elevated temperatures of 70°C. CoF_2 was subject to rapid fading upon cycling with reported capacities less than 200mAh/g after eight cycles after producing initial capacities of 600mAh/g [61].

Many research groups reported in the 90s a small reversible capacity of 80mAh/g for FeF_3. The electrochemical reaction of the conversion mechanism was shown by these groups to be very rate and temperature sensitive . This is due to the structural decomposition and reconstruction of the metal fluoride as well as the transport of the lithium ions in the bulk phase. These groups showed that by reducing the size, the lithium pathways are minimised and there is a large area for reversible conversion. In 2003 Amatucci's group ([26]) discovered a way of achieving high capacities at elevated temperatures and low cycling rates by producing a metal fluoride nanocomposite. Upon reduction to 1.5V a plateau was observed at 2V producing capacities of over 770mAh/g. The formation of LiF and Fe was confirmed upon discharge and it was shown that it reconverted to form FeF_3 upon recharging [26, 62]. Thin films have also been produced with no conductive additive and depending on the deposition conditions have produced capacities of over 1000mAh/g in the first cycle, with only 50% capacity retention after repeated cycling [63, 64].

3.3 Critical Inefficiencies

The promise shown by the transition metal fluorides of having a high reversible specific capacity, and a useable working voltage above 2V, are hindered from commercial application due to a number of deficiencies in the conversion mechanism.

The transformation of a metal fluoride into its lithium fluoride and metal product

can also include an intermediate formation. This intermediate formation is a Li-M-F phase that occurs before the transformation takes place. This intermediate formation can result in the metal that is in a high oxidation state to electrochemically react by inserting lithium and reducing it to a lower stable cationic state. This intermediate phase has suggested that the direct conversion to metallic compounds from some binary compounds is not energetically favoured and has a crucial role in the nanostructural formatting of the electrode [65]. In the case of FeF_3 density functional theory calculations suggest that it is more energetically favourable for the formation of $LiFeF_3$ to form from completely reducing the iron into the +2 state, before Fe precipitates out [66]. It has also been recorded that upon conversion to metallic nanoparticles of sizes between 1-10nm there was preservation of the initial particle shape [67].

There is also a problem with the experimental potential being far lower than the theoretical values for many compounds where their is direct conversion to metallic particles. It was initially thought to be due to poor electrode kinetics but tests that improve these by synthesising nanostructures and cycling at elevated temperatures show an increase in cycling capacities at higher rates but not large changes in the overpotential [68]. It is the combination of material crystallinity, surface energy and the diffusion of cations and anions within the binary compound that contribute to the deviations in theoretical potentials [69]. The impact of surface energy is recently being thought to be a major contributing factor to the deviation in experimental and theoretical potentials. The formation of Li_nF/M nanocomposite after electrochemical conversion with Li produces a large contact area interface between a product with a metallic bonding nature and one with an ionic bonding nature. The difference in nature between these two phases results in a large surface/interfacial energy which needs to be overcome for the reconversion reaction to take place. This energy needs to be put into the system and manifests itself in a deviation from the theoretical potential. The surface energy of metals have been recorded as high as

$2J/m^2$ and it is believed the interfacial energy is much higher [70]. Further studies are underway to achieve full understanding in this matter.

Upon oxidation of the Li_nF/M phase there is often a sloping curve that replaces the symmetrically expected plateau noticeable in the reduction reaction. The increased surface area explained earlier is one suspected cause of this discrepancy, as it has been shown in intercalation compounds that the increase in surface sites reacts at slightly different energies to bulk sites [71, 72, 73]. This large surface area is maintained throughout the oxidation process through the generation of the newly formed transition metal fluoride nanoparticles. Another contribution to the difference in discharge and charge profiles is believed to come from the amorphous nature sometimes reported for the Li_nF/M nanocomposite formed at the end of reduction. There is an expected difference between crystalline and amorphous materials equilibrium reaction potential due to the differences in free energy expressed as [74]:

$$\Delta G_j \equiv \Delta_f G_j^0 \quad \text{(amorphous)} \quad -\Delta_f G_j^0 \quad \text{(crystalline)} \tag{3.1}$$

This change in electrochemical profile between oxidation, reduction and the theoretical bulk potential indicates that there is a different dominating factor in the two processes, and induces an overall voltage hysteresis equal to the sum of the change in potential from theoretical potential of the charge and discharge plateaus, resulting in a huge inefficiency. In the particular case of FeF_3 it was discovered that there was a difference in the reaction path upon charge and discharge which are controlled by the very slow iron diffusion within the fluoride lattice. Before being fully reduced to LiF and Fe there would be a formation of $Li_x[Fe^{3+}_{1-x}Fe^{2+}_x]F_3$ and of $Li_{3-3x}Fe_xF_3$ before FeF_3 upon oxidation [75] and both these reactions have different equilibrium potentials which match the experimental data. There is also a need for a large

cut-off potential upon charging that could be even larger due to the thermodynamic values of the reduciton/oxidation of the metals defined by their standard potentials. The fact that the crystalline/amorphous character of the composites do not undergo any significant changes after the first cycle and the voltage hysteresis stays constant with further cycling points to other factors behind the voltage hysteresis, resulting in a need for a renewed focus on the study of these conversion mechanisms to understand this voltage hysteresis, as it is this inefficient cycling that is stopping the application of these materials in a lithium battery.

It has been reported that under 1V there is a similar plateau to the theoretical potential plateau that gives rise to extra charge storage. This extra charge storage has been attributed to electrolyte decomposition [76, 77] and interfacial storage. The electrolyte decomposition can be enhanced by using electrodes made of nanoparticles and can result in some decomposition happening during the voltage plateaus [78] arising from a catalytic effect of the generated metal nanoparticles [79]. The interfacial storage mechanism contributing to extra charge storage is based on the capacitive behaviour of the Li_nF/M interface. Electrons are localised on the metallic side whereas the Li^+ ions are stored on the lithium compound side leading to a charge separation. The interfacial storage is affected by the chemistry of the components and is supported by theoretical calculations.

The Li_nF/M nanocomposite formed upon first discharge is shown to have a high reactivity [28, 65, 75] that results in a large first charge capacity and formation of M_xF_y. This reactive Li_nF/M nanocomposite has been synthesised in the lab but has produced smaller capacities than their electrochemically induced counterparts [80] indicating that the one produced upon discharge is much more efficiently mixed. Even though that a large capacity is recorded on the first charge it is still much lower than the initially discharge resulting in a coulombic efficiency between 80 - 40% for most sample materials [81]. There are some exceptions particularly with FeF_3 which

has a coulombic efficiency higher than 90%, partly down to the upper charge limit of 4V which is believed to suppress these inefficiencies [82]. The coulombic inefficiency is thought to be attributed to; irreversible or non-electrochemical electrolyte decomposition, incomplete oxidation due to the presence of inactive or electrically active disconnected Li_nF/M regions and incomplete reduction of the initial metal fluoride compound. After the first cycle the coulombic efficiencies increase and stabilise, reaching close to 100% in a number of materials [78]. This increase in coulombic efficiency is thought to arise from there being an increase in the material undergoing reduction after the initial conversion into nanoparticles, however, a first cycle capacity loss is still found when the electrode material is already composed of nanoparticles. With also considering all the components of the cell any initial capacity loss due to decomposition of the electrolyte would require the electrolyte to reform back to the initial electrolyte species upon charge, to be reversible as not to reduce the coulombic efficiency, which has not been proven [81].

The cycle life is another obstacle in the way of commercialisation of these types of electrode materials. It is known that the conversion process undergoes structural reorganisation and volumetric changes which can lead to particle isolation and cracking [76, 83] resulting in a capacity fading after a few cycles. In order to counter this structural change strategies from making carbon nanocomposites, increasing the amount of polymeric binder, finding the most suitable polymer binder and performing heat treatments of the composite electrodes before testing have been tried and resulted in increased improvements [84]. The extra carbon used has been credited with improving the electrical conductivity and to inducing a formation of the stable SEI layer that does not change during cycling. The initial metal fluoride has also been synthesised in the nanoscale to offer a shortened diffusion path resulting in increased rate capability and to try and by pass the first cycle textural formatting, however this needs to be fully proved, as it is still thought that particle reorganisation and volume changes would still occur after a number of cycles.

There are also results which show that micron size particles out perform nanoparticles in electrochemical performance [84]. It is also important to consider when using nanoparticles that electrolyte decomposition can be increased which results in a barrier to lithium diffusion, increase particle isolation and thermodynamically enhanced particle dissolution [85]. A new approach many groups are looking at are integrating nanostructured electrodes in which the MF_x compounds are grown on metallic foams and nanopillared and foil substrates [86, 87, 88]. This improves the rate capability and cycling capacity by improving and preserving the substrate material contact. It is crucial that the failure mechanisms upon cycling and electrolyte compatibility are understood in order to assist in the complex reactions that take place in the present phases.

3.4 Solid Electrolyte Interphase

Conversion reaction systems such as transition metal oxides, sulfides, nitrides and phosphides have all been considered for negative electrodes in the lithium ion cell. For positive electrodes a similar process to the negative electrode occurs when forming an SEI layer. When the potential is below what is required for the electrolyte component to become thermodynamically unstable and there is a sufficient exchange current for electrochemical reduction, decomposition of the electrolyte occurs at the electrode/electrolyte interface to form an SEI layer. For the conversion systems the SEI evolution is dependant on the state of its lithiation [67, 89], whereas for carbonaceous materials and lithium-alloys the formed SEI changes as a function of potential and remained largely intact [90] and was less than what was required to maintain the electrochemical reduction of electrolyte species. The large voltage hysteresis of conversion materials and the redistribution of bonds during cycling resulted in an SEI that decomposed reversibly during the reconversion process [77, 91].

A decomposition layer on a metal oxide was discovered below 0.8V vs Lithium and was consistent with the electro-catalytic decomposition of electrolyte and led to an increased electrochemical capacity larger than the theoretical capacity [92, 77] in CuO cells. This decomposition layer was gel like at low potentials but upon charging above 2V vs lithium was no longer observed and improved the cycling as the electrode was charged to higher potentials. This gel like layer was shown to include lithium carbonate, lithium alkyl carbonate and polymeric species [93, 94, 95] near to the electrolyte, while lithium oxide and lithium carbonates were found near to the converted metal particles. The polymeric layer, unlike the lithium carbonate type phases that remained intact, was found to be driven electrochemically to dissociate through a dissolution process [96]. Both these layers were found to be reversibly formed and decomposed after the initial cycle whilst growing thick enough to allow the diffusion of lithium ions.

It has been shown in metal fluorides that a Li_2CO_3 induced formation from cyclic carbonates dominated the SEI found in converted BiF_3 nanocomposites (3LiF + Bi) at voltages near 2V vs Lithium. The presence of the nanometal was attributed to this induced Li_2CO_3 as it was also found on converted FeF_2 materials but not on nano-carbon or metal sulfide substrates, however using linear carbonates in the electrolyte did not show the induced formation. The SEI was shown to also decompose at 4.4V and that there was a relationship to the degree of SEI formed and the cycle life of the material [97] meaning the dynamic and constantly changing bonds of the metal fluoride conversion electrodes aggregate the interaction of cyclic carbonate electrolytes and the conversion material [98]. There was a marked improvement using acyclic carbonates and non-carbonate solvents such as nitriles, ethers and ionic liquids in the cycle life of this type of metal fluoride electrode.

3.4.1 Summary

It is clear that metal fluorides offer great advantages, despite their inefficiencies, over current intercalation compounds in the use of lithium batteries, and is an area where more research can be focused towards. This being the case this thesis is investigating a non-transition metal fluoride as a cathode material, to see if there are any advantages or disadvantages over the transition metal fluorides currently researched.

Aluminium fluoride is a material that is not on the list of tried cathode materials. It has been used to coat certain materials to improve their cyclability and act as an interfacial stabiliser, as it is proposed to prevent cathode/electrolyte interfacial degradation by the decomposition of the electrolyte at high potentials and stops acidic species from the electrolyte attacking the electrode material [99, 100, 101, 102].

It may not have been tried as a cathode material due to it being highly insulating, however by reducing the particle size may improve conductivity. This next section explores the possibility of using this material as a cathode material.

3.5 Aluminium Fluoride Theory

Aluminium fluoride upon reaction with lithium ions follows proposed equation 3.2.

$$3Li^+ + 3e^- + AlF_3 \longleftrightarrow 3LiF + Al \tag{3.2}$$

As aluminium is reduced from Al^{3+} to Al^0 the fluoride bonds are broken and reacts with lithium to form LiF. The reaction is similar to the well documented FeF_3 reaction with lithium. However as there is no recorded $Al^{2+}F_2$ phase of aluminium fluoride there should theoretically be a one voltage plateau as Al^{3+} is being reduced

to Al^0, unlike the FeF_3 reaction which has two voltage plateaus. One for the first reaction of $Fe^{3+}F_3$ to $LiFe^{2+}F_3$ and then $Fe^{2+}F_3$ to Fe^0, as shown in equations 3.3 and 3.4 [82, 26].

$$Fe^{3+}F_3 + Li^+ + e^{-1} \longrightarrow Li^+Fe^{2+}F_3 \tag{3.3}$$

$$Li^+Fe^{2+}F_3 + 2Li^+ + 2e^{-1} \longrightarrow Fe^0 + 3LiF \tag{3.4}$$

The mechanism for reversibility is based on the assumption that aluminium fluoride is similar in structure to iron fluoride so the mechanism for charge and discharge is the same. Upon reacting with lithium, iron fluoride is converted to metallic iron and lithium fluoride [82]. It is suggested that as metal fluoride compounds are highly ionic the transition between phases behaves so that the redox potentials approach those of free ions in a solution. The conversion reaction results in small lithium fluoride and iron products on the scale of 2-5nm [15]. Due to the thermodynamically stable iron and lithium fluoride reversibility and reformation of the metal fluoride structure can occur on the following charge [28].

Aluminium fluoride is a non conductive solid due to its ionic bonding. However, if the compound is molten or dissolved in a solvent it can become conductive due to the ions availability to move freely.

3.5.1 Structure and Stability

Aluminium fluoride has the same structure as Iron fluoride, rhombohedral with an R-3c space group one. The Aluminium fluoride structure adopts the rhenium trioxide motif, featuring distorted AlF_6 octahedra. Each fluoride is connected to two Al

centers as can be seen in figure 3.2, the aluminium is the octahedrons connected to one another by fluoride.

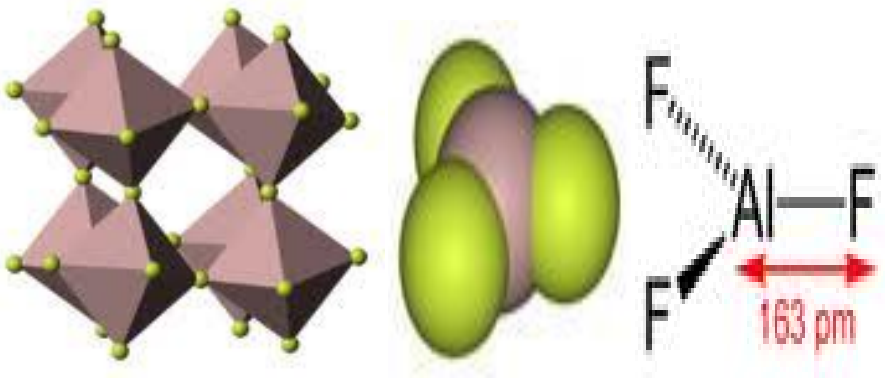

Figure 3.2: The aluminium fluoride structure. [103].

Upon reaction with lithium the aluminium is reduced to form metallic aluminium which has a face centered cubic structure, unlike iron which has a body centered cubic structure at the same temperature. Lithium fluoride forms a cubic structure. Both of these forms are highly stable and it is this stability which has hindered the development of the materials for rechargeable batteries.[104] reports that LiF is electrochemically active in the form of metal lithium fluoride composites, where the LiF and metal are dispersed on a nanometer scale.

Aluminium is usually used as the current collector in cathodes due to it being highly resistant to corrosion in $LiPF_6$ battery electrolytes [105] where it is being covered by the cathode material. However, due to porous electrodes there have been signs of low level localised corrosion due to underdeposit corrosion, the aluminium locally corrodes underneath the cathode where electrolyte is trapped [106]. At low potentials the aluminium is protected by an air-formed oxide layer [107] and at high potentials above 4V the aluminium is oxidised to form a nanometer thick layer of AlF_3 above the air-formed oxide layer, to protect against further corrosion [105].

With the conversion reaction forming aluminium nanoparticles there may be an issue with aluminium corrosion, however upon oxidation the aluminium should reform to AlF_3 which is known to protect against corrosion.

It is well known that the chemical compound aluminium fluoride and its products when reacted with lithium are stable at room temperature in an aqueous free environment. Aluminium fluoride can react with water to produce hydrogen fluoride and can also produce hydrogen fluoride if decomposed above 600°C. Most lithium batteries use a non aqueous electrolyte so the formation of HF is unlikely, however it is unknown if any side reactions will occur experimentally with a lithium based electrolyte, however as the aluminium fluoride is reacting with the lithium metal ions there should not be any side reactions.

3.5.2 Operating Voltage

Many trifluorides have been reported to have a useable operating voltage due to the highly ionic metal-ligand bonds [59]. The redox potential of aluminium fluoride can be estimated by ignoring the contribution from the ligand to the metal electronic state and using the standard electrode potentials. The potential data is known for the aluminium ion in strong acidic media and can be taken to be completely ionic in equation 3.7.

$$Al^{3+} + 3e^- = Al^0 \ -1.66 \text{ V versus NHE} \tag{3.5}$$

For the lithium redox potential the data is:

$$Li^+ + e^- = Li \ -3.05 \text{ V versus NHE} \tag{3.6}$$

We can now estimate the cell voltage with an ionic aluminium (III) cathode as:

$$Al^{3+} + 3Li = Al^{0} + 3Li^{+}\ 1.39\ \text{V} \tag{3.7}$$

However by calculating the Gibbs free energy change of $AlF_3 \longrightarrow LiF$ and using Equation 2.1 gives a cell potential of 2.89V, (ΔG for AlF_3 and LiF is -1430.928 and -588.688 kJ/mol respectively. Due to the standard electrode potential data not taking into consideration the fluoride component this could be a reason for the large difference in values.

3.5.3 Capacity

Aluminium fluoride has a molecular mass of 83.98 g/mol and has three valent states of aluminium. This allows 3 moles of material to take place in the electrochemical reaction and using equation 2.2 gives a theoretical specific capacity of 957 mAh/g. Comparing it to other metal fluoride materials in Table 2.2 it can be seen to have a comparable capacity to the higher capacity materials, such as Cr_2O_3, but with a slightly higher theoretical voltage. The theoretical energy density can also be calculated from the capacity and theoretical voltage and is around 1330 Wh/kg to 2766 Wh/kg which is one of the higher values in the trivalent fluorides.

3.5.4 Material Characteristics

The advantage of this material is that it has a high theoretical capacity of 957mAh/g and has a discharge reaction voltage between 1.39V and 2.89V which gives an energy density of between 1340Wh/kg and 2766Wh/kg which is higher than any other commercialised positive electrode material. It has the same structure as iron fluoride and can be compared to it during its redox reactions. The redox potential is

somewhat low which is why aluminium is used as a current collector as it is stable in non-aqueous solutions at high potentials. This is because the aluminium becomes passivated by species found when the aluminium reacts with the electrolyte. Theses species precipitate on its surface and prevent aluminium dissolution and still allow electrical contact with the cathodes active mass [55]. The high redox potential of fluorine makes up for this when formed with aluminium to give aluminium fluoride and a theoretical cell voltage of between 1.39V - 2.89V, which is acceptable due to its low atomic weight.

In addition to superior energy density and specific energy, AlF_3 has the potential to be significantly more affordable than existing LIB cathode materials. Recent prices for existing cathode raw materials are as follows: lithium cobalt oxide at US$88,490 per ton, lithium iron phosphate at US$24,000 per ton, and lithium manganate at US$7,375 per ton. While the price of aluminium fluoride has risen recently, it is currently around $1,440 per ton. This project therefore aligns with the scope by developing an affordable, effective and efficient electrical energy storage material.

3.6 Proposed Approach

This thesis will look at using aluminium fluoride as a cathode material for lithium batteries. As no investigation has been made on the use of AlF_3 as a cathode material this thesis will start from experimenting with the pristine material and then reduce the particle size. Initial tests will be carried out using common lithium electrolytes and cell preparation methods which will show initial material viability as a cathode material for rechargeable batteries. This should provide information about the mechanisms involved and how they can be improved.

Chapter 4

Experimental Methods

This chapter describes the characterisation techniques used in the analysis of aluminium fluroide powder and when fabricated into an electrochemical cell. It will first describe the synthesis method of producing aluminum fluroide nanorods and then will describe the characterisation techniques.

4.1 Synthesis Method

Aluminium fluoride nanorods were synthesised by a precipitation method and followed the following procedure.

Aluminium flouride nanoparticles were precipitated from a solution reaction of, aluminium nitrate ($Al(NO_3)_3$), ethanol solution (0.25mol/L) and Ammonium bifluoride (NH_4HF_2), by thoroughly stirring using polyethylene glycol (PEG) as a surfactant (0.005mol/L). The solution was centrifuged at 5000rpm for 15 mins and then washed in ethanol to remove residual HF. The resulting precipitate was dried at 70°C under vacuum for 2 hrs and the resulting powder was calcined under argon at a desired temperature for 2 hrs.

4.2 Material Characterisation

A number of techniques were used to characterise the structure, size and the surface morphology of the bought and synthesised particles.

4.2.1 Structure Characterisation

X-ray Diffraction

X-ray powder diffraction measurements were performed on a Siemens D5005 and the spectra was taken in the 2θ range of 5-90°. Ex-situ XRD measurements were recorded by dissembling a fabricated cell and washing the working electrode in dimethyl carbonate and drying under argon. The electrode was then placed on a glass slide and covered with Kapton film using a seal layer of vacuum grease.

In order to determine the crystalline phase, orientation of materials, lattice parameters and approximation of crystallite size the particles underwent X-ray diffraction. The wavelengths of the X-rays are comparable in size to the interplanar spacing so disperse the X-rays and produce a diffraction pattern. The spectrums generated by X-ray diffraction follow Bragg's Law:

$$2dsin\theta = n\lambda \tag{4.1}$$

where d is the interplanar spacing, θ is the angle of incidence with respect to the normal, n is usually one but represents an integer defining the order of diffraction and λ is the wavelength of the X-ray. When λ is fixed and the angle of incidence is varied the interplanar spacing can be found, thus allowing the identitiy of the structure and composition to be determined by inspecting the resulting diffraction pattern. The unit cell of a crystalline powder is distinguished by the structure factor,

which is the sum of all the atoms in the unit cell and is defined by [108]:

$$F_{hkl} = \sum_j f_j e^{i\theta_{hkl}(j)} \quad \text{where} \quad \theta_{hkl}(j) = 2\pi(hx_j + ky_j + lz_j) \tag{4.2}$$

The quantity F_{hkl} is called the structure factor, h, k, and l are the Miller indicies for the reflection, f is the atomic scattering factor, the ratio of the amplitude scattered by an atom at rest to the amplitude of a single electron. j is a counter for x, y and z which are the coordinates of the atom in the unit cell. The peak intensity is proportional to the modulus of the structure factor squared.

The crystallite size of the sample can also be determined from a XRD pattern and is calculated from the Scherrer formula:

$$L = \frac{K\lambda}{Bcos\theta} \tag{4.3}$$

The calculated crystallite size is L, B is the peak width, K is the shape factor, assumed to be 1 and λ is the x-ray wavelength.

Fourier Transform Infrared Spectroscopy

IR spectra were recorded on an Avatar 370 FT-IR spectrometer (Thermo-Nicolet), using the potassium bromide (KBr) pellet technique (loading 0.3 wt%) in the range of 4000-400 cm^{-1}. Fourier transform infrared spectroscopy is used to determine IR-active molecules of a sample in either a liquid, gas or solid sample. Figure 4.1 shows the workings of a Michelson interferometer used in FTIR. A beam splitter splits a collimated beams wavefront onto a fixed mirror and a moveable mirror. The beams then proceed to the sample area and dector after they are reflected and transmitted once and recombined at the beam splitter. The detected intensity as a function of moving mirror position, $I(x)$, is then transformed via a fourier transform into the

intensity spectrum as a function of frequency, Gk.

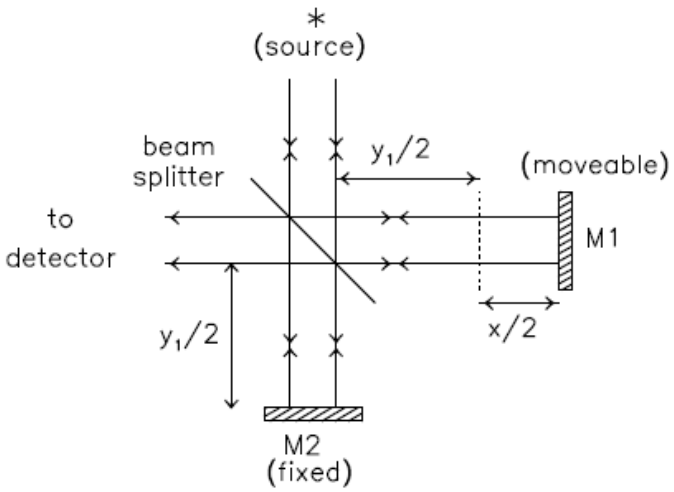

Figure 4.1: Schematic view of Michelson interferometer showing the collimated beam from source being split and recombined after being reflected and transmitted by two mirrors, one fixed and one moveable [109].

4.2.2 Morphology and Size Characterisation

The morphology and the size of the particles used in the study were characterised by scanning electron microscopy (SEM), transmisson electron microscopy (TEM) and nanoparticle tracking analysis.

SEM and EDX

SEM images were taken on a FEI XL30 SFEG analytical SEM (FEI), with a beam voltage of 15KeV.

The scanning electron microscope uses accelerated electrons carrying a large amount of kinetic energy to interact with a sample. When the electrons interact with the sample the energy is dissipated as a variety of signals as the incident electrons are decelerated as they hit the sample. The signals are produced by, backscattered electrons, diffracted back scattered electrons, photons, visible light, heat and secondary

electrons. It is the secondary electrons which produce the SEM images as they can show the morphology and topography. Figure 4.2 shows a schematic view of the scanning electron microscope.

Energy dispersive X-ray spectroscopy (EDX) analysis was carried out using the same instrument as the SEM and TEM and is used for elemental analysis. The sample is bombarded with a beam of high energy charged particles excite electrons within the inner shell leaving an electron hole, which is filled by an electron from an outer shell. The difference in energy between the higher energy shell and lower energy shell is released in the form of an X-ray. The number and energy of the emitted X-rays are measured by an energy dispersive spectrometer allowing the elemental composition of the sample to be ascertained.

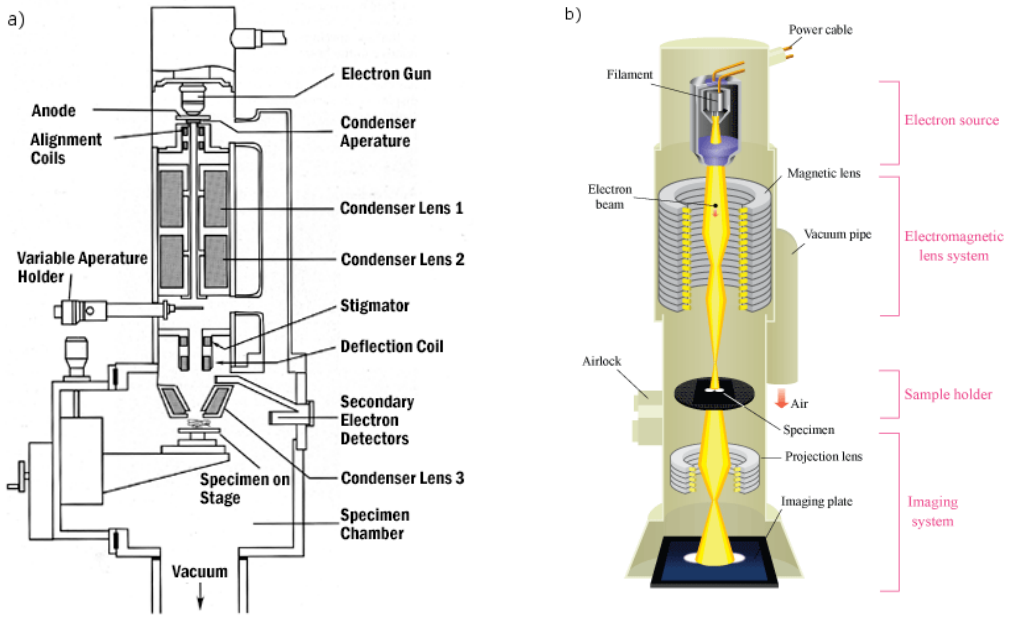

Figure 4.2: Scehmatic view of a scanning electron microscope [110] (a) and a transmission electron microscope (b) [111].

TEM

TEM images were taken on a CM20 Scanning TEM (Philips) with the sample being dispersed in a solution and then lifted onto a carbon coated copper grid for analysis. The transmission electron microscope is similar to the scanning electron microscope but has a greater magnification and is based on transmitted electrons instead of scattered electrons. The high energy electons are acclerated to nearly the speed of light and are directed into a thin-section of material where the electrons are scattered by the atomic planes (if crystalline) and then refocused to produce the required image [112]. Figure 4.2 shows the schematic representation of a transmission electron microscope.

Selected Area Electron Diffraction

During TEM analysis the samples are characterised by selected area electron diffraction. In this technique a beam of electrons are passed through the sample and due to their wavelike nature and the large differences between wavelengths of the electrons and atomic spacings within the sample, the atoms act as a diffraction grating to the electrons, diffracting them. This diffraction pattern is determined by the crystal structure of the sample and the selected area diffraction pattern is produced. By determining the diffraction ring spacing the lattice parameter and hence structure and sample can be determined. Figure 4.3 shows a typical selected area diffraction pattern.

The d-spacings in nm can be calculated from the SAED image by dividing the camera constant for a particular lens length by the measured radius.

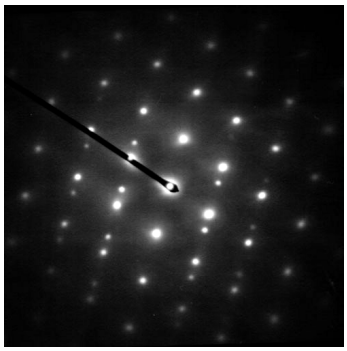

Figure 4.3: Selected area diffraction pattern of austenite in steel [113].

Nanoparticle Tracking Analysis

A Nanosight LM20 was used to help determine the particle size of the samples. The particles were prepared in isopropanol and placed in an ultrasonic bath for 30mins. The nanosight LM20 analyses a video recording of the motion of the particles in a viscous liquid under brownian motion to produce high-resolution particle size distributions. Figure 4.4 shows the basic principle of particle size analysis using nanoparticle tracking analysis.

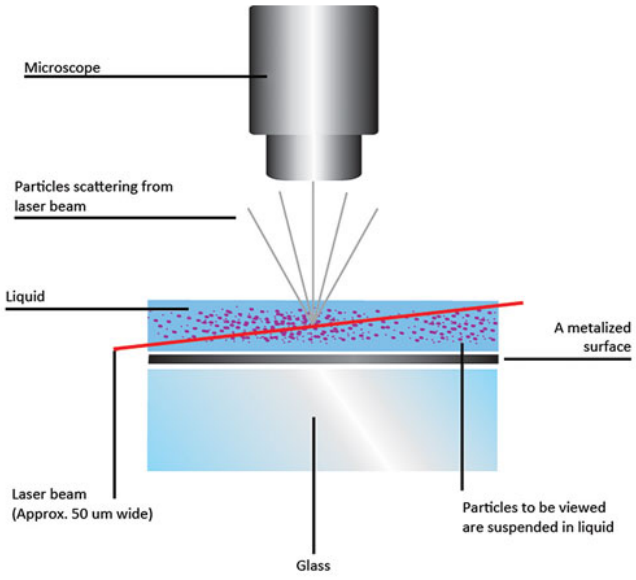

Figure 4.4: Schematic representation of the NTA [114].

Tap Density

The tap density was measured by placing around 1g of powder in a small glass vial and tapped on the lab bench 50 times by hand. The measured volume of the tapped powder and the mass was used to calculate the tap density [115]

4.2.3 Conductivity Measurements

The electrical conductivity of the samples were measured by applying a voltage through the sample and measuring the current.

The powdered samples were die pressed with a pressure of 1.5 tonnes/cm^2 and then coated with a Ag conductor paste on both sides to form blocking electrodes. A voltage is applied through the sample and the current is recorded. From equation 4.4 the resistivity can be determined and then using equation 4.5 the conductivity σ can be calculated.

$$\rho = \frac{VA}{It} \tag{4.4}$$

where ρ is the resistivity, V is the voltage applied, I is the current recorded, A is the area of the electrode and t is the thickness of the electrode.

$$\sigma = \frac{1}{\rho} \tag{4.5}$$

4.3 Cell Preparation

Each cell was prepared the same unless otherwise stated in the literature. This was to ensure that the results were due to the material itself and not the way the cell

was created. Each cell was constructed by mixing 50 wt% of active material with 20 wt% polyvinylidene fluoride as binder and 30 wt% Super P as a conductive additive. These were then homogenised in a solvent of n-methyl-pyrrolidine for 30 mins. This slurry was tape cast using a doctor blade onto a stainless steel current collector and dried at 120° C to remove the solvent. The electrode was then dried overnight under vacuum in order to remove any trace water. After drying the electrode was transferred into an argon filled glove box where a two electrode, CR2032 coin cell, was fabricated with a Lithium anode. A stainless steel electrode was used as to rule out an contributing capacity from an aluminium current collector and Lithium alloying when charging. The amount of active material in the electrodes varied between 5-10mg. The electrolyte used was 1M $LiPF_6$ in ethylene carbonate:dimethyl carbonate (EC:DMC).

For the cyclic voltammetry tests a three electrode swagelok cell was fabricated with lithium acting as the counter and reference electrode.

4.4 Cell Characterisation

In order to test the electrochemical performance of the samples the cell was characterised by galvanostatic cycling, galvanostatic intermittent titration, cyclic voltammetry and impedance testing. The tests were either carried out on a Verstat 4 potentiostat or a MTI 8 channel battery tester.

4.4.1 Galvanostatic Cycling

Galvanostatic cycling is a method where a current is applied across an electrochemical cell. The voltage of the cell as the current is applied can then be recorded as is the time. The recorded voltage is a result of the concentration of the redox species at

the electrodes. When a current is applied the redox reaction occurs at the electrode so that the current can be maintained and the concentration of the oxidised product is decreased. There is now a concentration gradient between the electrode surface and the bulk solution and molecules of the oxidant diffuse down to the electrode surface. The potential depends on the Nernst equation:

$$E = E^{0'} + \frac{0.059}{n} \log \frac{C_O^s}{C_R^s} \tag{4.6}$$

where C_O^s and C_R^s are the surface concentrations of the oxidant and the reductant respectively. As the concentrations vary with time the potential varies with time which is shown in the charge/discharge curves, with the time function replaced by specific capacity. Once there is no more oxidant at the electrode surface the current can no longer be maintained by the electron transfer reaction so the potential drops. If a potential window has not been set another analyte could produce a second electron transfer reaction or the electrolyte could undergo reduction. The time required for the concentration of the oxidant to reach zero is dependant on the applied current as is defined by the Sand equation:

$$it^{\frac{1}{2}} = \frac{nFAC\pi^{\frac{1}{2}}D^{\frac{1}{2}}}{2} \tag{4.7}$$

where C is the bulk concentration of the active material, D is the diffusion coefficient, A is the electrode surface area and the other variables are as described as before.

The specific capacity was determined by charge discharge cycles using galvanostatic cycling. The discharge rate current is calculated at the specific capacity of the electrode active material in the number of hours required to discharge. For a C rate of 0.1C (where the material wants to be discharged in ten hours) an electrode with a mass of 6mg of active material would require a discharge current of 0.57mA to

be fully discharged in ten hours, corresponding to a specific capacity of 957mAh/g. The discharge current D_c can be calculated from equation 4.8:

$$D_c = \frac{T_c A_m}{D_t} \tag{4.8}$$

where T_c is the theoretical specific capacity, A_m is the mass of active material and discharge time D_t you want full theoretical capacity to be realised in. The charge current was calculated in the same way as the discharge current. For tests where the C rate is not explicitly stated the charge rate can be taken to be 0.01C and the discharge rate 0.05C.

4.4.2 Cyclic Voltammetry

Cyclic voltammetry involves applying a variable voltage between two values, at a particular scan rate and recording the current. The voltage scans from the low potentials to the higher potentials and back again. As the voltage is swept the surface equilibrium at the electrode changes and the current flows. The higher the voltage the more reactant is being reacted with and so the current increases until a peak occurs when the diffusion layer has grown sufficiently above the electrode so that the movement of the reactant to the electrode is not sufficient to satisfy the Nersnt equation and the current drops. As the voltage moves back to the lower vertex the current now flows due to the solution species back onto the electrode and current should show a peak the same way as it did as the voltage was scanned to the first vertex. The diffusion coefficient of the Li ion in the electrode can be calculated from the Randles-Sevcik equation, by the relationship between the peak current and the square root of the scan rate:

$$\frac{I_p}{m} = 0.4463F\left(\frac{F}{RT}\right)^{\frac{1}{2}} C_{Li}V^{\frac{1}{2}}AD^{\frac{1}{2}} \tag{4.9}$$

where i_p is the peak current, m is the mass of the electrode, F is the Faraday constant, C_{Li} is the concentration of Li ion in the cathode, V is the scan rate, D is the diffusion constant and A is the contact area between electrode and electrolyte.

The cyclic voltammetry tests were recorded from a potential range of 1 - 4.5V at a scan rate of 0.1mV/s.

4.4.3 Galvanostatic Intermittant Titration

The galvanostatic intermittent titration technique was developed to determine the diffusion coefficients of Li-ions in electrode active materials. It is considered to be a more reliable method to determine the D_{Li} for compounds with varying composition than the galvanostatic cycling technique. It uses the same principles but a smaller current is applied for a set period. The cell is then relaxed for a length of time and its open circuit voltage is recorded. This continues until the cell is discharged. The results can then be used to plot a columetric titration curve of open circuit potential against state of charge or number of lithium ions inserted into cathode material.

4.4.4 Electrochemical Impedance Spectroscopy

Electrochemical impedance spectroscopy (EIS) represents a powerful method for investigation of electrical properties of materials and interfaces of conducting electrodes. EIS studies the system response to the application of a periodic small amplitude ac signal. As stated earlier before a current flowing at an electrified interface due to an electrochemical reaction, always contains nonfaradaic components, no matter how well the measurement is made. Figure 4.5 decipits an electron transfer-

ring across an electrified interface and the faradaic and nonfaradiac components are a result of the charge transfer.

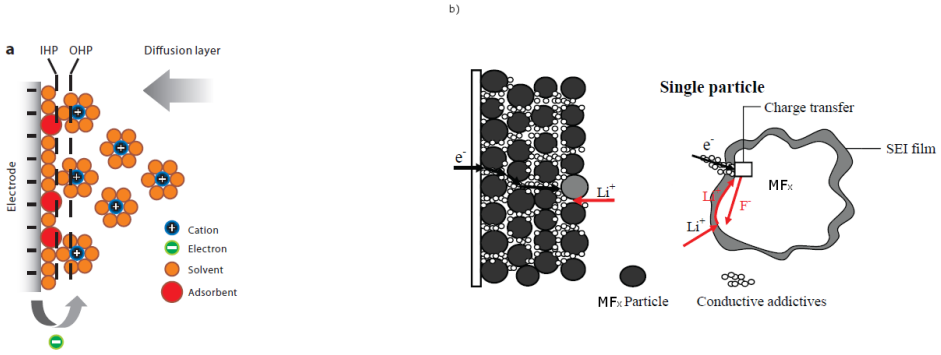

Figure 4.5: Negative electrode with an electrified interface where IHP is the inner Helmholtz plane and OHP is the outer helmholtz plane. [116]. (a) Model representing the conversion mechanism of lithium and a metal fluoride [117].

Figure 4.5 shows the model for lithium-ion insertion and de-insertion into a metal fluoride and is the basis for the Randles equivalent circuit model.

As the electron overcomes the polarisation resistance (charge transfer resistance) R_{ct} and the electrolyte resistance R_Ω (further denoted R_s) the faradaic component arises. The constant phase element C_d is responsible for the nonfaradiac current. The Warburg impedance W is a result of the mass transport of the reactants and products when the charge transfer takes place at the interface, which can be seen as a peak in a CV curve [116]. This information is usually represented in an electrical equivalent circuit (EEC) analog shown if figure 4.6. The EEC is used as a model to describe the electrochemical reaction that takes place at the electrode/electrolyte interface.

Using figure 4.6 and equations 4.10 the values of the charge transfer resistance, electrolyte resistance and Warburg impedance can be found and calculated from:

$$|W| = \sqrt{2}\frac{\sigma}{\omega^{\frac{1}{2}}} \tag{4.10}$$

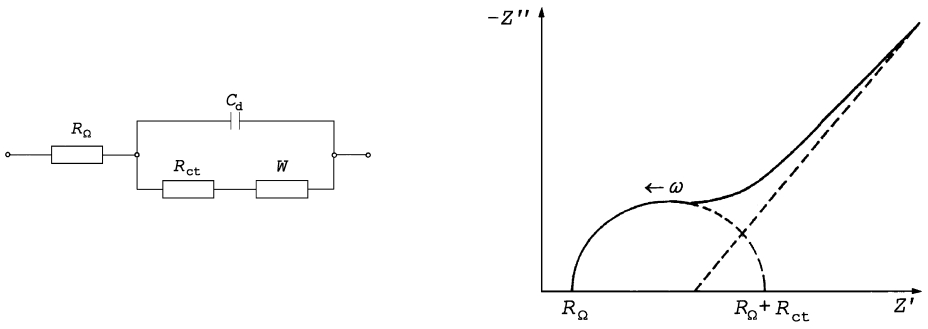

Figure 4.6: The scheme of Randles equivalent circuit (a) where the high frequency region correlates to the semi circle and the low frequency region a sloping line. The resistance between electrolyte and electrode R_Ω corresponds to the intercept at the Re (Z) in the high frequency region. The radius of the semicircle in the medium frequency region indicates the charge transfer resistance and the inclined line in the low frequency region corresponds to the Warburg impedance W which is related to the Li-ion diffusion (b).

where σ is the warburg coefficient and is equal to:

$$\sigma = \frac{|ImZ''|}{\omega^{\frac{1}{2}}} \tag{4.11}$$

From these values the diffusion of the Li-ion can be determined from:

$$D_{Li} = \frac{1}{2}\left[\left(\frac{V_m}{SFA}\right)\left(\frac{\delta E}{\delta x}\right)\right]^2 \tag{4.12}$$

Where V_m is molar volume, S is surface area of cathode, A is the warburg coefficient and $\frac{\delta E}{\delta x}$ is the slope of the coulometric titration curve.

Chapter 5

Aluminium Fluoride as a Novel High Capacity Cathode Material

This chapter describes the results of using aluminium fluoride as a cathode material in lithium batteries. It will first give a brief introduction to why it may be useful and needed, explain the brief experimental procedure and then discuss the presented results.

5.1 Introduction

As explained in the literature in the previous chapter current batteries energy densities fall short of energy goals in a lot of applications. Although it is not just how much energy can be stored in the electrodes that contribute to this failing it is the most crucial. The fundamental problem in attaining the highest specific capacity in an electrode is the utilisation of all the possible oxidation states of the compound in a redox cycle, this can be done using metal fluorides. As aluminium fluoride is cheaper than many current battery materials and may follow the same theory as iron fluoride due to structural similarities, it could be interesting material for use

as a cathode. This chapter will report the findings of using a number of aluminium fluoride samples as the cathode material against a lithium anode.

5.2 Experimental

Four types of AlF_3 powders were tested. The first was a commercially bought powder (from sigma-aldrich, further denoted CP), the second was the commercially bought powder ball milled (BM) and the third was the commercial powder ball milled and coated with a thin carbon coating (further denoted BMC) and the fourth was a carbon aluminium fluoride nanocomposite (NC).

The ball milled samples were prepared by mixing with isopropanol and ceramic mixing balls. The suspension was placed into a desktop ball mill and run for 240 hours. The suspension was dried to leave the ball milled AlF_3. The ball milled powder was then mixed with polyvinylidene fluoride (PVDF) (2wt%) and IPA for 2 hours. The suspension was then dried and the powder was calcined under argon for 2 hours at 600°C to leave a thin layer of carbon coating the AlF_3 powder. The nanocomposite samples were prepared by high energy milling $R\bar{3}C$ AlF_3 (Sigma Aldrich) with Super P in a weight % ratio of 85:15 respectively. The powders were placed within a hardened steel milling cell with hardened steel media in a SPEX 8000 high energy ball mill and milled for one hour. All the processes were completed within an inert atmosphere. All the powders were then prepared into either two electrode CR2032 coin cells or a three electrode swagelok cell for electrochemical testing.

PVDF was used as the carbon precursor for coating as it was used in the coating of CF_x to improve conductivity [118]. There are a number of other coatings that could be used which could be investigated in a future study to test for improvements.

5.3 Results and Discussion

5.3.1 Structural Characterisation

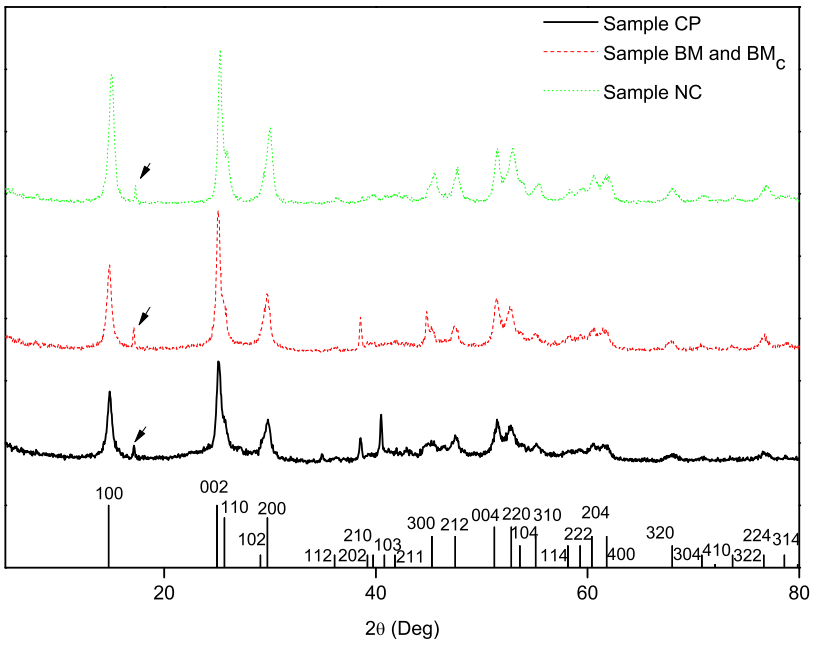

Figure 5.1: The XRD pattern of the commercial, ball milled and nanocomposite samples. The ball milled sample is carbon coated and taken from the same batch as sample BM. The diffraction peaks are indexed against the JCPDS no. 43-0435.

XRD patterns of the commercially bought, ball milled and nanocomposite powders are shown in Figure 5.1. It shows that both samples are the correct phase with a hexagonal lattice system and space group P63/mmc. The diffraction peaks of the samples are indexed based on JCPDS no. 43-0435 ($\beta - AlF_3$). However, there is a peak present in all the samples which is not indexed on the JCPDS reference indicated with the small arrow. Initially it was thought that the AlF_3 samples were reacting to air or moisture but could not be identified as such. The peak was not able to be identified and may have been an issue with the hardware rather than the sample.

The size distribution of the commercial powder and the ball milled powder can be

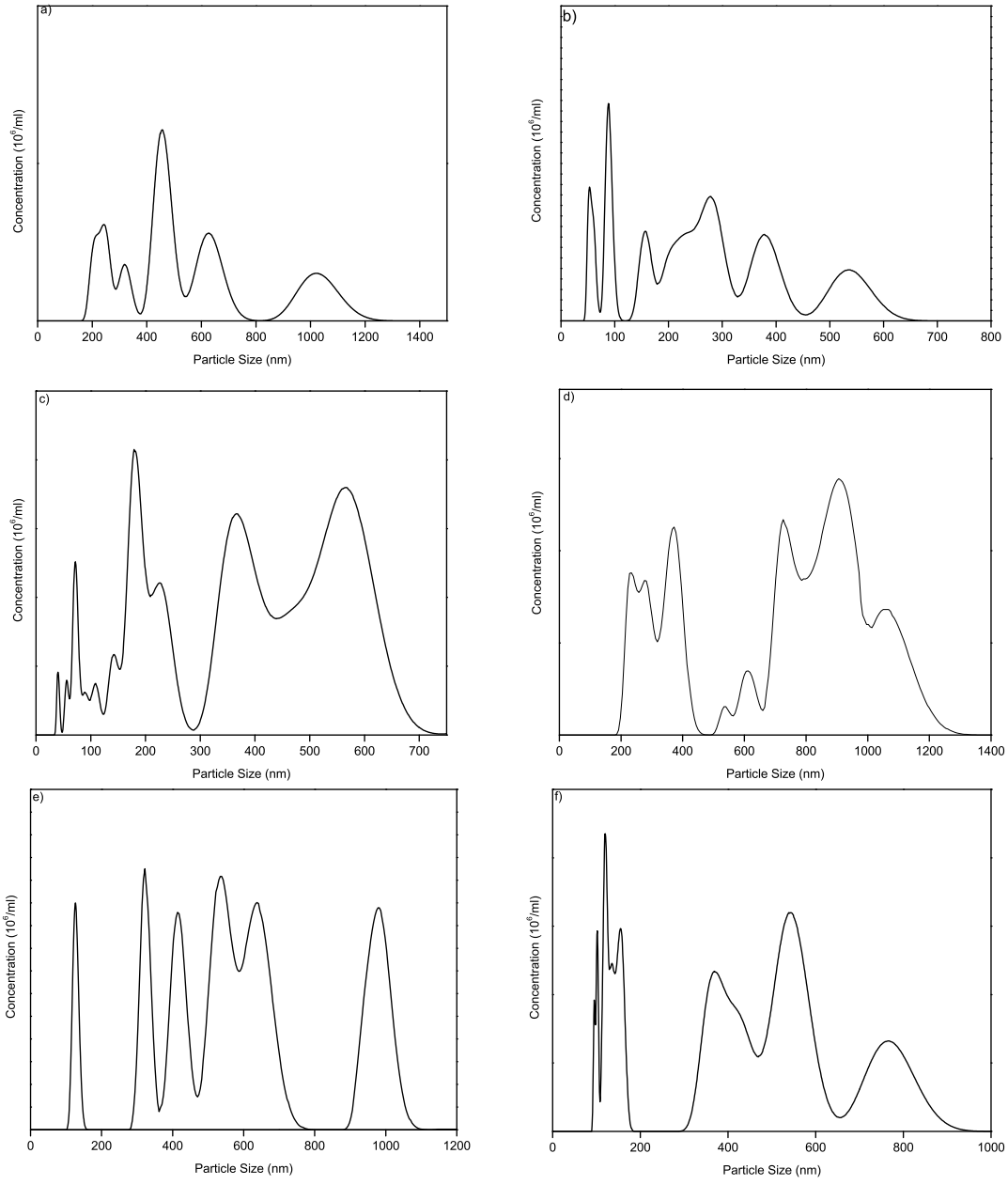

Figure 5.2: The average size distribution of samples CP (a), BM (b) and NC (c) taken over three different samples. Images (d), (e) and (f) show the average size distribution of samples ball milled for one day, two days and five days respectively.

seen in Figure 5.2. It can be seen that prior to ball milling the average particle size, over three different samples range from 200nm to over 1000nm. The highest concentration of particles is around 500nm in size. After ball milling and being coated the average particle size reduces and is in the range of 50nm 600nm, with the highest concentration being around 100nm. Images (d) (24 hours), (e) (48 hours) and (f) (120 hours) show the particle size distribution of four samples ball milled at different lengths of time. It can be seen that as the ball milling time is increased the mean particle size is reduced and it is the smallest particle size sample that was used in the electrode tests. The sample size did not reduce any further with milling over 240 hours. For sample NC it can be seen that there is a much larger range of particle sizes than in the BM sample, and they are smaller particles. The small size can be attributed to the high energy ball mill which can produce smaller particles than the normal ball mill method. The larger range can be attributed to the formed nanocomposite that is also formed. The carbon contribution would increase the overall size of the particles, depending on how big the nanocomposite agglomeration is. This is confirmed in the SEM images of the samples shown in Figure 5.3.

The BM sample can be assumed to be the same size as the BMC sample, as the carbon coating in Figure 5.3 shows the thickness does not add any further size to the diameter of the particle. The carbon coating of BMC can be seen as a thin layer surrounding the main particle shown in the TEM image.

5.3.2 Electrochemical Characterisation

All the electrochemical tests were carried out at room temperature and in the voltage range of 1V - 4.5V. As carbon has no contribution to the specific capacity in this voltage range [119] all the observed capacity can be attributed to the electroactive material AlF_3. Figure 5.4 shows the initial discharge capacities for sample CP at the three tested current rates, 0.01C, 0.05C and 0.1C and samples BM, BM_c and

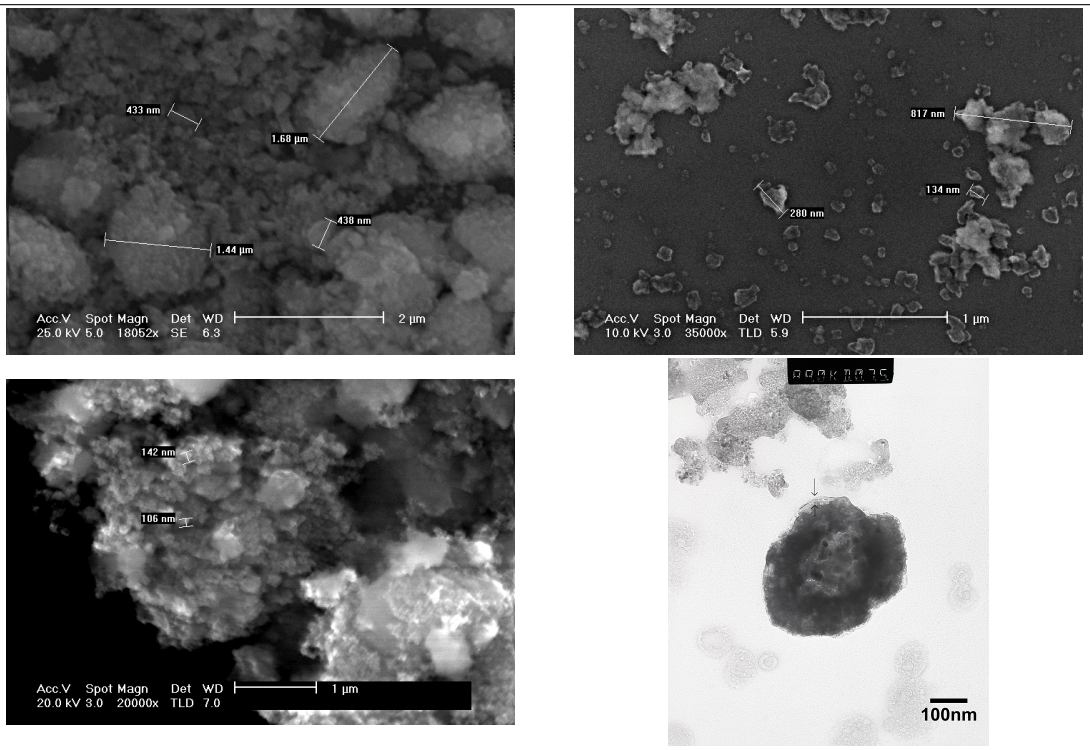

Figure 5.3: SEM images of samples CP (a), BM (b) and NC (c). TEM image of the carbon coating on sample BMC indicated by the arrows.

NC at their specific discharge rates.

At the slowest discharge rate it can be seen that the initial discharge capacity is over 100mAh/g with an average single stage voltage of around 1.6V. It starts around 2V and slowly declines until it reaches the lower limit of 1V. The specific energy density of this material is around 200 Wh/kg at a discharge rate of 100 hours. As the discharge rate is increased it can be seen that the single stage voltage profile drops and so does the capacity to around 30mAh/g at a rate of 0.1C. By changing the sample to either BM, BM_c or NC the initial discharge rate could be increased. It was found that the capacity increased dramatically compared to sample CP. For sample BM the capacities are 957, 486 and 125 mAh/g for discharge rates 0.1C, 0.125C and 0.17C respectively. For sample BM_c they are 957, 608, 263, and 43 mAh/g for discharge rates 0.1C, 0.125C, 0.17C and 0.25C respectively. This was increased even further by using sample NC with 0.1C, 0.125C, 0.17C, 0.25C and 0.33C discharge capacities being 957, 755, 472, 119 and 54 mAh/g respectively.

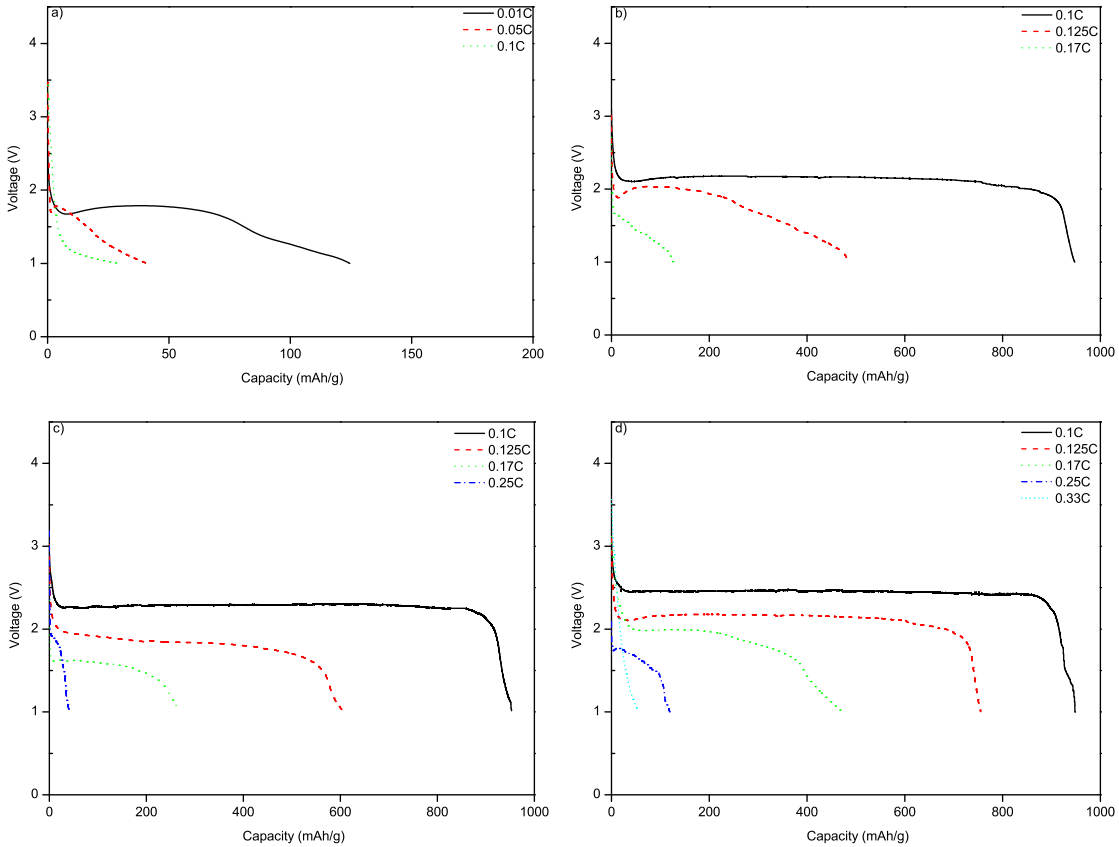

Figure 5.4: Discharge capacities of samples CP (a), BM (b), BM_c (c) and NC (d), at current densities specified in each image.

The poor first discharge capacity for sample CP can be attributed to the inferior conductivity compared with the other samples. As a current is passed through the material polarisation occurs and the resistance of the material increases. This polarisation is a contribution of activation and concentration due to the materials poor conductivity. As the ions pass through the electrolyte and reach the electrode / electrolyte phase boundary there could be the formation of a passivating SEI layer that makes the electrode become passive. Added to that the inherent poor conductivity of aluminium fluoride, even the low current density passing through the cell could be too fast for the material, a concentration gradient builds up at the electrolyte / electrode interface resulting in a quick drop in potential and reduced capacity as not all the active material has taken part in the reduction. It may be

possible to decrease the lower voltage limit to less than 1V but there may be a case of unwanted side reactions such as electrolyte decomposition which could attribute to an increase in capacity, and the working voltage would be too low for any real life applications. This loss in capacity could also be attributed to the average size and shape of the particle resulting in the large diffusion distances of the electrons and ions. Due to the poor conductivity of the large particle powder the electrons are reaching the electrode surface quicker than they are able to pass through the electrode, causing the electron concentration gradient. It is well known that nm sized particles give a higher capacity than micron sized particles [35, 38] due to an increase in electroactive surface area and smaller pathways for the electrons and ions to pass through hence increasing electron and ion conductivity, thus reducing concentration polarisation and increasing capacity. It can be seen from the first discharge results of sample BM in Figure 5.4 that this is the case. The decreased particle size has resulted in the theoretical capacity being achieved for the first discharge cycle at a rate of 0.1C which is a much higher current density than what sample CP was put under. However, further increasing the current density results in a rapid reduction of capacity again due to the inherent properties of the material. In order to try and determine whether the electrolyte being in contact with the bare aluminum fluoride has an effect on increasing activation polarisation sample BM was coated to make sample BM_c. These results also shown in Figure 5.4 show that the polarisation does decrease as higher specific capacities can be attained at higher rates. The initial discharge plateau of 0.1C is also shown to have a higher discharge voltage than of the BM sample of 2.3V rather than 2.15V. This initial drop from the open circuit voltage of around 3.1V shows a reduced ohmic polarisation due to improved kinetics by reduced particle size. By coating the sample as in BM_c and incorporating a nanocomposite the kinetics were improved even further and the ohmic drop contribution to polarisation was reduced significantly. This also confirms that the total resistance through the cell is decreased as the voltage plateau

is increased. This produces an energy density of 2201 Wh/kg for sample BM_c and 2297 Wh/kg for sample NC which is a lot larger than current commercial materials. Even sample BM has an energy density of 2058 Wh/kg which is still larger than many commercial secondary lithium cathode materials. However, theoretical calculations using Al^{3+} redox values put the discharge voltage at 1.39V against Li/Li^+ and using thermodynamics and the gibbs free energy the theoretical voltage is 2.89V, so it is interesting to find different initial voltages. This initial voltage plateau is also increased in sample NC with a value of 2.4V at a discharge rate of 0.1C. The first discharge can be attributed to a thermodynamically changing AlF_3 to LiF which would expect to be seen at around 2.89V, however, due to the polarisations in the cell this drops and the initial plateau is seen between 2V and 2.5V. Rather than the experimental voltage being the 1.39V expected of Al^{3+} reducing to Al^0; by taking into account the contribution of fluorine the experimental voltage is closer to the thermodynamically calculated value of 2.89V.

Table 5.1 shows the energy densities of the tested samples against their initial discharge rate. It shows that upon first discharge the specific energy densities of aluminium fluoride is much larger than two existing commercial technologies.

Table 5.2 shows the powder conductivities of the CP, BM, BM_c and NC samples and confirms that this increase in conductivity for the BM_c and NC samples improves the discharge rate capacities by reducing the polarisation of the cell as current is passed through.

The single stage discharge plateau recorded at different discharge rates demonstrates a single step electrochemical reduction process of a three electron reduction of AlF_3 to form Al and LiF. The discharge plateau of the CP sample has a sloping profile and indicates there is both a solid and liquid phase during discharge. For the other samples the capacity recorded at the 0.1C discharge rate indicates a single solid phase as the plateau is flat. Increasing the discharge rate results in a sloping voltage

Table 5.1: Energy densities of samples CP, BM, BM_c and NC at particular specified discharge rates.

Sample	Discharge Rate (C)	Discharge Capacity (mAh/g)	Discharge Voltage (V)	Specific Energy Density (Wh/Kg)
CP	0.01	125	1.6	200
	0.05	41	1.4	57
	0.1	29	1.2	35
BM	0.1	957	2.15	2058
	0.125	486	1.8	314
	0.17	125	1.25	90
BM_c	0.1	957	2.3	2201
	0.125	608	1.9	1155
	0.17	263	1.6	421
	0.25	43	1.4	60
NC	0.1	957	2.4	2297
	0.125	755	2.15	1623
	0.17	472	1.9	897
	0.25	119	1.5	179
	0.33	54	1.3	70
$LiFePO_4$ [120]	1	147	3.4	500
CF_x [121]	1	712	2.2	1566

profile indicating that the two phases are present.

It is clear that by reducing the particle size the polarisation through the material has been lowered at the specific discharge currents. By coating the material the polarisation reduces even further so that even higher capacities can be reached at the particular current densities. The low capacity of the CP sample could be attributed to the formation of an SEI layer on the surface of the electrode as it is reaching equilibrium and a steady open circuit voltage. This electrode surface could contain some electrolyte anions and cations and become passive again increasing the resistance once a current is passed through the cell. However, by adding a layer of carbon as in sample BM_c or forming a carbon nanocomposite this carbon layer prevents direct

Table 5.2: Conductivities of samples CP, BM, BM_c and NC.

Sample	Resistance (Ω)	Area (m^2)	Length (m)	Resistivity (Ω m)	Conductivity (S/m)
CP	6.45×10^{8}	1.13×10^{-4}	7.5×10^{-4}	9.72×10^{7}	1.03×10^{-8}
BM	8.76×10^{7}	1.13×10^{-4}	7.5×10^{-4}	1.32×10^{7}	7.57×10^{-8}
BM_c	1.60×10^{7}	1.13×10^{-4}	7.5×10^{-4}	2.41×10^{6}	4.15×10^{-7}
NC	6.93×10^{6}	1.13×10^{-4}	7.5×10^{-4}	1.04×10^{6}	9.58×10^{-7}

electrode / electrolyte contact and stops any initial adverse reactions.

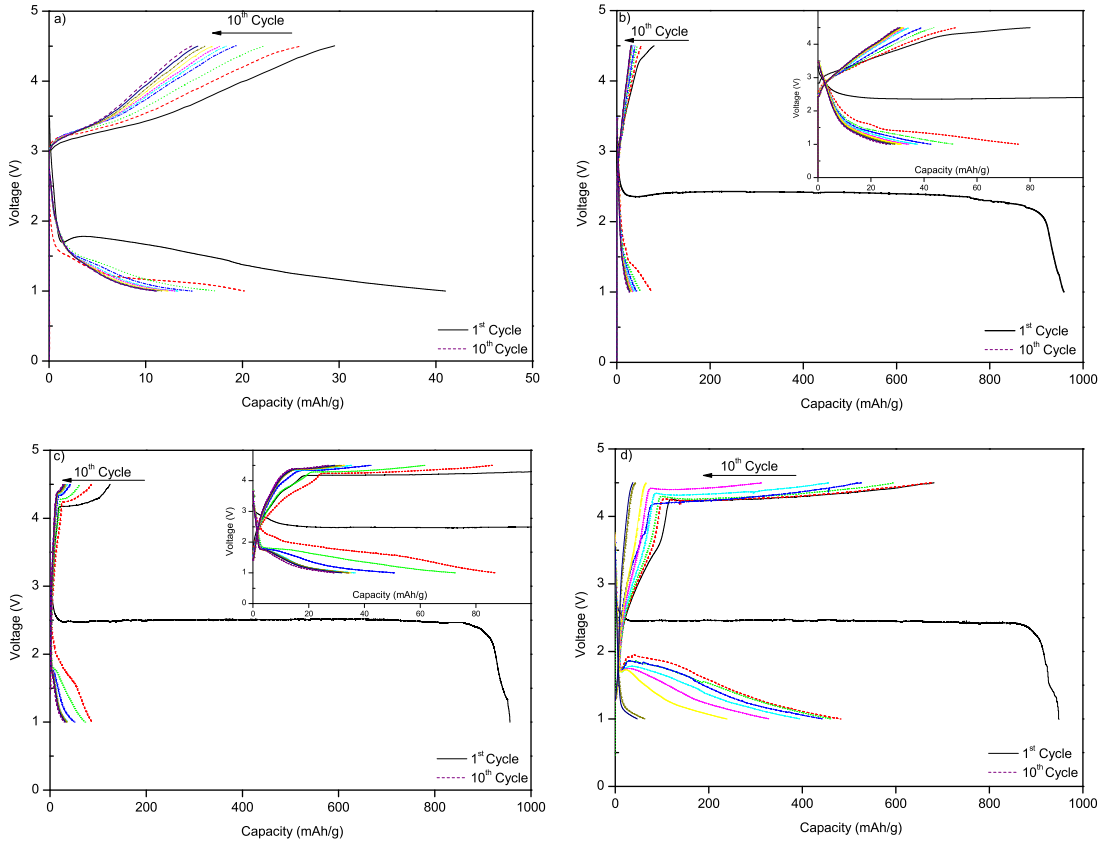

Figure 5.5: Cycling profile of samples CP (a), BM (b), BM_c (c) and NC (d) at a charge rate of C/100 and a discahrge rate of C/20. The insets of the graphs show are the smaller capacities enchanced.

Figure 5.5 shows the voltage profiles of the samples CP, BM, BM_c and NC for a discharge rate of C/20. It can be seen in the less conductive samples CP and BM that there is not much of a charging plateau indicating that polarisation is so large that Tafel behaviour is present and the electrode is irreversible with respect to a large percentage of theoretical capacity. The initial charge capacity is 80mAh/g resulting in a second discharge capacity of 76mAh/g which is less than 8% of the initial discharge capacity. The discharge capacity for cycle ten is 26mAh/g which is less than 3% of the initial capacity indicating rapid capacity fade during cycling. By increasing the conductivity of the powder and by introducing a layer between the

electrolyte and electrode material, by carbon coating, the initial charge capacity has increased to 125mAh/g, 13% of the initial discharge capacity and again undergoes rapid capacity fade to less than 3% of the initial capacity after ten cycles. Sample NC however, has a large initial charge of 682 mAh/g and a second discharge of 482 mAh/g, indicating a highly reversible process. This initial reversibility rapidly fades to less than 4% of initial discharge capacity after ten cycles though. The coating doesn't seem to have as much affect on the reversibility of the electrode as the nanocomposite. This indicates that there are processes that are involved with the conversion mechanism that reduce the efficiency of the carbon coating or nanocomposite from first discharge to last discharge.

It is also evident from Figure 5.5 that there is a huge inefficiency from the large difference in the discharge and charge potential profiles. This indicates that the reduction of AlF_3 has resulted in a LiF and Al composite that produces a large voltage hysteresis, which is evident in the charge discharge profiles. It can also be put down to the large surface area that is formed upon the reduction to LiF and Al. This large surface area of the reductants could react unfavourably with the electrolyte and cause new electrode / electrolyte surface interphases which require more energy to pass through, resulting in an increased charge potential. This inefficiency is slightly decreased with the improved conductivity and introduction of carbon, but due to the structural change that occurs during reduction this may not have an effect after the first discharge. In conversion reaction systems the voltage hysteresis has been linked to the finite kinetics which can be manipulated with particle engineering and a thermodynamic origin inherent to the starting material [122] and [123]. This can be seen here with the improved kinetics reducing this hysteresis but only until a point.

From the initial discharge the AlF_3 particles are thought to reduce to form LiF and Al. In [26] it is shown that when the particles are reduced to form LiF and

Fe they reduce in size to around 5nm. As AlF_3 has the same structure as FeF_3 it is fair to assume that the mechanism is similar and the LiF and Al particles that form are of similar size. These size particles could then react with the electrolyte and undergo further reduction reducing the amount of material that can be further charged. Upon recharging and removing the lithium ions AlF_3 reforms and due to some of the material having reacted with the electrolyte the capacity reduces. It has been shown that coating the electroactive material in a conductive substance the amount of dissolution in the electrolyte can be reduced. This is shown by the coated material having a higher capacity for more cycles. However, as this may be the case with intercalation compounds as there is no structural change the carbon coating remains intact. With metal fluorides there is a structural change and a reduction in particle size. With a material that is initially carbon coated, once it has been reduced and undergone structural change the carbon coating must either breakdown or encompass the material that has been broken down. If the coating breaks down, the electron and ionic pathways through the material may not be continuous and the internal kinetics of the material may be lower than that of when it was in its initial state which would affect the capacity upon recharge [51]. The surface of the active material that has not got a coating is then susceptible for dissolution in the electrolyte, reducing capacity. As well as the internal kinetics being reduced due to the electronic and ionic pathways not being continuous the removal of the carbon surface could encourage the LiF or Al to aggregate and decrease in surface area which would again reduce capacity upon recharge. When this coating breaks down there would be some surface of the resultant LiF and Al that is in contact with the electrolyte and could be susceptible to dissolution in the electrolyte which would reduce the amount of active material that could react with lithium ions upon recharging. However, it is unlikely that the aluminium reacts with the electrolyte in the particular voltage window used as it is currently used in lithium batteries as the current collector due to low anodic corrosion properties. If the carbon coating does

not breakdown and instead the AlF_3 is reduced inside the coating each particle that was coated would then involve many smaller particles that may not be connected efficiently and reduce the electron and ionic conductivity within the coated area as shown in Figure 5.6.

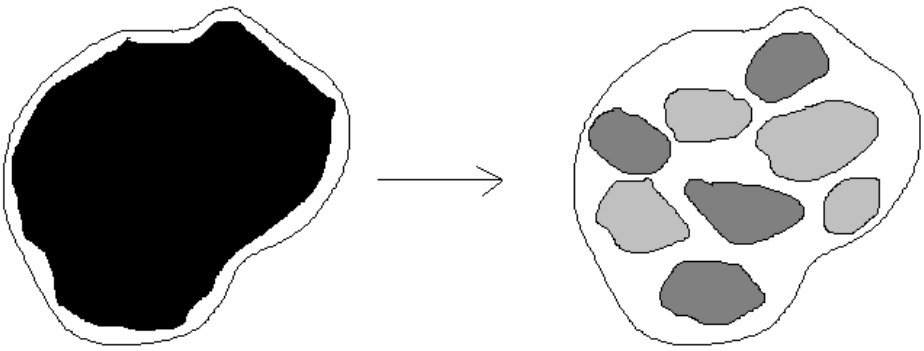

Figure 5.6: Simplified diagram of the conversion process with carbon coated material. The black filled material is the AlF_3 coated nanoparticle. The grey particles are the LiF and Al nanoparticles formed when AlF_3 is reduced, reducing the continuous electronic and ionic pathways, shown as the blank white area.

Figure 5.7 shows the capacity of the four samples after being cycled ten times at different discharge rates, the charge rate was kept constant at 0.01C. For all the samples it is clear that there is rapid capacity fade after a few cycles. The addition of carbon either as a coating or in a nanocomposite seems to improve the capacity retention but only for a few cycles. This shows that there is an increase in cell resistance as the cycle number increased indicating a reduced conductivity at either the bulk of the electrode, electrode surface or through the electrolyte. However, [102] states that aluminium fluoride has been used as a coating for other materials due to its stability and inertness in organic electrolytes. As the material is in the form of nanoparticles instead of a thin coating the material could be reactive in this morphology and cause a loss of electrode material resulting in a loss of capacity. This could explain why there is a larger cycle life with sample NC. The carbon nanocomposite stops the electrode material dissolving in the electrolyte.

It is also mentioned that conversion reactions undergo large structural changes [81]

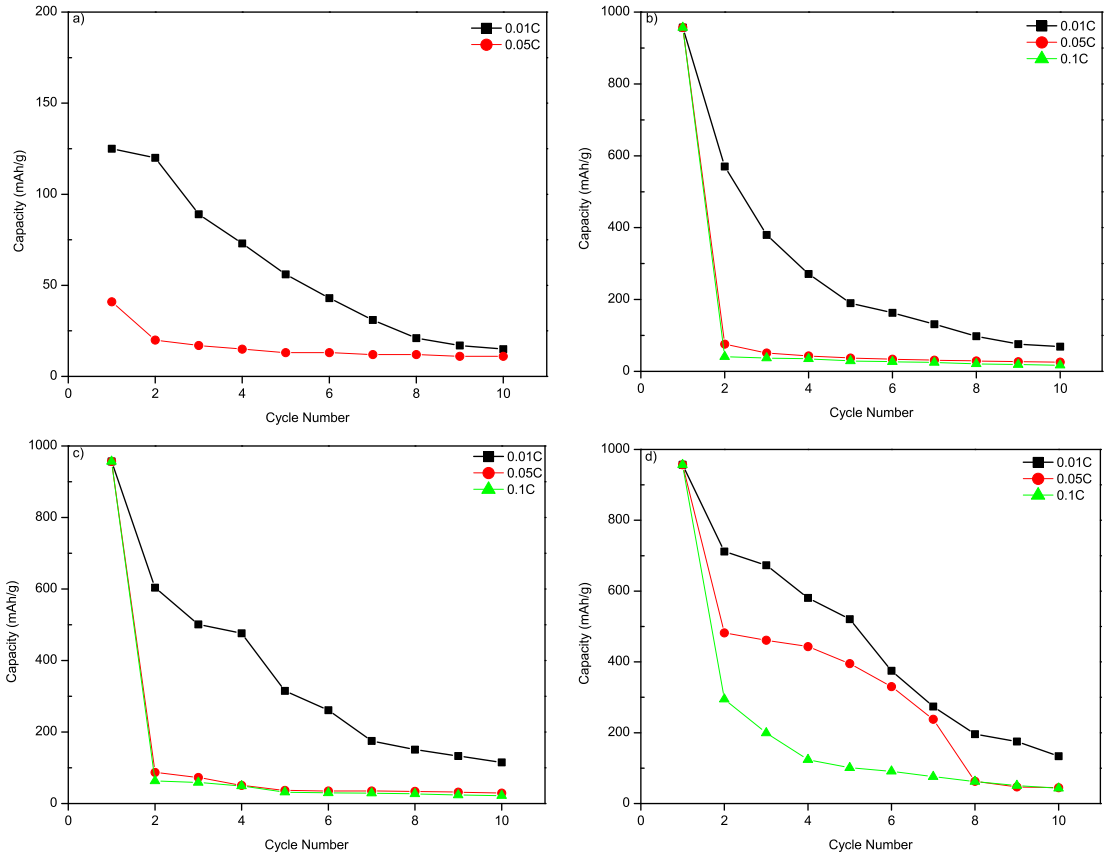

Figure 5.7: The cycling capacities of samples CP (a), BM (b), BM_c (c) and NC (d) at a charge rate of C/100 and a discharge rate stated in the figures.

which cause the electrode to crack. This cracking can then detach particles allowing them to be dissoluted into the electrolyte and become electrically isolated from the current collector. Figure 5.8 shows the cracking of the NC electrode after it was cycled ten times. It is clear that the volume change in cycling causes some of the particles to break off which could further reduce the capacity after cycling.

The cycling figures shows that there is rapid capacity fade during cycling, however this may not always mean the battery is inefficient. If the ratio of discharge capacity to charge capacity is high, it would mean that the reversible efficiency of the cell is high. Figure 5.9 shows the coulombic efficiency curves for the tested samples. It can be seen that there is no real relationship between the discharge rate or cycle number and cycling efficiency. There is no correlation that allows a prediction to be

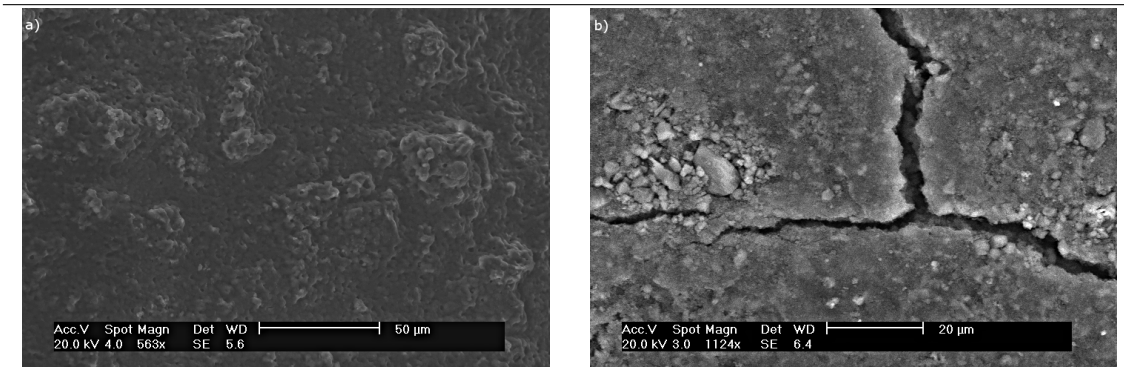

Figure 5.8: SEM images of the NC sample electrode before (a) and after (b) ten cycles

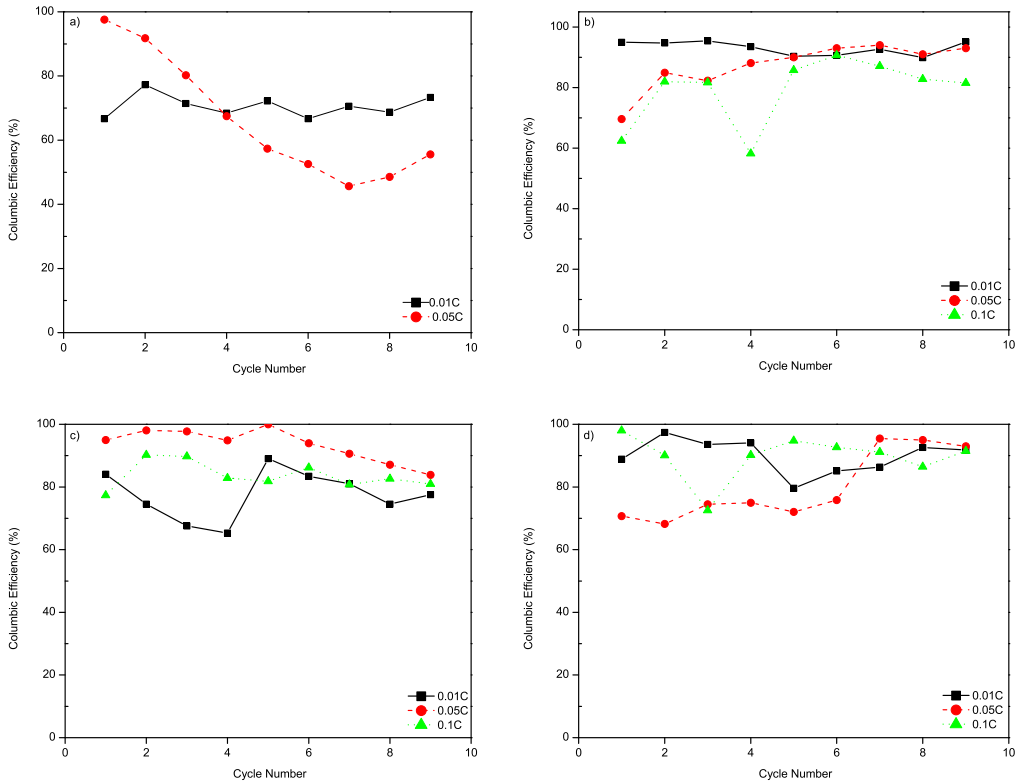

Figure 5.9: The Coulombic efficiency graphs of samples CP (a), BM (b), BM_c (c) and NC (d).

made from the amount of capacity charged and the capacity on the next discharge. The efficiencies range from 100% to around 60% and is not sample dependant.

To further test the onset of polarisation between a fresh cell, a cell discharged over one cycle and a cell charged and discharged over ten cycles electrochemical impedance tests were performed. The equivalent circuit that was used is that de-

scribed in chapter 4.6. Only samples BM, BM_c and NC were analysed with EIS due to the initial low capacity of sample CP.

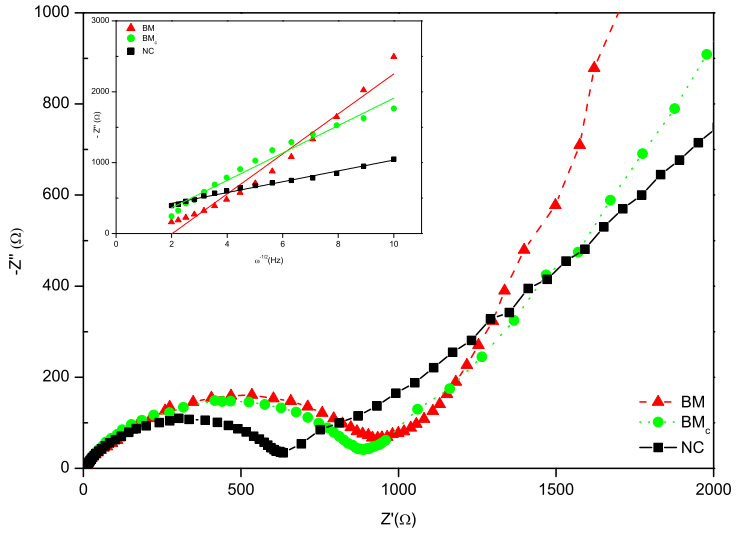

Figure 5.10: Nyquist plots of sample BM, BM_c and NC before first discharge. The inset figure is a plot of -Im Z against square root of frequency.

Figure 5.10 shows the impedance of the samples before any discharge tests were carried out and after the cell was rested to reach equilibrium. The intercept with $Z'\Omega$ at the high frequency region of the Nyqvist plot corresponds to the ohmic resistance between the electrolyte and the electrode. These areas are all equal as should be expected as all the cells are in the same state, with no current being passed through them. The radius of the semi circle in the medium frequency range, which reduces in size for the three different samples indicates the charge transfer resistance. It is suspected that the reduced sample size and coating increases the conductivity of the material, and the lithium ions and electrons can transfer with increased speed. The reduction in size of the medium frequency range semi circle confirms this. An increased charge transfer resistance indicates a larger semi circle. The inclined line in the low frequency region relates to the Warburg impedance and is plotted against the square root of the frequency in the insert to Figure 5.10, this relates to the lithium ion diffusion through the material. For the three samples it

can be seen that sample BM has the largest Warburg impedance and the NC has the smallest which also confirms that reduced particle size and coating has a positive effect on increasing the diffusion properties of aluminium fluoride.

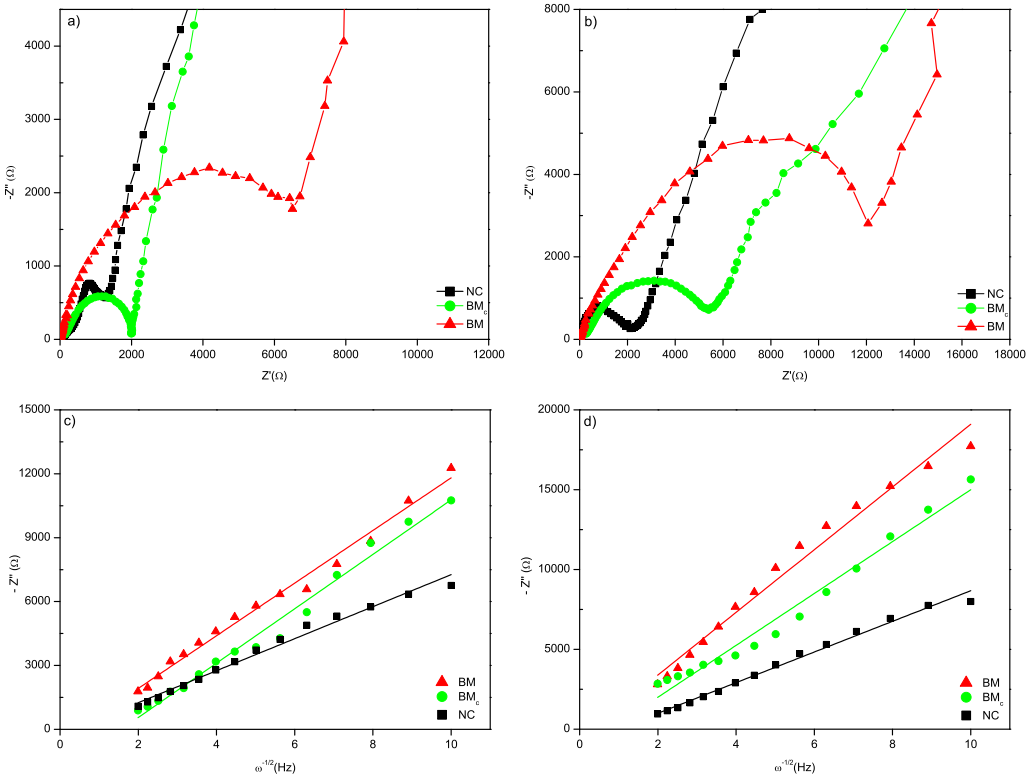

Figure 5.11: Nyquist plots of sample BM, BM_c and NC after first discharge (a) and ten (b) cycles.

Figure 5.11 shows the impedance data after the first discharge and after ten charge discharge cycles and -Im Z against square root of frequency to give an understanding of the diffusion of lithium through the cell. It shows that the impedance of the cells increases quite dramatically after only a few cycles, even after one discharge, indicated by the increase in the Z′Ω intercept in the high frequency intercept and the increase in the semi-circle in the medium frequency range. The rise in this impedance is a combination of an increase in charge transfer resistance, polarisation throughout the interphase between the electrolyte and material and a decrease in the diffusion properties of the lithium ion in the solid. The increase in charge transfer resistance is due to electrode losses due to the potential determining ions being inhabited while

Table 5.3: R_s and R_{ct} values of samples BM, BM_c and NC from Figures 5.10 and 5.11.

	R_s (Ω)			R_{ct} (Ω)		
Sample	Fresh Cell	After first discharge	Ten cycles	Fresh Cell	After first discharge	Ten cycles
BM	8.121	69.27	139.2	621.4	4021	6850
BM_c	7.871	32.77	78.21	476	1034	2450
NC	7.611	21.18	61.21	331.1	863.1	1105

Table 5.4: Exchange current densities for samples BM, BM_c and NC.

	i_o ($\times 10^{-5}$ A/cm^2)		
Sample	Fresh Cell	After first discharge	Ten cycles
BM	4.06	0.62	0.37
BM_c	5.30	2.44	1.03
NC	7.63	2.93	2.28

trying to pass through the electrode electrolyte phase boundary by the formation of a foreign substance on the electrode surface due to adverse reactions with the electrolyte. This adverse reaction also restricts the current due to concentration changes of the electroactive species at the electrode surfaces, resulting in low current density discharges behaving as if there was a high current passing through the cell, and the discharge profile showing a large drop in voltage with respect to the first charge. This is evident in the discharge profiles in Figure 5.5.

Table 5.3 shows the impedance data for R_s and R_{ct} for the samples BM, BM_c and NC over the ten cycles. It can be seen that as the cycles increase both the resistances increase due to reactions occurring within the cell.

By using the value of R_{ct} the exchange current density can be calculated by equation 2.13. The values for i_o are shown in Table 5.4 and show how the electron transfer decreases over number of cycles, confirming that the reduced capacity fade is partly due to reduced electron diffusion through the electrolyte and electrode.

The Warburg impedance also increases indicating that the diffusion of the lithium ions also decreases over cycling. This decrease can be attributed to the polarisations mentioned earlier.

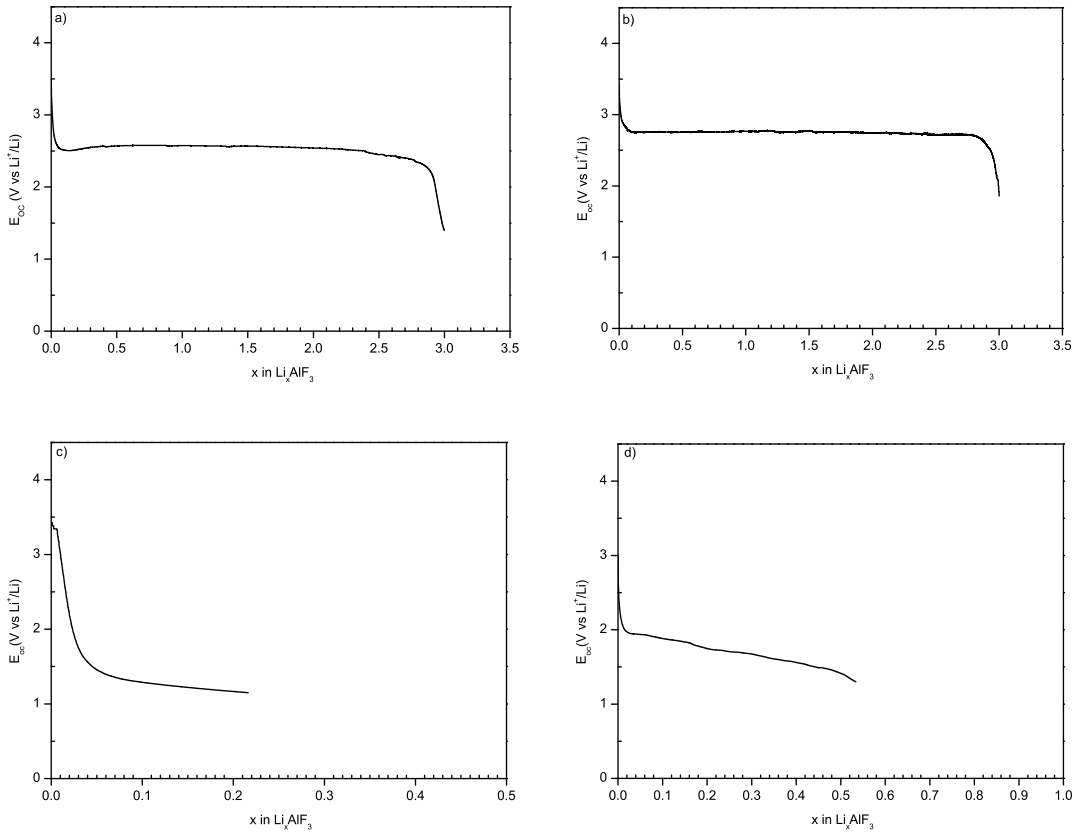

Figure 5.12: Galvanostatic titration curves of fresh cells for samples BM (a) and NC (b) and cells cycled ten times for samples BM (c) and NC (d).

By using equation 4.12 the Li^+ diffusion coefficients can be calculated for the fresh, discharged and charged BM and NC samples, and are shown in Table 5.5. Only the BM and NC samples were calculated to get a comparison of a poorly conducting sample with a good first discharge capacity and a more conductive sample. It can be seen that the lithium diffusion coefficient is two orders of magnitude higher for the NC sample in a fresh cell. However, this rapidly diminishes and after the first discharge all the cells have similar lithium diffusion coefficients. Upon further cycling it is interesting to see that sample NC has a higher diffusion coefficient, this can be attributed to the carbon nanocomposite which is improving the conductivity slightly through the cycling period and suppressing formation of a detrimental foreign surface coating on the electrode.

Table 5.5: Lithium diffusion coefficients for samples BM, BM_c and NC.

	D_{Li} ($\times 10^{-16}$ cm^2/s)		
Sample	Fresh Cell	After first discharge	Ten cycles
BM	2.90	0.14	0.06
NC	100	0.45	0.25

The galvanostatic titration curve can also be used to estimate the total ohmic drop in voltage from a cell under a current and one that is not. All the samples suffer an ohmic drop from their respective titration curves but the less so for the more conducting samples. The initial discharge profile for the BM sample was 2.15V which dropped from an open circuit of 2.5V and the NC sample dropped from 2.8V to 2.4V. Indicating the improved kinetics due to reduced particle size and a conductive coating help with the electron conductivity and lithium diffusion through the electrode.

Figure 5.13 shows what could be happening. As the aluminium fluoride breaks down the interphase between the electrolyte and lithium fluoride hinders the transport of new lithium ions that would react to the aluminium fluoride nearer to the current collector. This can contribute to the increase in charge transfer resistance and the decreased diffusivity through the electrode solid. By coating and reducing the particle size there is a quicker way for the lithium ions and electrons to reach the solid electrode and diffuse through the interphase layer between electrolyte and electrode. However, due to the morphology and relatively large particle sizes the reaction happens in a agglomerate preventing material blocked by the agglomerate from being reacted with.

Figure 5.14 shows the cyclic voltammetry curves for CP and NC to give a direct comparison of an irreversible and a reversible sample of aluminium fluoride. There is a clear reduction peak for NC between 2.5V–1V which is consistent with the discharge profiles in the previous figures. However the CV curve for CP does not show a clear reduction peak but a small reduction curve around 1.5V, which is probably

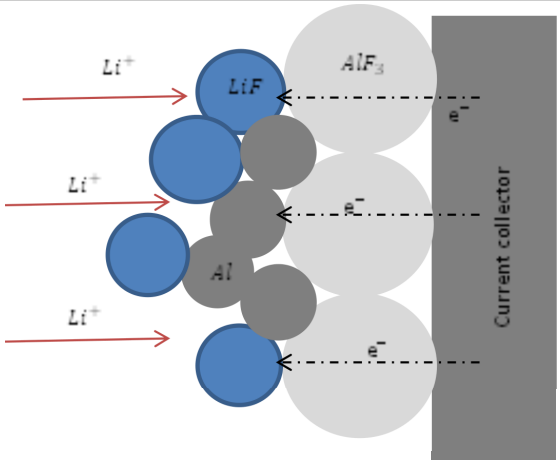

Figure 5.13: Schematic diagram of lithium diffusion in electrolyte and electrode.

due to the reduced kinetics of the pristine material compared to the nanocomposite material.

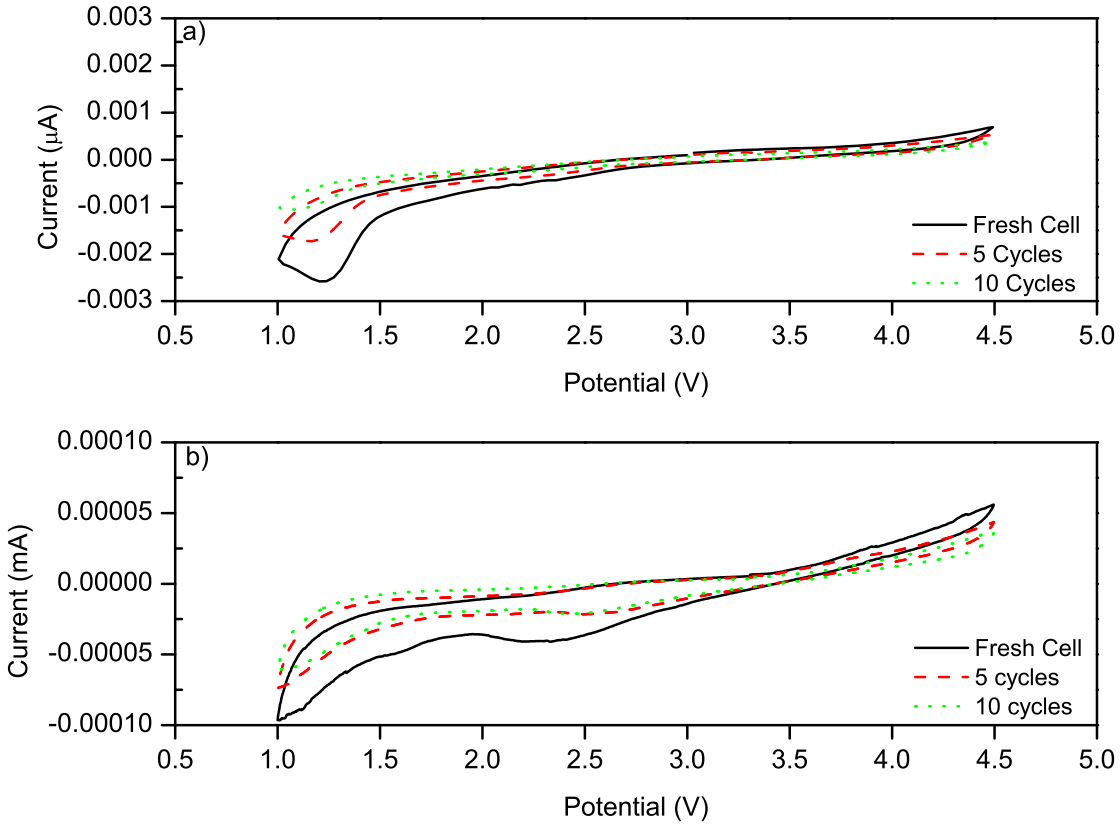

Figure 5.14: Cyclic voltammograms of CP (a) and NC (b). Scan rate $0.1 mVs^{-1}$ and after a different number of cycles as indicated in the figures.

There is not a distinct charging plateau for the CP sample but the increase in current for the NC sample after 3.5V indicates that there is an oxidation of LiF and Al occurring, however small. After the sample is cycled it can be seen that the reduction and oxidation peaks decrease as the polarisation through the material increases and no reversible capacity can be observed.

Using the Randles-Sevcik equation (4.9) the chemical diffusion coefficient of the Li ion in AlF_3 can be determined. The peak current is taken from figure 5.14 and the concentration is determined by the state of charge of the sample at the voltage peaks in said figure. The concentration was calculated using equation 5.1 where x is the state of charge of the cell, 83.98 is the molecular mass of aluminium fluoride and 2.88 is the density. The state of charge was taken to be 0.01% at the cathode and 99% at the anode.

$$C_{Li} = \frac{x/3}{83.98} \times 2.88 \tag{5.1}$$

The electrode electrolyte surface area was taken to be the surface area of the particles, due to the reaction taking place over the whole surface and not in any particular dimension. R is the universal gas constant and T is the temperature in kelvins, the experiment was recorded at.

Table 5.6 shows how the diffusion coefficients for the fresh cell increased by a factor of a hundred with the carbon nanocomposite. These values are still extremely low so that the diffusion is hindered considerably by the material kinetics and this contributes to the poor capacity retention during cycling.

Table 5.6: Anodic and cathodic diffusion coefficients for fresh, after first discharge and after ten cycles cells, for samples CP and NC.

	Anodic D_{Li} ($\times 10^{-25} cm^2/s$)			Cathodic D_{Li} ($\times 10^{-17} cm^2/s$)		
Sample	Fresh Cell	Five cycles	Ten cycles	Fresh Cell	Five cycles	Ten cycles
CP	0.008	0.005	0.002	0.081	0.042	0.019
NC	3.598	2.024	1.599	9.795	5.510	3.526

Further studies will be needed to confirm the cyclability mechanism and the reversibility of this material but initial investigations look promising that it can be used as a high capacity reversible electrode material. If this is not the case it can still be used as an alternative low cost material in primary batteries as it has a specific energy density comparable to carbon fluoride primary batteries [118, 15].

5.4 Conclusion

Initial investigations were carried out to see if AlF_3 is a possible high capacity electrode material for lithium batteries. Micron and nanometer uncoated, coated and carbon nanocomposite sized particles were tested in CR2032 coin cells at charge discharge rates of 0.01C, 0.05C and 0.1C for 10 cycles. Initial discharge capacities were shown to be around 100mAh/g for the micron sized particles and around 957mAh/g for the other nanometer sized particles, at around a plateau ranging from 2.15 - 2.4V, giving specific energy densities of over 2057 Wh/kg, higher than many commercial materials. The charge discharge experiments showed that the material was reversible but the specific capacity decreased to less than 5% of the initial discharge capacity after 10 cycles. This initial capacity fade was partly related to the poor kinetics of the materials as confirmed by the conductivity and impedance measurements. The higher the conductivity the lower the impedance and the better the specific capacities.

Initial experimental data show promise in the reversibility of this high capacity material and the next step is to understand the mechanism more clearly to see what the best route is in order to improve the rate capacity and cycle life.

Chapter 6

Investigation of the Redox Reaction of Aluminium Fluoride

6.1 Introduction

With capacities reaching theoretical values of 957mAh/g it is clear that there is a full reduction process of Al^{3+} to Al^{0}. However, upon repeated cycling this full reduction does not occur, due to either the oxidation process being inefficient, by being hampered by the reduction products, or a detrimental reaction with the electrolyte. It is the inefficiency in the cycling that would have to be improved to make the material suitable for use in applications which require a long cycle life. From previous results it is also shown that there is a one stage discharge plateau, for the initial discharge this is around 2V, and for subsequent discharges this regresses to 1.6V and to around 1.2V for the last few cycles. The high voltage discharges around 2V occur with a steady flat profile whereas the subsequent discharges result in a sloping profile. The aim of this chapter is to determine what is happening to this material as it undergoes reduction and oxidation.

6.2 Experimental

The cells electrochemically tested in the previous chapter were characterised by ex situ TEM, DF, SAED and ex situ XRD. The ex situ XRD samples were tested by disassembling the electrochemical cell in a Ar filled glovebox and rinsing the electrode in dimethyl carbonate (DMC). The dried electrode was then placed on a glass slide and covered with kapton film using a seal layer of vacuum grease. Ex situ TEM samples were prepared by disassembling the coin cells under argon, the electrode rinsed and dispersed in DMC and a few drops of the dispersion was placed onto a carbon film supported on a copper grid.

6.3 Results and Discussion

The full reduction of Al^{3+} to Al^0 is clearly shown in Figure 6.1 with the flat discharge profile reaching theoretical capacities and a full three electron transfer. It is believed that the reduction process of AlF_3 follows equation 6.1 to form LiF and Al. This would explain the flat discharge profile seen at around 2.4V. However, this reduction would result in a large structural rearrangement from an R$\bar{3}$C structure to a Fm$\bar{3}$m structure. This is due to the breaking of all the Al-F bonds.

$$3Li^+ + 3e^- + AlF_3 \longrightarrow 3LiF + Al \tag{6.1}$$

A NC sample (preparation details explained in chapter 5) was reduced to 1V so the reaction products could be determined. Figure 6.2 shows the ex situ XRD results. Two compounds were identified in the ex situ XRD pattern LiF and Al which is consistent with a conversion reaction in equation 6.1.

To further corroborate the ex situ XRD results selected area electron diffraction

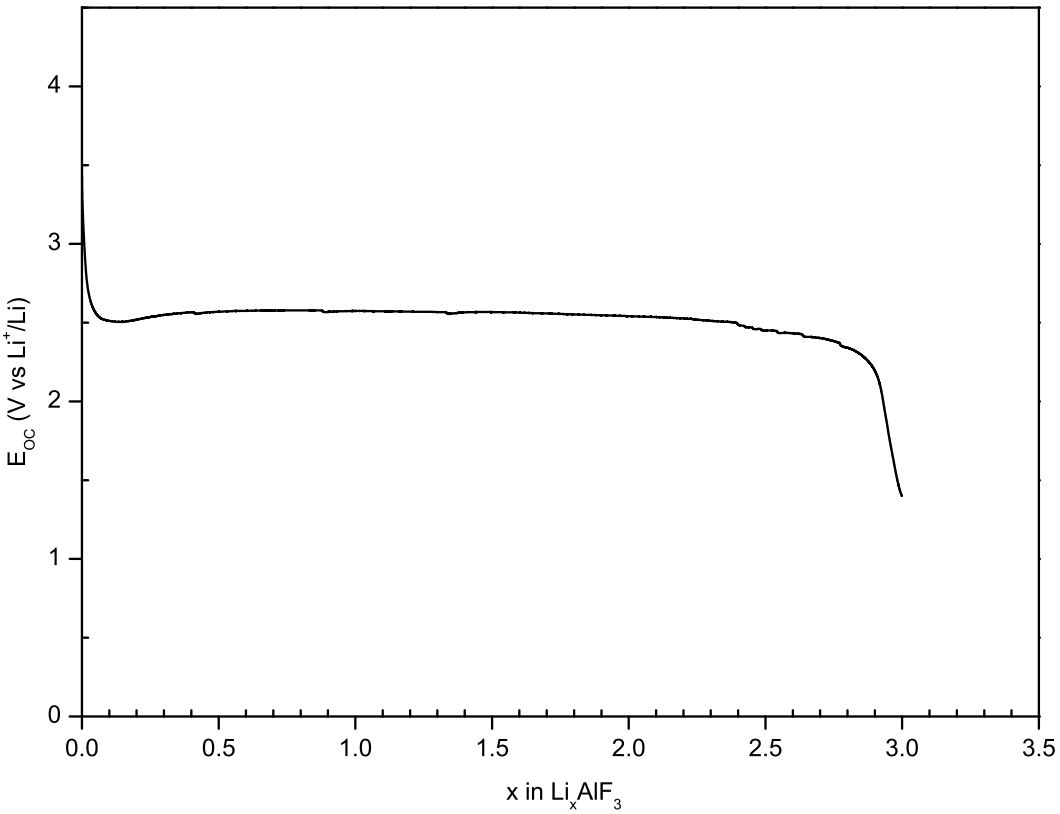

Figure 6.1: Galvanostatic intermittent titration discharge profile of sample NC

patterns were taken on the discharged sample. Figure 6.3 shows two fields for the sample at room temperature. The d-spacings of the diffraction circles can be calculated and are shown in Table 6.1 against the JCPDS standards.

Table 6.1: d-spacings derived from SAED pattern with a cell fully discharged to 1V. The standard LiF and Al are shown as reference.

1V Field 1	LiF - $Fm\bar{3}m$ Standard	1V Field 2	Al - $Fm\bar{3}m$ Standard
2.303	2.325 (111)	2.322	2.338 (111)
2.017	2.013 (200)	2.052	2.031 (200)
1.430	1.424 (220)	1.488	1.432 (220)
1.200	1.214 (311)	1.219	1.221 (311)
1.177	1.163 (222)	1.178	1.169 (222)
1.024	1.005 (400)	1.010	1.012 (400)

The broad diffuse diffraction patterns in Figure 6.3 indicate small crystals a few nanometers in size. Field 1 had calculated d-spacings which agreed enough with the JCPDS standards to confirm that LiF was one product. Field 2 also had calculated

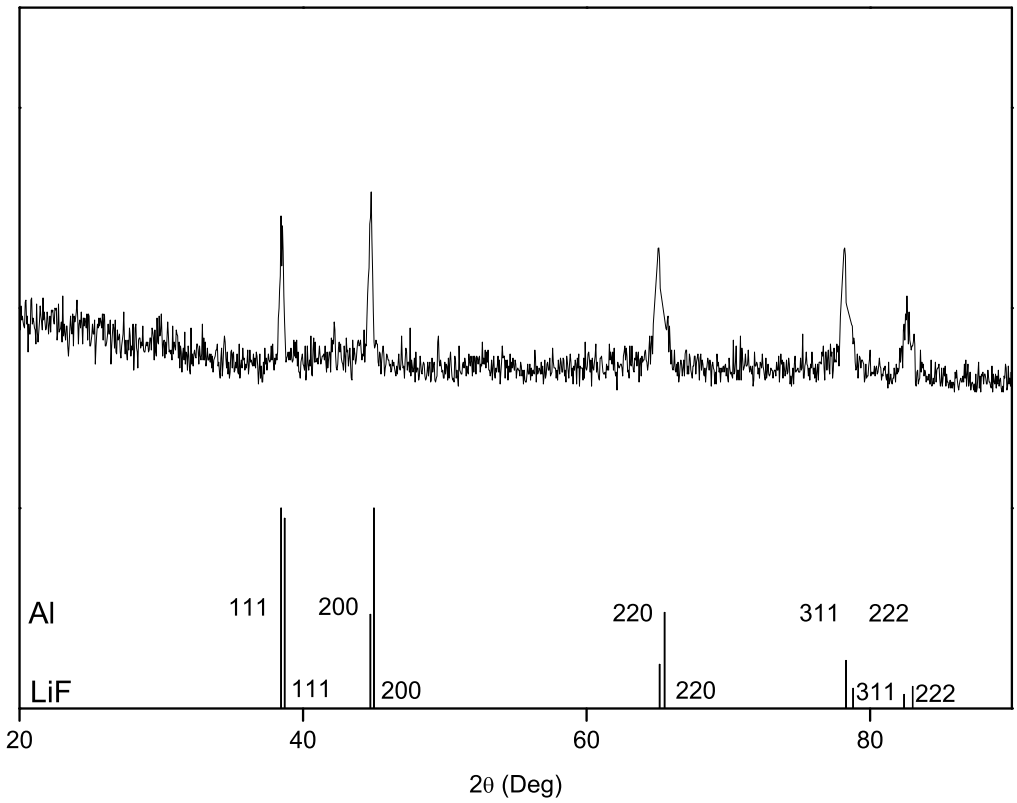

Figure 6.2: Ex Situ XRD of sample NC discharged to 1V. The columns represent the lattice parameters of the identified materials.

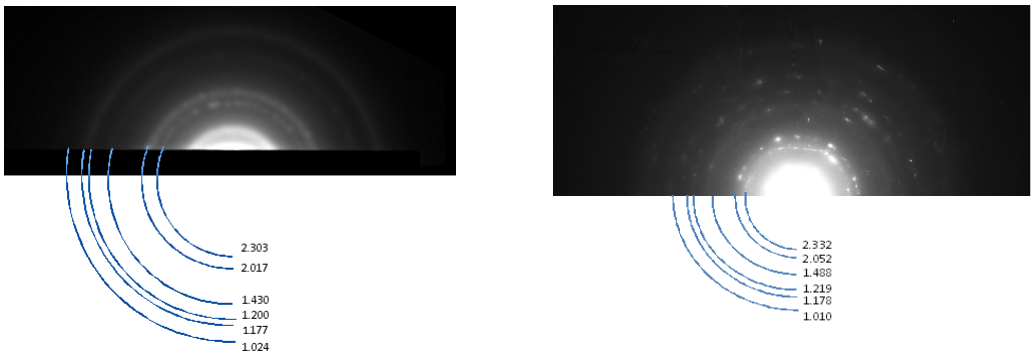

Figure 6.3: Selected area electron diffraction pattern of sample NC discharged to 1V. Image (a) is of field one the lithium fluoride product and image (b) is of field 2 the aluminium product.

d-spacings which agreed enough with the JCPDS standards to confirm that Al was also a product agreeing with the conversion reaction in Equation 6.1 and the ex-situ XRD patterns in Figure 6.2.

The crystallite sizes were calculated using equation 4.3 for peaks (111) and (220) and were 17nm and 11nm in size. This is slightly larger than the crystallites found when FeF_3 was reduced to LiF and Fe but that can be attributed to larger cell parameters of 286.65 pm for iron and 404.95 pm for aluminium. The crystallite sizes are smaller than they were before the reduction process as determined in chapter 5.

It seems that the reduction mechanism from Al^{3+} to Al^0 is explained by the one stage discharge plateau and the subsequent forming of LiF and Al nanocomposite. Due to there being no further voltage profile and the plateau is flat this can be attributed to the reactants and products both forming solid phases. This can be confirmed by the polycrystalline nature of the SAED patterns.

Upon oxidation it is believed that the Li-F bonds can be broken and then the F reforms with Al to form AlF_3. This oxidation reaction is associated with a $3e^-$ transfer and subsequent discharge reactions maintained characteristics of the initial compound, a one stage profile between 2.6V and 1V.

Figure 6.4 shows the ex situ XRD patterns for discharged cells which were then recharged to 3V, 3.5V and 4.5V. These potential values were used because it was clear that the charge profile was not at the same voltage as the discharge profile. Upon oxidation it is seen that the Bragg peaks at 38° (2θ) and 43° (2θ) reduce in intensity as do the peaks at 63° (2θ) and 78° (2θ) respectively. This is associated with the oxidation of the LiF and Al products formed upon discharge. At 3V there is the emergence of peaks around 20° (2θ) which is indicative of AlF_3 reforming and the peaks of LiF and Al start to reduce. Upon further charging to 3.5V the LiF and Al peaks start to become more pronounced which could be due to the reduction in amorphous nature and the crystal structure being more defined as it is oxidising to reform AlF_3. It is at this stage that the AlF_3 peaks become more pronounced and more intense suggesting that AlF_3 is reforming. At this voltage there still seems to be some LiF and Al implying that not all the material has oxidised, or that there

has been some dissolution of the LiF and Al into the electrolyte. At the final charge voltage of 4.5V it is clear that AlF_3 has reformed due to the large intensity peaks, however there are still some residual LiF and Al peaks indicating the oxidisation did not occur to all the LiF and Al. This could explain why the theoretical capacity could not be achieved upon the second discharge, not all the LiF and Al had oxidised to reform AlF_3. However there does not seem to be any peaks that indicate the adverse reaction of the $LiPF_6$ electrolyte with AlF_3 and no peaks that indicate there is an intermediatory phase. These results show that some reversibility is present but due to the poor kinetics and a high overpotential the reversibility is not efficient. The kinetics of the material can be a major contributing factor to poor oxidation of the reactants due to no anomalous species being present in the electrolyte. Ex situ SAED was also used to confirm this and the SAED pattern of a reconverted region showing AlF_3 can be seen in Figure 6.5. The subsequently calculated d-spacings are shown in Table 6.2 confirming AlF_3.

Table 6.2: The d-spacings derived from the SAED pattern in Figure 6.5 with a cell fully charged to 4.5V. The standard AlF_3 d-spacings are shown as reference.

Cell charged to 4.5V	AlF_3 - $P63mmc$ Standard
5.892	5.981
3.536	3.551
3.431	3.457
3.011	3.001
3.051	3.079
2.391	2.486

The increased spot development on the SAED pattern in figure 6.5 is attributed to the reformation of the AlF_3 compound and the diffuse rings indicate small crystal structures. The peaks differ significantly from the discharged sample indicating that some form of oxidation has occurred and with collaboration from the ex situ XRD it can be put down to the oxidation of LiF and Al to form AlF_3 as the calculated d-spacings, match the JCPDS standards.

The fact the oxidation process does occur shows that the material is reversible,

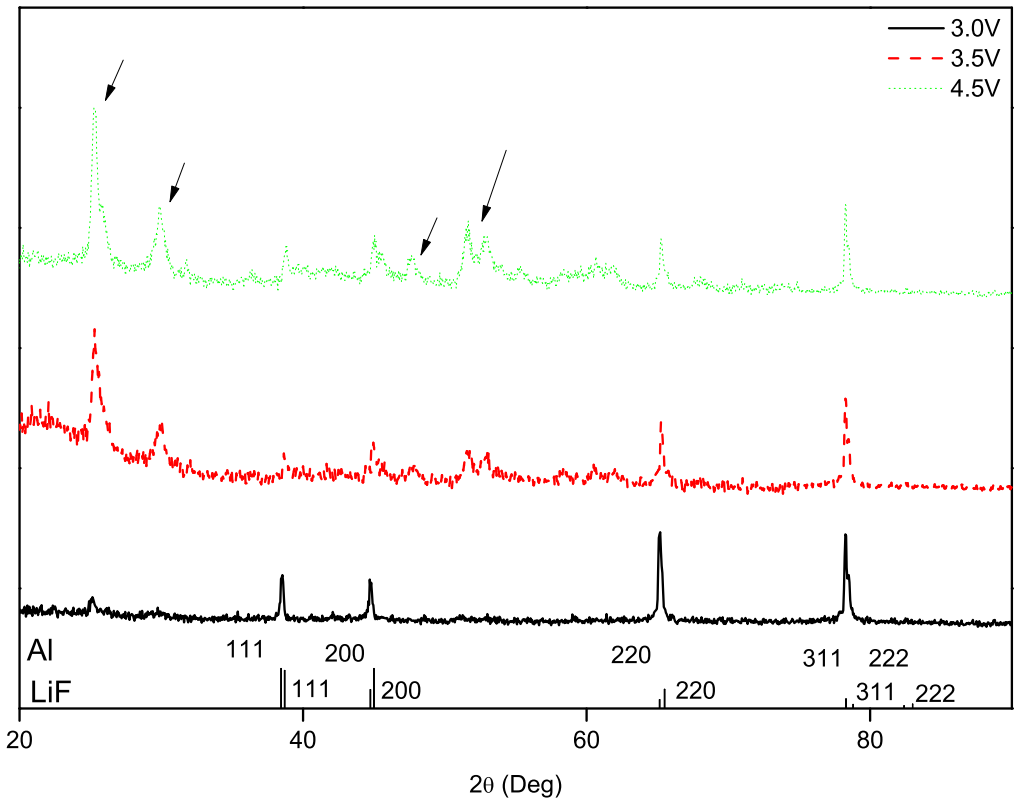

Figure 6.4: Ex Situ XRD of sample NC charged to 4.5V. The columns represent the lattice parameters of the identified materials and the arrows indicate the aluminium fluoride peaks. The voltage the sample was charged to is indicated.

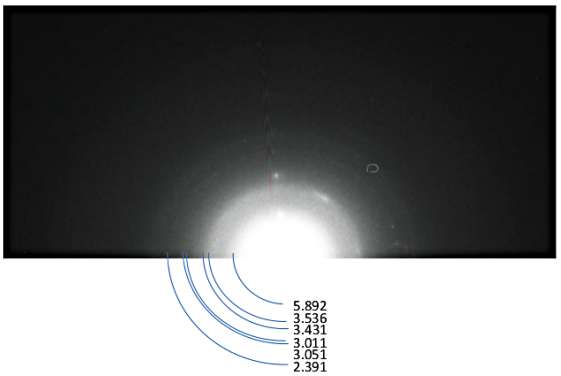

Figure 6.5: Selected area electron diffraction pattern of sample NC charged to 4.5V.

however, there are some inefficiencies that result in poor capacity retention. The initial thought is that upon reduction of AlF_3 there is an adverse reaction with the electrolyte resulting in an added phase which does not oxidise back into AlF_3. However, during the discharge analysis not enough side product was found that could reduce the capacity by 26% on the subsequent discharge.

One problem with conversion reactions is the structural change upon cycling. The reconverting from one compound to another degrades the integrity of the electrode resulting in cracking, this is confirmed by Figure 6.6 which shows an electrode after one charge discharge cycle.

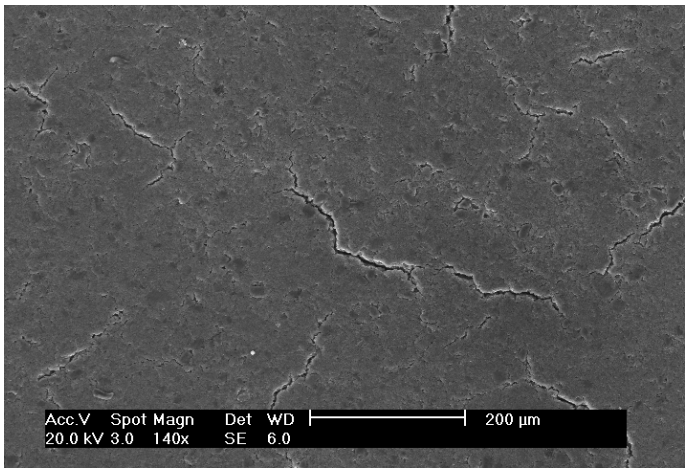

Figure 6.6: SEM image of cracked electrode after one cycle

This could result in the dissolution of material into the electrolyte as it breaks off from the electrode. This would also have the effect of there being particles that are not bound to an electrically conductive network of carbon or current collector, making it being a passive material not undergoing any reaction, or the current being too high for the particular particle due to the materials poor kinetics. It was found that upon disassembling the cell that there were loose pieces of electrode in the electrolyte which could contribute to the loss in capacity.

It was found as detailed in chapter 5 that after a few cycles the capacity dropped considerably and instead of a flat plateau there was a plateau that had a sloping

profile. This sloping profile is thought to indicate that the reactants and products are both in liquid and solid solution whereas the flat profile indicates the reactants and products form two distinct solid phases [10]. As the sloping profile is only apparent after the first discharge the reconversion to AlF_3 from LiF and Al could be responsible due to a reaction between one of those products and the electrolyte. Over repeated cycling one of the reduction products could incorporate into the electrolyte either substitutional or interstitially. Figure 6.7 shows the ex situ XRD of a NC sample cell cycled ten times. The peaks indicated are those of Li_3AlF_6 which was found amongst LiF, Al and AlF_3 peaks. This indicates that upon cycling LiF reacts with some of the AlF_3 to form Li_3AlF_6. This product can be regarded as a solid solution of LiF and AlF_3 [124] and can explain the sloping discharge profile. This can also explain the rapid capacity fade as some of the formed AlF_3 reacts with LiF to reduce the actual amount of AlF_3 available for the next charge.

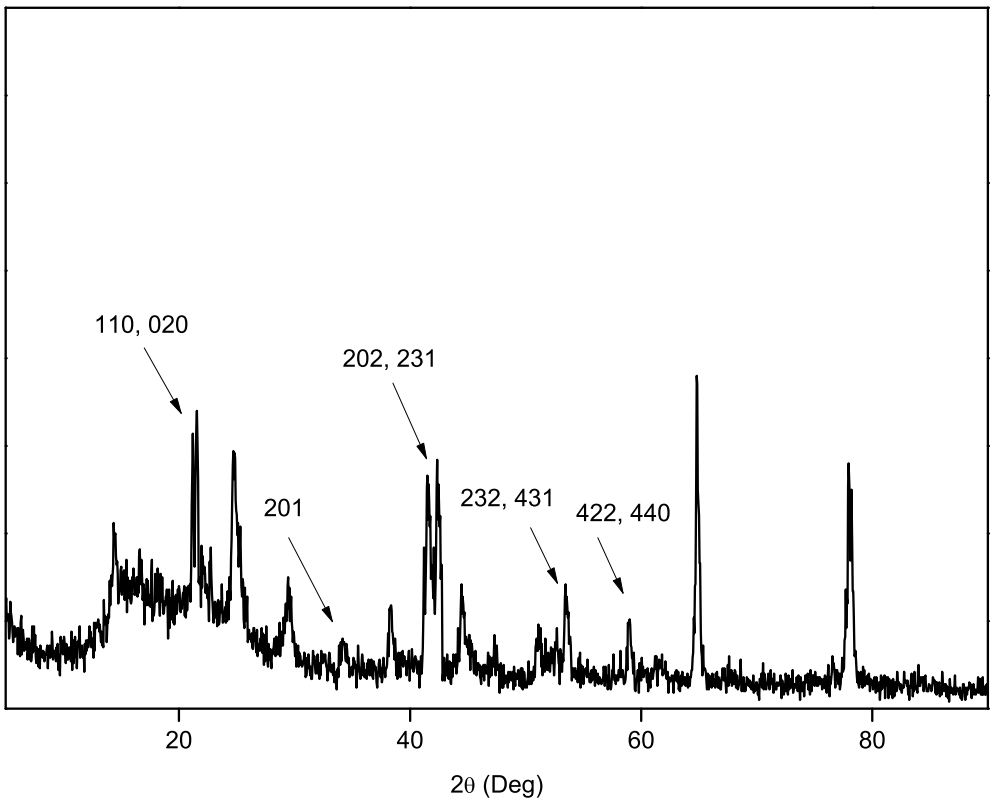

Figure 6.7: Ex situ XRD after ten cycles

Both these processes affect the properties of the material by distorting the crystal lattice and disrupt the electrical and physical homogeneity of the solvent material which could also explain the increased charge transfer resistance, and resistance between electrode and electrolyte interface through the cell, as discussed in chapter 5. The cracking of the electrode and dissolution into the electrolyte could also enhance this process and would also account for the loss of capacity witnessed in subsequent cycles. The reconverted crystal size calculated from peaks (100) and (004) were 19nm and 49nm respectively indicating a size increase of over 200%. The initial particle size of around 100nm for the samples undergo a size reduction of over 90nm in the first discharge. They then at least double in size on the subsequent charge. This size fluctuation is enough to understand why the electrode cracks upon repeated cycling.

It is also known that once the initial particles are reduced they form a nanocomposite of LiF and Al as can be seen in Figure 6.8. The dark field sample (a) in the figure is the sample before it is discharged. The dark area is the carbon and the light areas are the AlF_3. It can be seen that there is a large amount of active material combined together to form a nanocomposite with the AlF_3 particles being roughly the size determined from the NTA analysis in chapter 5. Upon discharge it can be seen in (b) that the products are much smaller and seem to form areas rich in LiF and Al as confirmed by EDX. This product of LiF and Al sits in a a nanocomposite of the two where there is a different bonding nature of LiF (ionic) and Al (metallic). This large surface contact interface results in a large energy requirement to be put into the system to overcome. This is one explanation to why the charge profile is so much higher than the discharge profile, as recorded in chapter 5. It may be possible to further increase the charge voltage to see if a higher capacity can be achieved upon a second discharge, however this would require a high voltage electrolyte as $LiPF_6$ starts to oxidise at higher potentials than 4.5V. The increase in charge profile could also be due to the cracking of the electrode causing a larger impedance due to

reduced electrically conductivity through the electrode. By reducing the cracking it may increase subsequent discharge capacities.

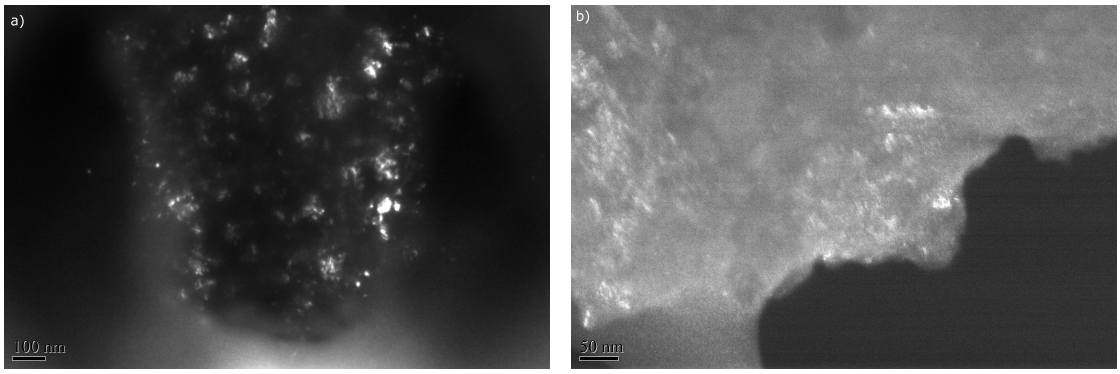

Figure 6.8: Dark field image of sample NC before discharge (a) and after discharge (b).

6.4 Conclusion

The reversible conversion reaction of aluminium fluoride was shown to follow the reduction of AlF_3 into LiF and Al during discharge and upon charge LiF and Al would oxidise to form AlF_3 again. Even though not all the LiF and Al was oxidised this was put down to combination of a large voltage required to over come the large surface/interfacial energy produced by the production of nano LiF and Al particles and the large reduction in size from the initial particles to the reduced phase, which resulted in the cracking of the electrode reducing the amount of active material there is to oxidise, which also increased impedance through the cell. The formation of Li_3AlF_6 from AlF_3 and LiF during the short cycle life of the cell also indicates there is unwanted side reactions with the $LiPF_6$ electrolyte, with the lack of capacity in subsequent discharges attributed to this phenomenon. It is clear that this material is reversible it is just a matter of finding the right engineered electrode and compatible cell electrolyte to improve the cyclability.

From here there are a few routes to improve this material. One is to synthesise smaller particles so that the initial size reduction is not so great that it cause break-

ing of the electrode and to increase conductivity through the material. For the first charge this seemed to be one of the larger contributors to not realising a rechargeable capacity near theoretical. The decreasing of particle size should also improve the material kinetics so faster discharge rates and even charge rates could be realised. Another route is to try and find a compatible electrolyte that does not form unwanted products and could perhaps even increase the charge profile upto 5V, with the idea to improve the cycle life and subsequent cycling capacities. An investigation of the mechanism of the SEI interphase and how it exists in relation to bulk AlF_3 interaction is another route that could be taken.

Chapter 7

A Facile Synthesis of Aluminium Fluoride Nanorods

The previous chapter showed that there is potential for aluminium fluoride to be used as a reversible cathode material. This chapter describes the synthesis of a new morphology aluminium fluoride powder which could have the potential to increase the rate capability and cycle life of the cathode material due to its decreased size.

7.1 Introduction

With particle sizes in the hundreds of nanometer range it was shown that aluminium fluoride can produce a reversible capacity of around 300mAh/g after 5 cycles and less than 50mAh/g after 10 cycles, at a low discharge and charge rate. Due to the insulating nature of aluminium fluoride it is necessary to reduce the particle sizes to a scale of tens of nanometers. Even reducing the particle size to tens of nanometers may not be enough due to the surface area of the material in contact with the electrolyte not being particularly large for spheres. By using a simple precipitation reaction we show that it is possible to synthesise aluminium fluoride nanorods which have a higher surface area than ball milled particles. The synthesis route was made

up of six variables, molar mass of surfactant, amount of surfactant, precipitation time, calcination time, calcination temperature and rate of cooling.

7.2 Experimental

The nanorods were synthesised by the method described in chapter 4. The structural characterisation was carried out by XRD and FT-IR and morphology was characterised by TEM and SEM.

7.3 Results and Discussion

7.3.1 Synthesis

Aluminium fluoride has been synthesised via thermal decomposition of fluoroaluminate salts or dehydration of aluminium fluoride hydrates. These methods lead to impurities of the fluoride due to partial decomposition or a reduced surface area [125, 126, 127, 128]. Alternative methods have been developed which use halogen acids or air sensitive precursors [129, 130, 131]. Aluminium fluoride can also be synthesised from a simple reaction of ammonium bifluoride and an aluminium salt described in chapter 4. The addition of 1.5M of ammonium bifluoride to the aluminium salt suspension reduces the aluminium nitrate and produces nitric acid, nitrogen and water as shown in equation 7.1:

$$10Al(NO_3)_3 + 15NH_4HF_2 \longrightarrow 10AlF_3 + 21HNO_3 + 12N_2 + 27H_2O \qquad (7.1)$$

After a few hours the aluminium fluoride precipitation can be observed in the solution. This precipitate can be separated by centrifugation and dried at 70° C. The

resulting powder is calcined to produce aluminium fluoride. The materials crystal structure, surface structure and surface area were investigated as a function of mixing time, calcination time, calcination temperature, cooling rate, molar mass of the surfactant and amount of surfactant.

Table 7.1: Synthesised samples with varying synthesis conditions. The variable that was changed is in bold. The reference samples are in italics.

Sample	PEG M_w	Percent of PEG	Mixing time (hrs)	Calcination temperature (°C)	Calcination time (hrs)	Cooling rate (°C / min)
Reference RW	4600	82	18	Not calcined	0	0
Reference A	4600	82	18	300	2	4
Reference B	4600	82	18	600	2	4
1	**300**	82	18	600	2	4
2	**20000**	82	18	600	2	4
3	4600	**820**	18	600	2	4
4	4600	**0**	18	600	2	4
5	4600	82	**5**	600	2	4
6	4600	82	**47**	600	2	4
7	4600	82	18	**400**	2	4
8	4600	82	18	**500**	2	4
9	4600	82	18	**700**	2	4
10	4600	82	18	**800**	2	4
11	4600	82	18	**900**	2	4
12	4600	82	18	600	**1**	4
13	4600	82	18	600	**4**	4
14	4600	82	18	600	2	**10**
15	4600	82	18	600	2	**1**
16 - (**Under Air**)	4600	82	18	600	2	4

Table 7.1 shows the samples that were synthesised and which variable was changed.

7.3.2 Variables that Affect Bulk Structure

X-ray powder diffraction measurements were taken on three reference samples. The reference samples used a surfactant with a molar mass of 4,600, were mixed for 18 hours, calcined at 2 hours and cooled at 4°C/min. The three reference samples were the raw powder designated Reference RW, which was not calcined, raw powder

calcined at 300°C designated Reference A and the raw powder calcined at 600°C designated Reference B. These three references were what the other samples were analysed against.

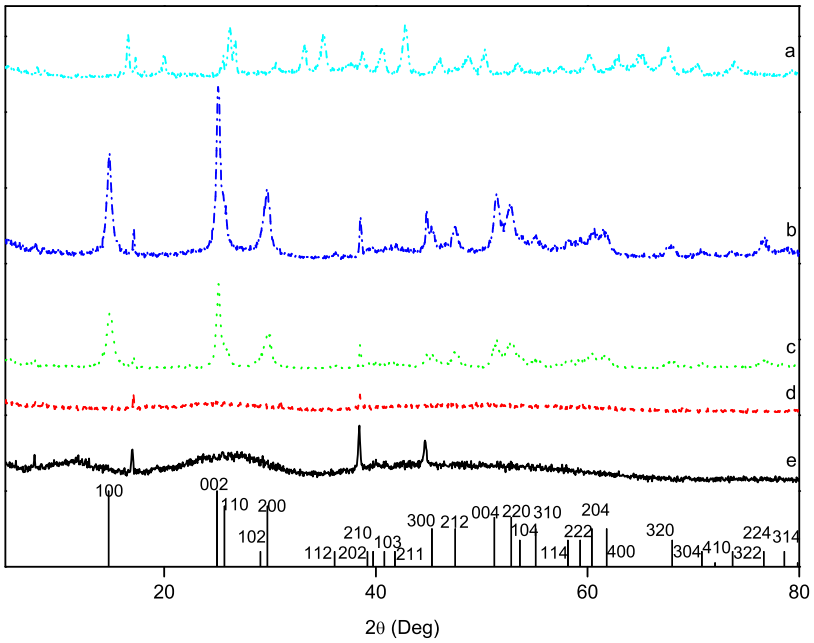

Figure 7.1: X-ray powder diffraction patterns of aluminium fluoride, sample 16 (a), bought powder (b), 600° C (Reference b) (c), 300° C (Reference a) (d) and 70° C (Reference RW) (e).

Figure 7.1 shows the X-ray diffraction pattern of the three samples against a bought sample of AlF_3 and sample 16. It shows that Reference RW is amorphous with no real crystal structure. The AlF_3 starts to crystallise at higher temperatures with some crystal structure being present in Reference A and then the full crystal structure being present in Reference B. The XRD measurements show that no crystalline oxide or hydroxide species were detected after calcination under argon. For the sample that was burnt under air the XRD pattern shows that no aluminium fluoride is present but many oxide and hydroxide species including aluminium oxide can be found. It is burning under argon that removes the oxide and hydroxide species that are present in sample 16. The only other variable that appeared to affect the crystalline structure of the material is the calcination temperature. The samples

that had the surfactant molecular mass, amount of surfactant, the mixing time, the calcination time and the cooling rate varied had similar crystal structures to Reference B as shown in Figure 7.2. The calcination temperature was 600°C for all these samples.

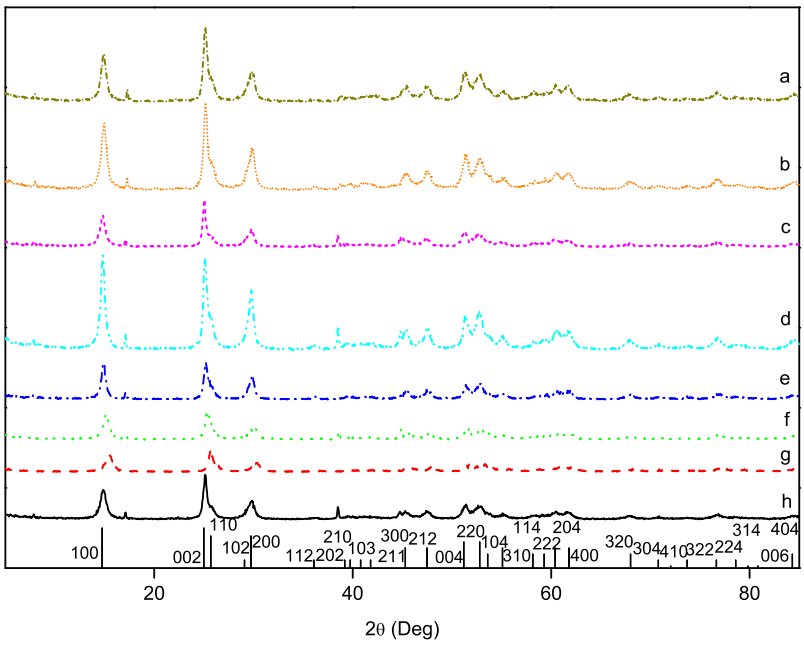

Figure 7.2: X-ray powder diffraction patterns of aluminium fluoride synthesised as a function of surfactant molecular mass, amount of surfactant, the mixing time, the calcination time and the cooling rate. a = Reference 7, b = Sample 6, c = Sample 5, d = Sample 4, e = Sample 3, f = Sample 2, g = Sample 1, h = Reference B.

The calcination temperature was varied between 300°C and 900°C in intervals of 100°C and the XRD patterns are shown in Figure 7.3. It shows that at 300°C there is still no definite crystal structure and is amorphous. Increasing the temperature by 100°C increases the crystallinity of the sample and aluminium fluoride forms. At higher temperature the crystal structure of samples changes from hexagonal lattice system with space group P63/mmc at temperatures up to and including 600°C to a rhombohedral lattice system with space group R3 at temperatures over 700°C.

The surface structure can be related to the bulk structure of the material. This being the case IR spectroscopy was used to characterise the surface of the three reference

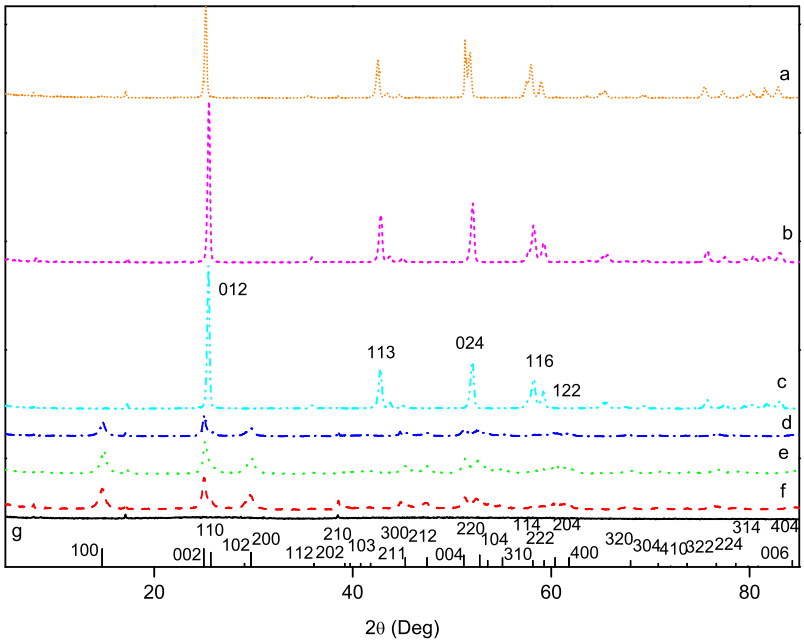

Figure 7.3: X-ray powder diffraction images of samples with different calcination temperatures.a = 900° C, b = 800° C, c = 700° C, d = 600° C, e = 500° C, f = 400° C and g = 300° C. The main lattice planes are indicated on graph c to indicate the rhombohedral lattice system.

samples, bought material, a high temperature sample and sample 16. Figure 7.4 shows the IR spectra of the reference samples. Reference RW shows that there is still moisture in the sample from the absorption bands at over 3000cm^{-1}. As the calcination temperature is increased the intensity of the signal decreases as should be expected. Reference RW also shows C-H and O-H deformation vibrations from between 1200cm^{-1} up to 1460cm^{-1} absorption bands which clearly decreases in intensity as the calcination temperature increases which can be attributed to the surfactant being removed at the higher temperatures. Throughout all the samples there is a clear rise in intensity at the low absorption band around 650cm^{-1} which can be attributed to the Al-F vibration.

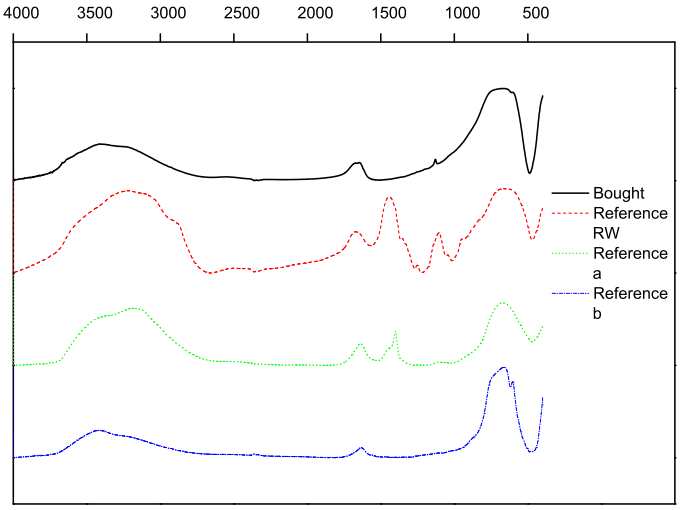

Figure 7.4: FT-IR results of the three reference samples and the bought aluminium fluoride.

7.3.3 Morphology

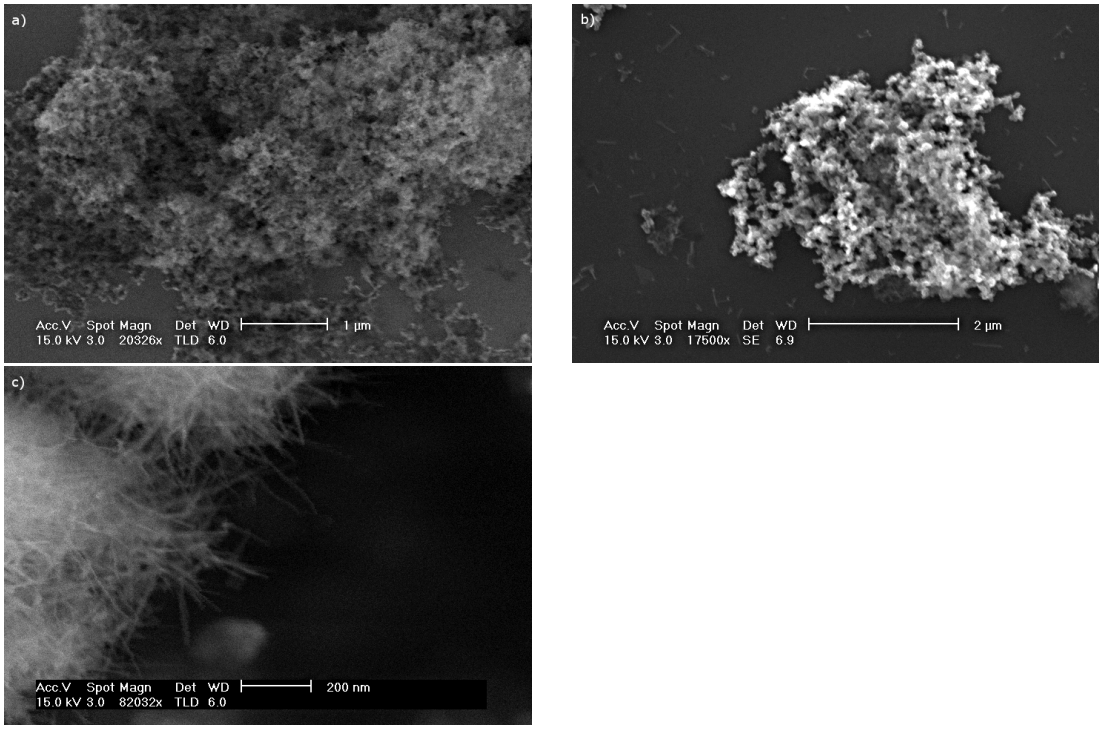

Figure 7.5: SEM images of AlF_3 nanopowder after heat treatment at (a) 70° C, (b) 300° C, (c) 600° C.

The morphology of the structure was determined by SEM and TEM. Figures 7.5 and

7.6 show the morphologies of Reference RW, Reference A and Reference B using the SEM and TEM. Before calcination and at 300°C it can be seen that the morphology is similar, small spherical particles.

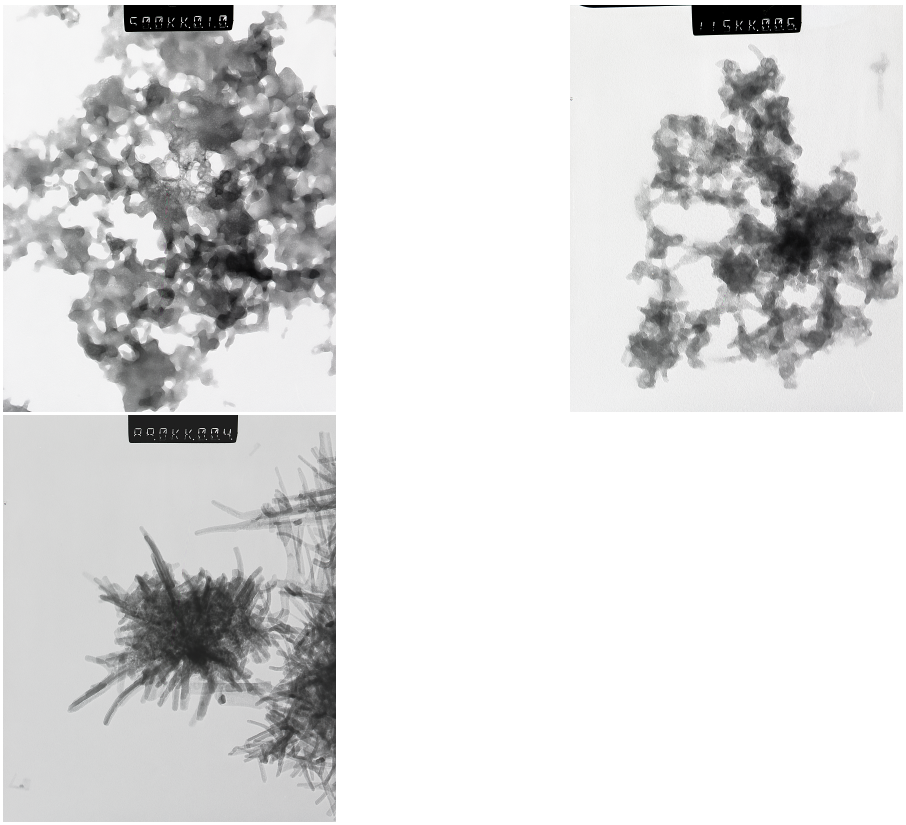

Figure 7.6: TEM images of AlF_3 nanopowder after heat treatment at 70° C (top left image), 300° C (top right image) and 600° C (bottom left image).

At temperatures up to 500°C the particles are still formed. It is only at 500°C and 600°C that the nanorods are present. It is at these temperatures that the material starts to crystallise and hence show their crystal form as nanorods. The crystallisation does not occur at lower temperatures which is shown in the XRD patterns described previously and seen in the particles that are formed. Above 600°C large particles are formed again as shown in Figure 7.7.

The nanorods can partly be attributed to the surfactant preventing agglomeration of material during the calcination step and helping form the rods upon cooling. At the higher temperatures the surfactant decomposes and no longer prevents sepa-

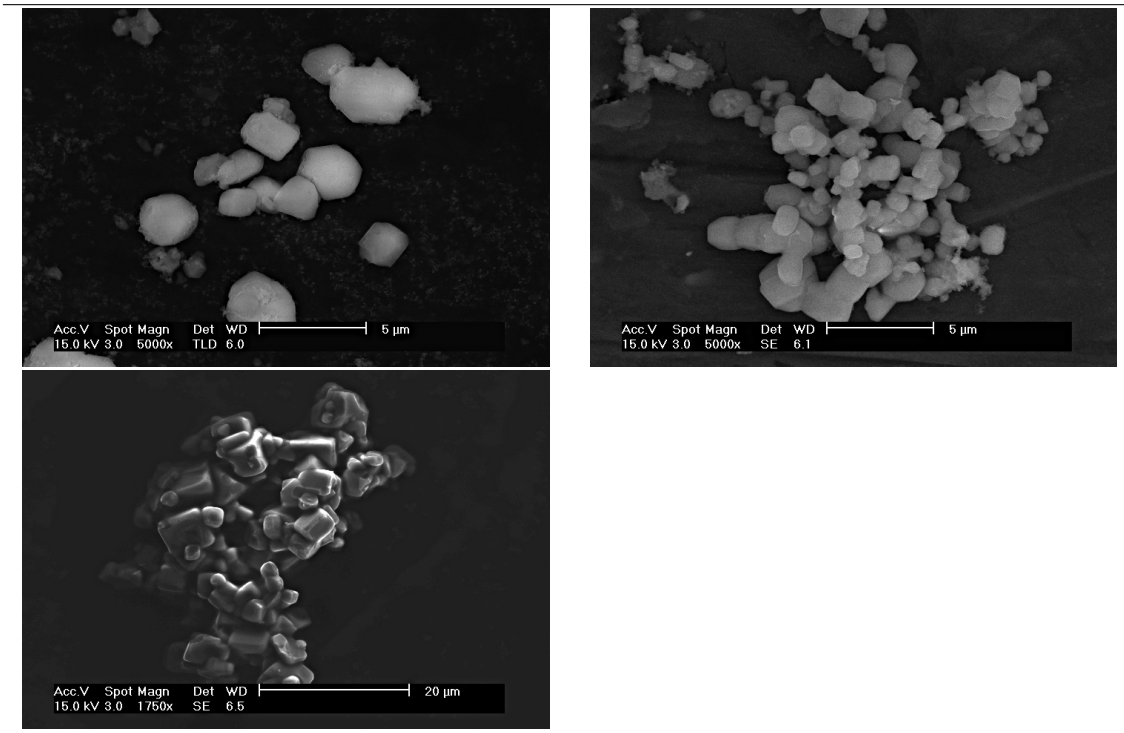

Figure 7.7: SEM images of synthesised AlF_3 at calcination temperatures of 700°C (top left image), 800°C (top right image) and 900°C (bottom left image).

rate crystal growth. Instead the crystals combine at an early stage and form large particles as shown in Figure 7.8.

The sizes of the rods vary depending on the calcination time. Figure 7.8 shows the rods from sample 12 and 13. A decrease in calcination time gives rise to shorter thicker nanorods where an increase in calcination time gives rise to thinner and longer rods. The molecular mass of polyethylene glycol and the mixing time did not seem to affect the size of the rods.

7.3.4 Surface Area

In order to improve on the performance of ball mill coated material the surface area of the samples would need to be analysed to see if there is an improvement. The increased surface area would allow a larger electrolyte electrode interface and reduce diffusion distances within the bulk of the material increasing the capacity of

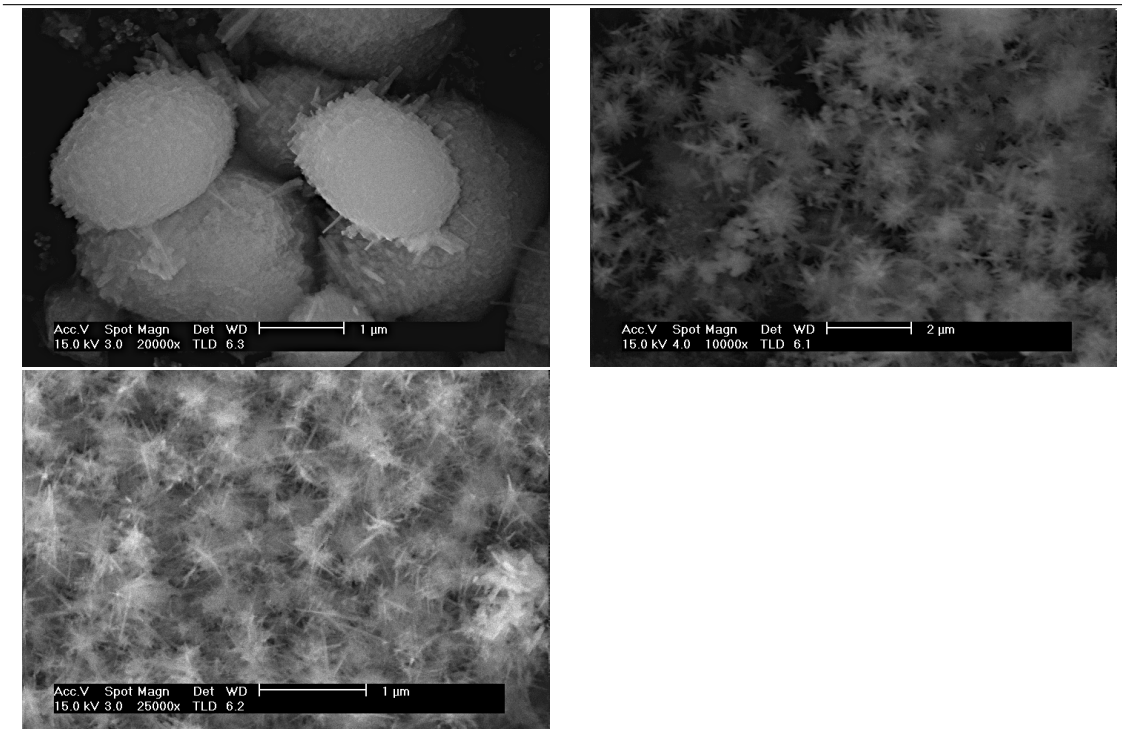

Figure 7.8: SEM image of AlF_3 nanopowder synthesised with no surfactant, sample 4 (top left image) and with calcination time varied, samples 12 (top right image) and 13 (bottom left image).

the material at higher current densities.

Table 7.2 shows the surface area of the synthesised samples. Only the samples that had the correct structure of aluminium fluoride were tested for surface area size.

Table 7.2: Specific surface area of synthesised samples.

Sample	Specific surface area (m^2/g)
CP	11.24
BMC	36.24
Reference B	68.76
1	52.30
3	102.00
4	25.43
5	76.96
6	61.82
7	55.37
8	65.91
9	13.66
12	68.91
13	56.97
14	41.17
15	69.64

Figure 7.9 shows a comparison of the variables and their specific surface area. As sample reference B was used as the standard to try and increase the surface area against, we can see from Figure 7.9 that by decreasing the mixing time and reducing the calcination time and even calcination temperature we can achieve similar or larger surface area particles and reduce the processing time and energy requirement. The great increase in surface area of sample 3 can be attributed to a larger amount of surfactant and it is the surfactant that we are actually measuring the surface area against not the active material aluminium fluoride. It is also seen that by reducing the amount of surfactant results in a large decrease in surface area. This can be attributed to no surfactant being in the reaction to stop the aluminium fluoride particles agglomerating when forming. By increasing the calcination temperature the surface area is also reduced due to the larger crystal structure of different phase AlF_3 being formed. The increased cooling rate can also be seen to reduce the surface area of the particles. As the particles are cooled quickly they do not have time to settle as they are cooling. This results in the formation of thicker shorter rod like particles which have a smaller surface area than thin long rods.

The other surface area values are pretty similar to the reference standard and vary by less than $10m^2$ so may be due to the particular sample area that was tested and not due to the mechanism of synthesis.

It can also be seen that the surface area of sample CP and BMC used in chapter 5 are much lower than of the synthesised nanorods. The results described in the next chapter will show whether this material is good for a cathode material for lithium batteries.

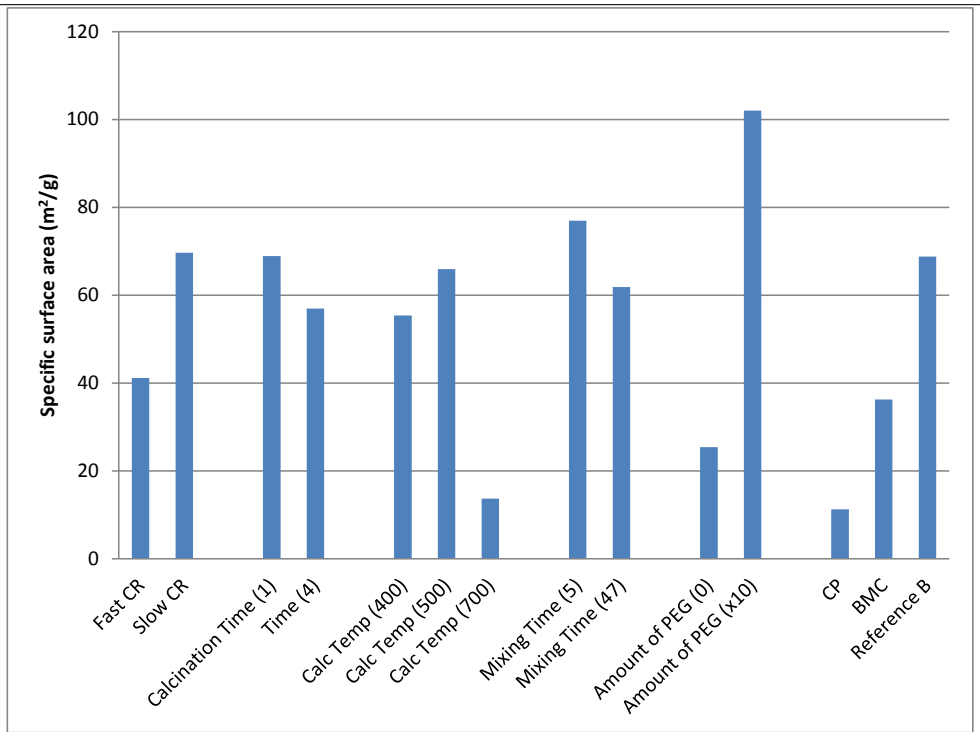

Figure 7.9: Graph to show comparisons of variables and their surface area.

7.4 Conclusion

AlF_3 nanofibers have been synthesised with two different space groups. The method used is novel in using aluminium nitrate and ammonium bifluoride. It is facile and produces a novel AlF_3 nanostructure. Depending on the space group and size of rods wanted the method can be optimised for efficiency. The resulting AlF_3 material exhibits a good phase and a high stability towards air shown in the lack of oxide groups in the FT-IR analysis, after being treated at high calcination temperatures under argon. It was found that the morphology and the phase of the synthesised powders changed depending on the calcination temperature and the calcination time. The next step is to try this synthesised material as a cathode material. Due to the increased surface area it may be possible to achieve higher capacities at higher current densities than the commercial powder and the ball mill coated powder.

Chapter 8

Aluminium Fluoride Nanorods as an Improved High Capacity Cathode for Lithium Batteries

8.1 Introduction

It has been shown that ball milled, ball milled coated aluminium fluoride and an AlF_3 nanocomposite can be used as a cathode material with a recorded capacity of over 950 mAh/g for the first discharge and a capacity retention of around 4% after ten cycles. Due to the poor kinetics attributed to the particle size and intrinsic insulating properties of aluminium fluoride the rate capability upon charging and the cycle life is not sufficient for rechargeable batteries. In order to to increase the kinetics of the material and hence contribute to an increased rate capability and cyclability the particle size of the aluminium fluoride may need to be reduced.

The newly synthesised aluminium fluoride nanorods described in chapter 7 are shown to have a higher surface area and smaller particle size than the previously tested ball milled particles. By using equation 2.16 the diffusion length has been reduced

so a decreased diffusion time would be expected. It is also expected that as the reduced particle size decreases the diffusion distances of the ions and electrons the material reduces resutling in an increased conductivity, which would manifest itself in a larger capacity at higher discharge rates.

8.2 Experimental

Sample Reference B was chosen as the active cathode material and to be coated. This was due to its good crystalline structure and morphology. It was coated in the same way as the ball milled samples; mixed with 5wt% PVDF and calcined at 600°C. The cells were created as stated in chapter 4. The bare nanorod sample will be further denoted NR and the coated nanorod sample is NR_c.

8.3 Results and Discussion

Figure 8.1 shows the SEM of the synthesised nanorods and the carbon coated nanorods. It can be seen that the morphology is different from the initial synthesised nanorods as they become mesh like spherical particles. These particles may form during the cooling period after calcination. A thin carbon precursor layer forms around the nanorods similar to the ball mill coating method, but as the nanorods are much smaller and more brittle when they are heated a substantial structural transformation occurs. As the nanorods contract together upon heating the PVDF acts to stop complete agglomeration of the AlF_3 but allows an interconnected nanorod sphere to be formed.

The higher electronic conductivities of the mesh like spheres and synthesised nanorods over the ball milled samples are shown in Table 8.1 and calculated from equations 4.4 and 4.5. The increased conductivity can be attributed to the conductive coating

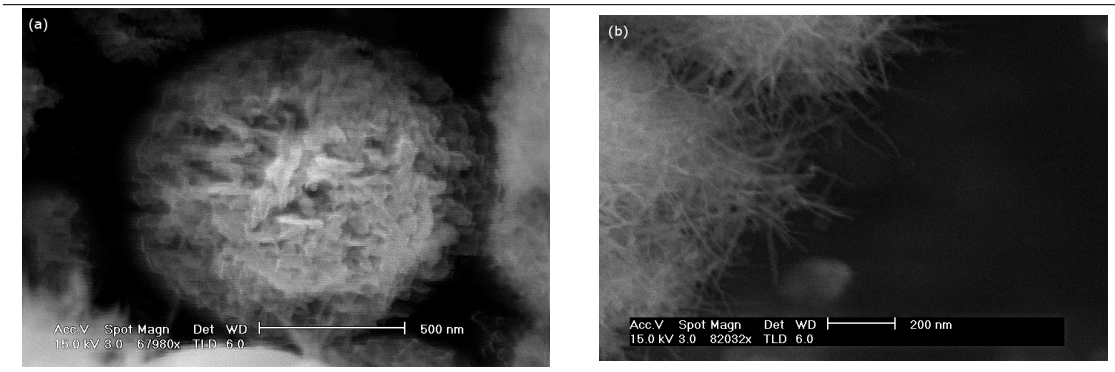

Figure 8.1: Morphology of the carbon coated nanorod sample NR_c (a) and Morphology of the bare nanorods (b)

of electrically conducting carbon and the morphology. The rods form a spherical object with nano size channels which can allow for easy electron conduction.

Figure 8.2 shows the XRD pattern of sample NR_c against the commercial bought AlF_3 pure powder. It can be seen that the phase is identical to the commercial powder and has the hexagonal lattice system with space group $P63/mmc$.

An important feature of powdered materials for use in electrodes for lithium batteries is their tap density. This is particularly important in materials for electric vehicles as a high tap density allows for a high volumetric energy density which is required for a large mileage in electric vehicles. The tap density for sample NR was recorded as 0.73g/cm^3 and 0.91g/cm^3 for NR_c. The NR_c sample has a higher tap density due to the hierarchial structure formed of the large secondary particle made up of smaller rods which allows better alignment when tapped than the NR sample. These values are still low compared with the micron sized CP sample of 1.34g/cm^3.

The first discharge curves and charge curves of the NR sample and the NR_c samples are shown in figure 8.3. It can be seen that the initial discharge curves produce

Table 8.1: Conductivities of samples NR and NR_c.

Sample	Resistance (Ω)	Area (m^2)	Length (m)	Resistivity (Ω m)	Conductivity (S/m)
NR	1.04×10^6	1.13×10^{-4}	7.5×10^{-4}	1.56×10^5	6.41×10^{-6}
NR_c	6.75×10^5	1.13×10^{-4}	7.5×10^{-4}	1.02×10^5	9.83×10^{-6}

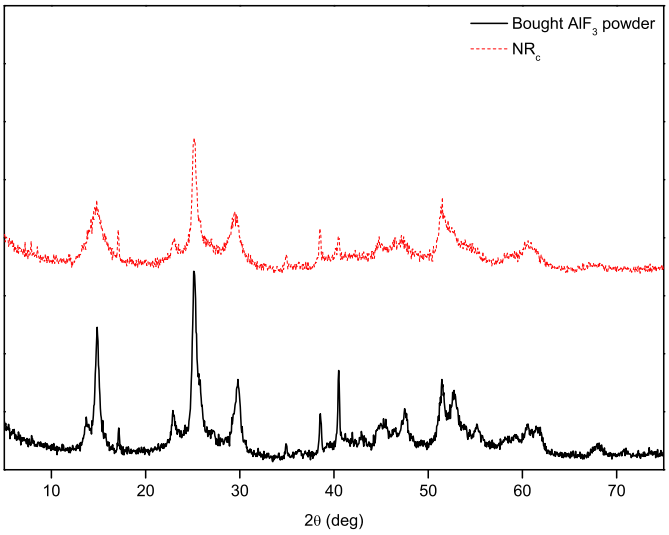

Figure 8.2: XRD pattern of sample NR_c

very high capacities for both samples at the slower rates of 0.1C and 0.125C, of 957mAh/g. The NW samples capacity then starts degrading substantially at further increasing discharge rates, until 0.5C where it has a capacity of 85mAh/g at an average of 1.1V. At the slower discharge rates it can be seen that the voltage is a one step profile at a useable voltage of between 1.8V and 2.4V, where the AlF_3 reactant and the Al and LiF products are all in a solid phase producing the flat discharge plateau. At these slow rates the kinetics of the electrode and morphology of the material allows the conversion of the material to take place without suffering huge polarisation loses. The internal resistance of the bulk phases within the cell are low and concentration overvoltage is small, there is no restriction in the current caused by concentration changes of the electrolyte species at the electrode surface.

At the rates of 0.25C and faster the voltage profile doesn't have a distinct one step plateau but decreases slowly until 1V suggesting the reactants and products are in both a liquid and solid phase resulting in a decreasing voltage curve. The NR_c samples have very high initial discharge capacities at a useable voltage between 1.5V and 2.6V even up until discharge rates as high as 0.33C. This is more than the NR samples and can be attributed to the added carbon coating, which in turns affects

the morphology of the sample. This morphology and added carbon increases the electronic conductivity which gives rise to the higher capacities at the faster discharge rates. As well as increasing the electronic conductivity the ionic conductivity is improved due to the network of nanopores allowing the electrolyte to impregnate the spheres and contact a larger area of the material than the NR sample. As described in the previous chapters the one stage plateau is attributed to the three electron reduction of AlF_3 to form Al and LiF. At the discharge rates above 0.33C the carbon coating no longer reduces the polarisation through the active material and mass transport through the electrode is reduced, reducing the capacity substantially, at a much lower voltage. At these higher discharge rates the polarisation is not only affected by surface and electrode kinetics but the kinetics through the remaining material itself; it is the intrinsic insulating properties that need to be improved in order to increase discharge capacities at the higher rates.

Upon discharging, the conversion reaction of AlF_3 into Al and LiF results in a structural change of the material. It can be seen from Figure 8.3 that the increased conductivity of the initial AlF_3 has a slight effect on the charge capacitates at the different charge rates. However, it does not have such an influence on being able to increase the charge rates further due to the structure changing from the primary morphology. The initial morphology increases the electron conductivity through the discharged electrode resulting in a lower polarisation allowing for a charge plateau of 3.6V, which is closer to the discharge plateau of 2.5V for the NR_c samples and a marked improvement of the voltage hysteresis observed in the NC and BM samples. The variance between the two plateaus can be attributed to the kinetics of the material as the difference between the two plateaus increases as the scan rate increases. As the scan rate increases the ohmic potential and concentration overvoltage increase, impeding electron and ionic diffusion, resulting in lower capacities seen at the faster charge rates and a continuously increasing charge profile, not the charge plateau seen at the lower charge rates.

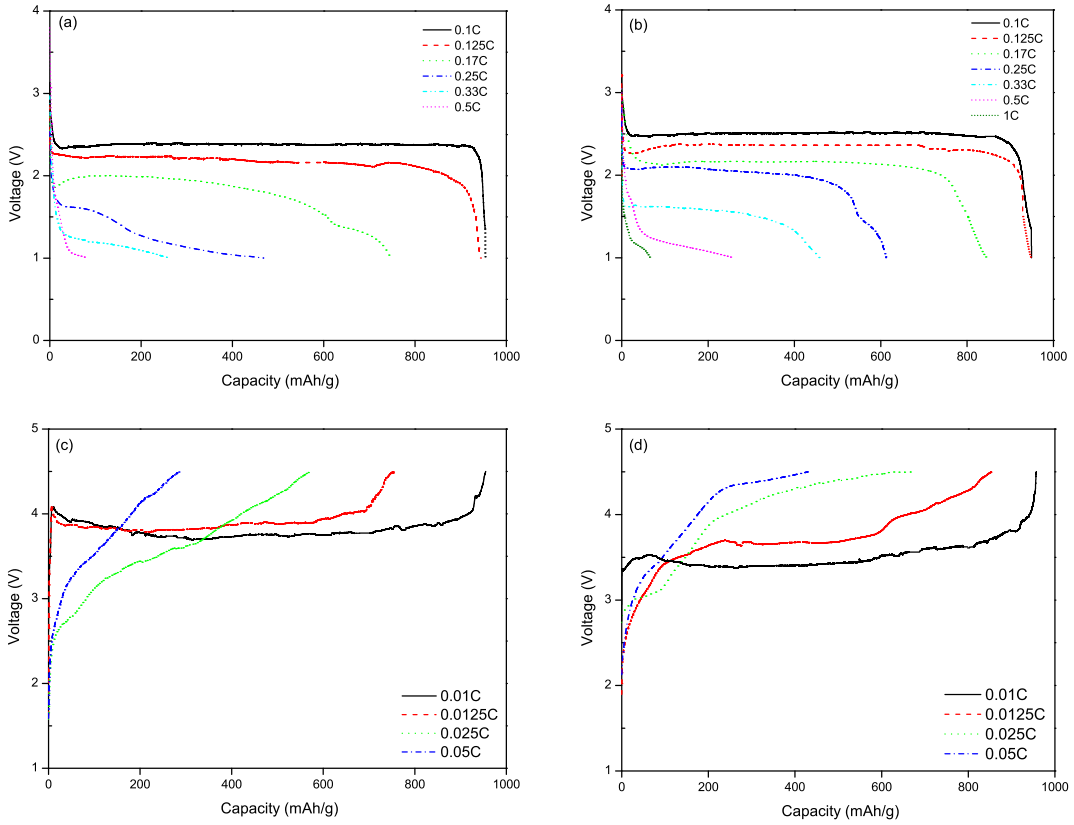

Figure 8.3: Discharge and charge curves for samples NR, (a) and (c), and NR_c (b) and (d).

Figure 8.4 shows how the increased conductivity of the NR_c sample during the discharge and charge process could happen. The morphology of the NR_c sample allows a tighter packing of particles than the nanorods of the NR sample. Upon discharge the material converts to Al and LiF leaving two distinct particles, the LiF being much smaller than the Al. In the NR sample where packing is not so tight there are larger distances between active material particles increasing the distance the electrons and ions have to travel to one another. In the NR_c sample there are lots of smaller groups of active material particles closer together decreasing the distance electrons and ions have to travel to each other, hence, increasing the conductivity compared to the NR sample. This manifests itself in a lower polarisation, a voltage plateau closer to the discharge plateau and a larger specific capacity.

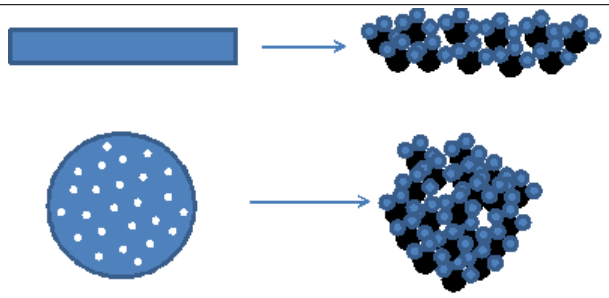

Figure 8.4: Schematic representation of conductivity mechanism for the NR and the NR_c samples. The bulk AlF_3 material is the large structure on the left. Upon discharge the particles stay vaguely in the surrounding vicinity taking the shape of the initial particle. The mesoporous sphere structure is tighter packed with other particles maintaining conductivity through the material. The nanorod stucture is less tightly packed resulting in a reduced conductivity. The LiF particles are the light spheres and the Al are the dark spheres. Not representative of particlesizes.

Figure 8.5 shows the dark field image of the two samples after one discharge at a 0.01C rate. One can see that the converted Al and LiF follows the shapes of the initial morphology and that in the NR sample there are larger spaces between them, than in the NRc sample.

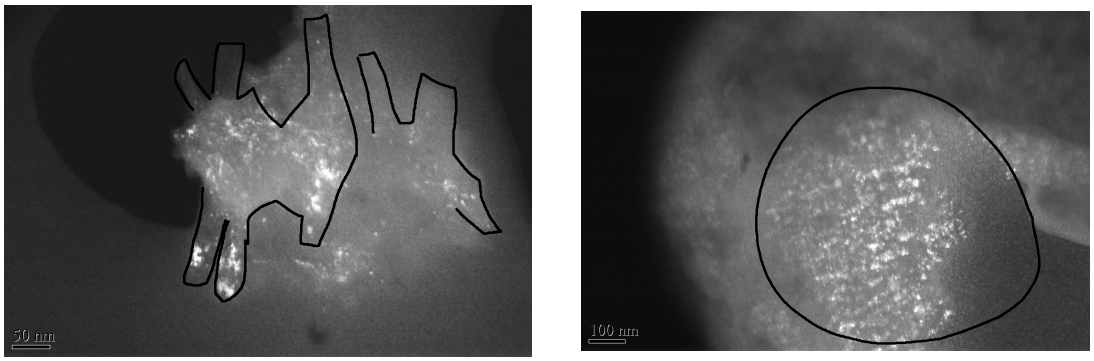

Figure 8.5: Dark field image of sample NR (a) and sample NR_c (b) the outlines are of the intital compounds morphology.

The energy densities for the two samples at specific discharge rates compared to current primary and secondary cathode materials are shown in Table 8.2. It can be seen at that the lower discharge rates the energy densities are substantially higher than those of the commercial materials. Even at the faster discharge rate of 0.25C for the sample NR AlF_3 is still competitive even at a lower useable voltage. For the NR_c sample the energy density is again substantially higher even at discharge

rates of 0.33C at a respectable voltage. However, at the faster discharge rates the intrinsic insulating properties of AlF_3 prevent a useful voltage plateau from being recorded even at the low capacities, resulting in an energy density much smaller than the commercial materials. The initial energy density is important for primary cells but for rechargeable cells it is important to have a high energy density over a number of cycles.

Table 8.2: Energy densities of samples NR and NR_c.

Sample	Discharge Rate	Discharge Capacity (mAh/g)	Discharge Voltage (V)	Specific Energy Density (Wh/Kg)
NR	0.1	957	2.4	2282
	0.125	949	2.2	2075
	0.17	746	1.8	1343
	0.25	469	1.5	704
	0.33	262	1.2	314
	0.5	82	1.1	90
NR_c	0.1	957	2.5	2383
	0.125	946	2.4	2270
	0.17	813	2.2	1789
	0.25	612	2.1	1285
	0.33	458	1.6	733
	0.5	259	1.2	311
	1	66	1.1	73
$LiFePO_4$ [120]	1	147	3.4	500
CF_x [121]	1	712	2.2	1566

Figure 8.6 shows the cycle life over 20 cycles of the two samples at a charge rate of 0.01C and a discharge rate of 0.05C. Both samples deliver initial specific discharge capacities of over 955mAh/g for the first cycle at a voltage of over 2.3V. However, as the cycles increase the capacity fades dramatically, from 803mAh/g in discharge three to 456mAh/g in discharge four and then to 167mAh/g, 17% of the initial capacity, in discharge ten for sample NR. The capacity fade after discharge ten is not as great as the first ten cycles as it decreases to 78mAh/g, less than 10% of initial capacity at discharge 20. As the conductivity of the sample increases, as in NR_c, the capacity increase over cycling is evident. However, there is still dramatic capacity fade over the first ten cycles. The third discharge capacity of sample NR_c is 830mAh/g dropping to 599mAh/g for discharge four and 367mAh/g for discharge

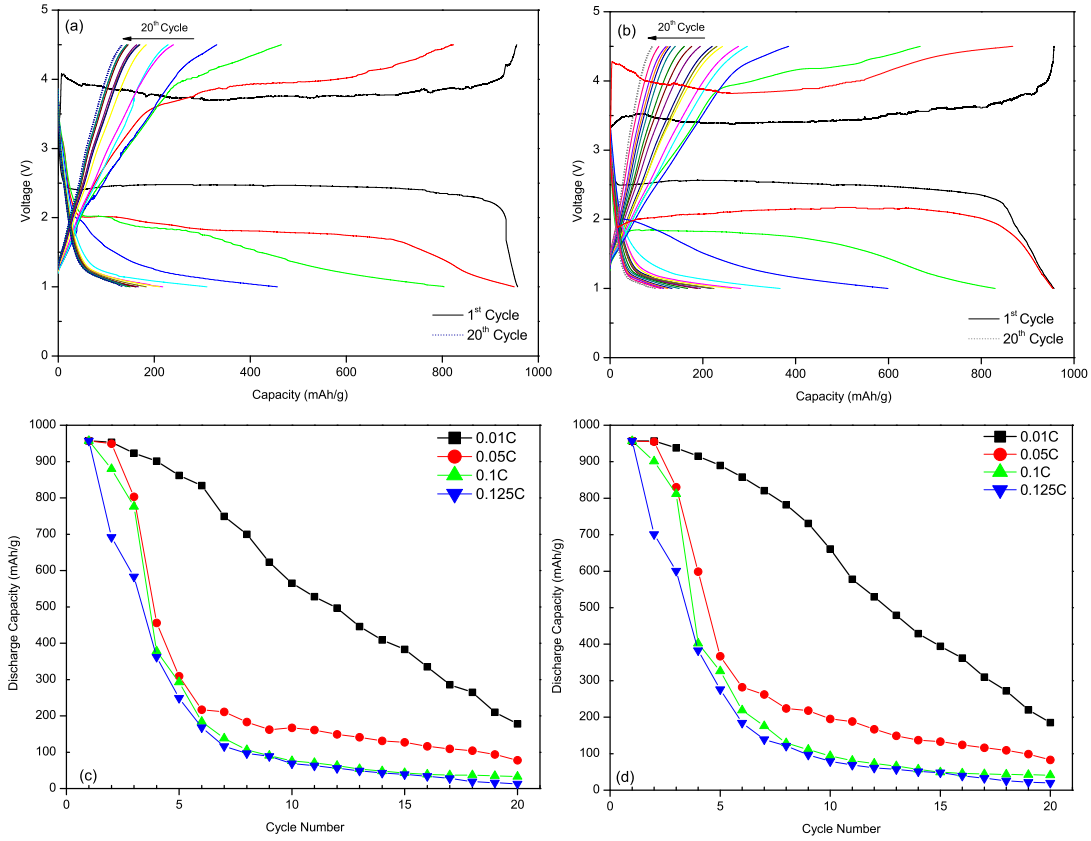

Figure 8.6: Cycling profile of samples NR (a) and NR_c (b) at a charge rate of 0.01C and a discharge rate of 0.05C. The cycling capacity for samples NR and NR_c at different discharge rates and a charge rate of 0.01C is shown in (c) and (d) respectively.

five. The capacity fades from 195mAh/g to 83mAh/g between discharges ten and 20, 20% and 9% of the initial discharge capacities. Increasing the conductivity is not the only factor when trying to increase the cycling stability.

The coulombic efficiency graphs, shown in Figure 8.7 do not follow a real trend but it can be seen that the majority of the charge discharge cycles have a higher coulombic efficiency than the samples tried previously, this is a result of the increased surface area improved material kinetics. The largest drop in coulombic efficiency cames in the first five cycles. After these cycles it stays roughly constant above 80% till the last charge. The largest percentage reduction in capacity is also seen in the first five cycles relating the coulombic efficiency with the initial structural changes in the first discharge and the formation of surface species on the AlF_3 and reductants LiF

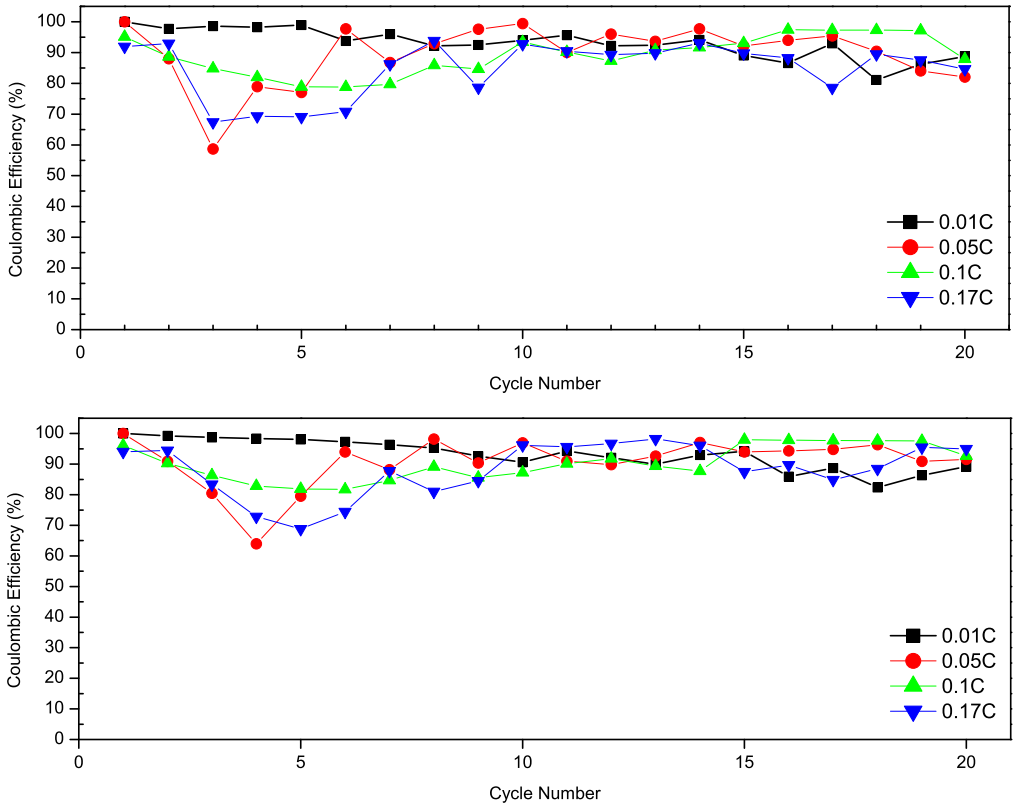

Figure 8.7: Coulombic efficiencies of NR and NR_c at different cycling rates.

and Al.

The energy densities of the two samples and a highly researched material in lithium iron phosphate, over a particular number of cycles are shown in Table 8.3.

Table 8.3: Energy densities of samples NR and NR_c at discharge cycles 1, 5, 10 and 20. The $LiFePO_4$ sample was cycled at a faster discharge rate of 1C

Sample	Cycle Number	Discharge Capacity (mAh/g)	Discharge Voltage (V)	Specific Energy Density (Wh/Kg)
NR	1	957	2.45	2345
	5	309	1.2	371
	10	167	1.1	184
	20	78	1.1	86
NR_c	1	957	2.5	2393
	5	367	1.2	440
	10	195	1.1	215
	20	83	1.1	91
$LiFePO_4$ [132]	80	125	3.5	438

It can be seen that the potential difference between the two discharge and charge

profiles is larger in the NR sample. This indicates that the NR_c sample has a smaller electrochemical polarisation and hence an improved conductivity over the NR sample. As the samples are cycled the potential difference between the discharge profiles becomes increasingly large and similar to each other suggesting the electrochemical polarisation increases as the cycles are increased. The capacity loss is due to a number of reasons; parasitic reactions within the electrolyte/active material interface, dissolution of particles within the electrolyte causing side reactions within electrolyte itself and continual structural change upon cycling degrades integrity of electrode. The results of chapter 7 indicate that the formation of Li_3AlF_6 is common place after repeated cycling and was seen to occur in a cell after twenty and ten cycles indicating that it occurs after only a few discharge charge profiles. Figure 8.8 shows the state of the electrodes before cycling and after 20 cycles. It can be seen that repeated cycling degrades the electrode and causes it to crack. The continuous structural change slowly loosens the surrounding material and causes the electrode to crack. Even though the structural change is not as large as the previous samples, as particle sizes go from around 50nm to 5nm, it seems to be enough to cause electrode cracking. The electrode cracking results in particles detaching from the bulk electrode and dissolute in the electrolyte which reduces the amount of active material there is to contribute to the specific capacity and contributes to the increased impedance resulting in the shallower charge discharge profiles.

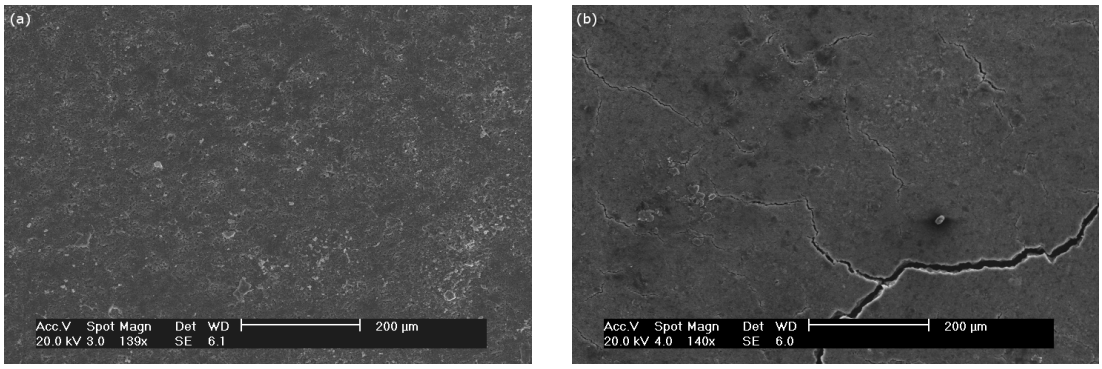

Figure 8.8: SEM images of the NR_c sample electrode before (a) and after (b) cycling

The impedance of the samples before first discharge, after first discharge, after first

charge and after 20 cycles is shown in the Nyqvist plots in Figure 8.9. The resistance between the electrolyte and electrode is modeled as R_s and is where the Z' axis is intercepted at the high frequency region. It can be seen that the resistance R_s is small throughout and similar for both samples due to the same electrolyte and cell fabrication method. It is much smaller than the charge transfer resistance and is around 6Ω. The charge transfer resistance modeled as R_{ct} is the medium frequency region and is determined by the radius of the semi circle. This impedance data for R_s and R_{ct} is shown in Table 8.4. It can be seen that as the cells charge the transfer resistance increases as it is cycled. This increase in resistance causes a larger polarisation and hence a limited capacity retention and poor cycling behaviour.

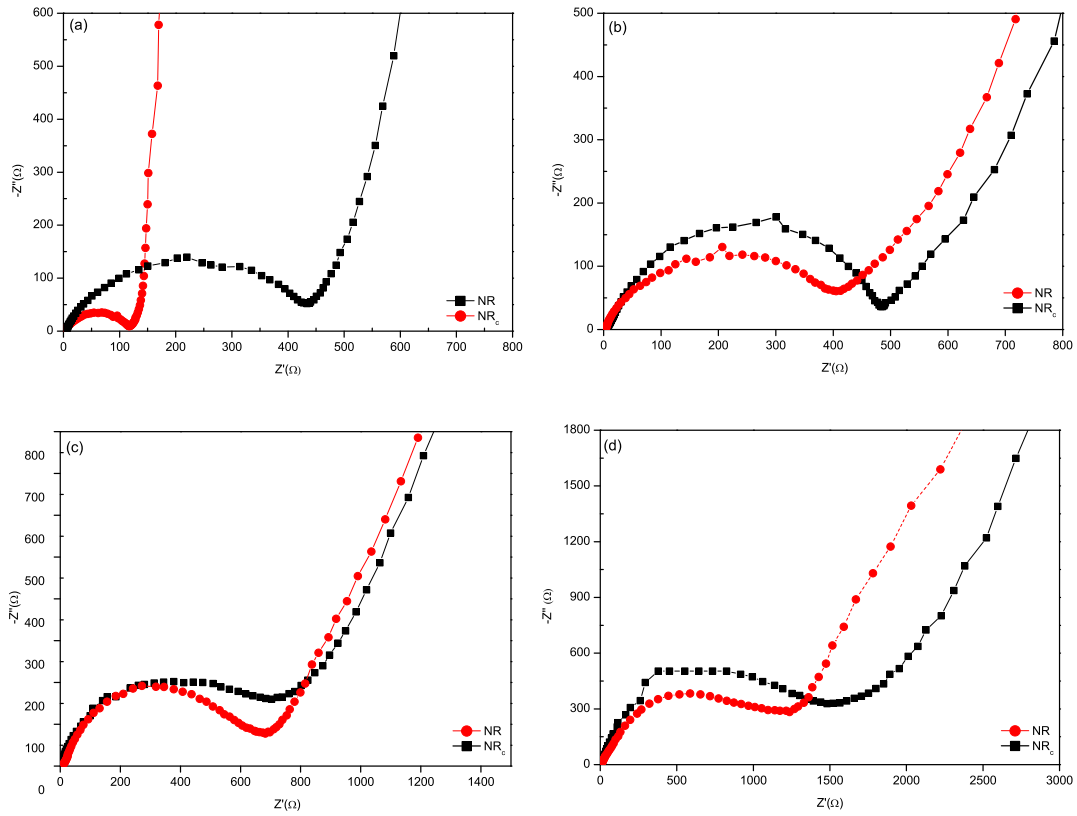

Figure 8.9: The Nqvist plots before 1st discharge (a) after 1st discharge (b) after 1st charge (c) and after 20 cycles.

By using the calculated charge transfer resistance in Table 8.4 the exchange current density can be calculated by equation 2.12 and is shown in Table 8.5. The exchange

current density can be seen to decrease as the cycle life increases by a factor of ten for the NR_c sample indicating that there is reduced electron diffusion through the electrode and electrolyte due to the reasons mentioned earlier.

The warburg impedance plots can be used to indicate the diffusion of the lithium ions and can be used with Figure 8.11 to calculate the Li^+ diffusion coefficients for the fresh cells and the cells cycled twenty times. Table 8.6 shows the diffusion coefficients for the NR_c sample. Only a NR_c sample was tested because the results were very similar to the NR sample in terms of initial discharge capacity and final discharge capacity as well as material kinetics.

The titration curve in Figure 8.11 shows that the total ohmic drop from this titration curve during the discharge profile for a NR_c cell under similar load is around 0.3V, smaller than the other tested samples, indicating that the improved kinetics reduces ohmic drop.

Figure 8.12 shows the cyclic voltammetry curves for NR_c. There is a clear peak between 2.5V–1V which is consistent with the discharge profiles in the previous figures. During the charge process there is also a sharp rise in current indicating an

Table 8.4: R_s and R_{ct} values of samples NR and NR_c from Figure 8.9.

	R_s (Ω)				R_{ct} (Ω)			
Sample	(a)	(b)	(c)	(d)	(a)	(b)	(c)	(d)
NR	6.251	7.076	7.451	12.14	219.25	239.3	361.15	805
NR_c	4.072	4.460	4.932	10.34	61.1	206.45	346.0	630.5

Table 8.5: Exchange current densities for samples NR and NR_c.

	i_o ($\times 10^{-5}$ A/cm^2)			
Sample	Fresh Cell	After first discharge	After first charge	20 cycles
NR	11.1	10.2	6.78	3.04
NR_c	40.1	11.9	7.08	3.89

Table 8.6: Lithium diffusion coefficients for samples NR_c.

	D_{Li} ($\times 10^{-15}$ cm^2/s)	
Sample	Fresh Cell	20 Cycles
NR_c	5.48	0.36

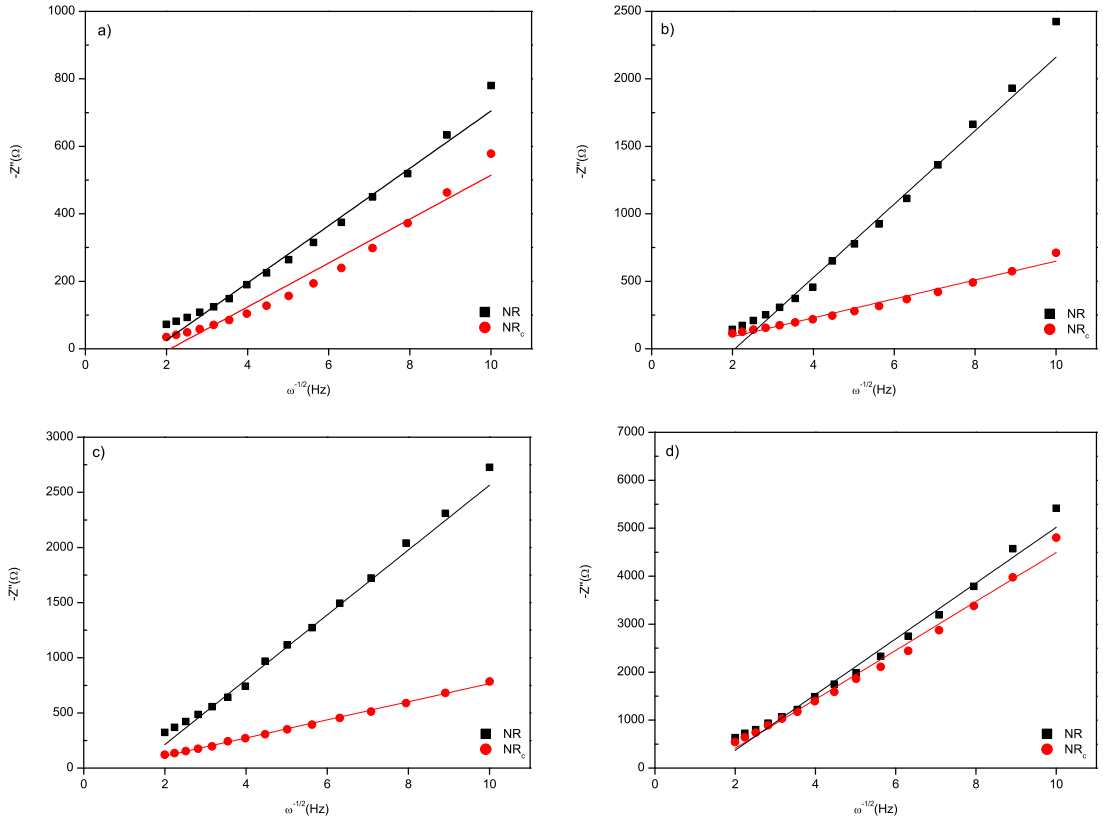

Figure 8.10: Warburg plots for samples NR and NR_c

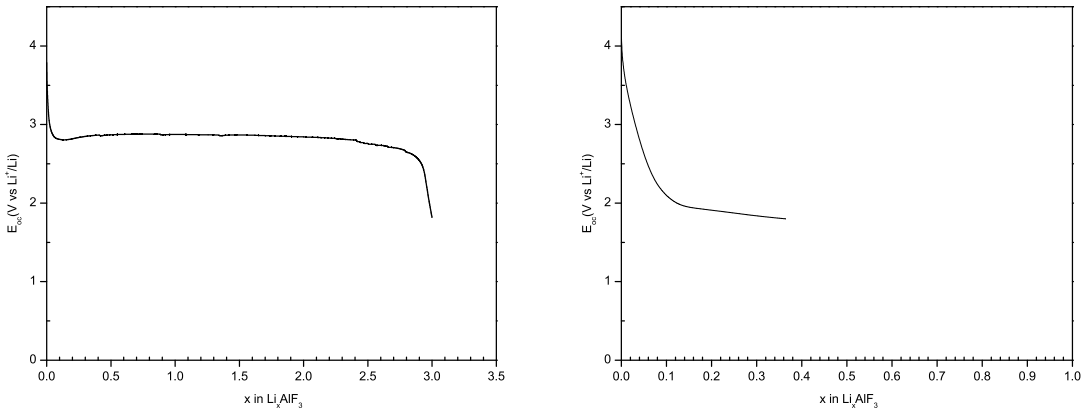

Figure 8.11: The galvanostatic titration curves for sample NR_c as a fresh cell and after 20 cycles.

oxidation process and charging is happening. After the sample is cycled it can be seen that the reduction and oxidation peaks decrease as the polarisation through the material increases and a much smaller reversible capacity is observed.

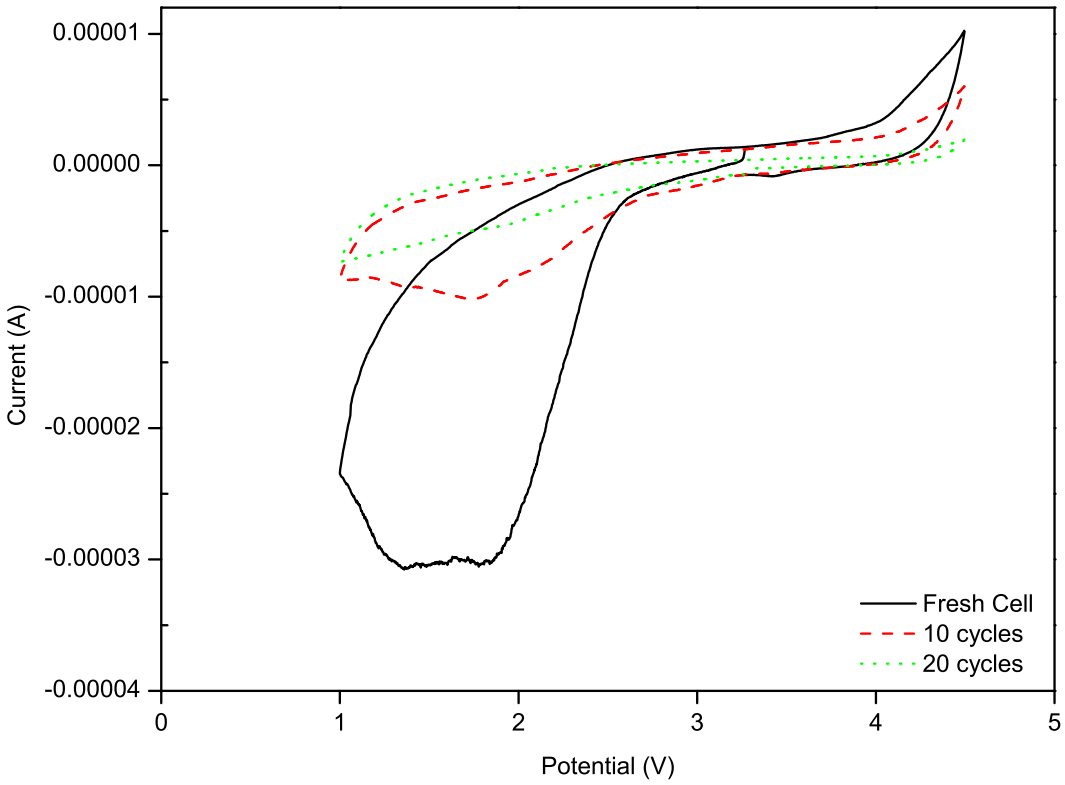

Figure 8.12: The CV curve of sample NR_c.

The chemical diffusion coefficient of the Li ion in AlF_3 can be found using the Randles-Sevcik equation 4.9 and is shown in Table 8.7. The diffusion coefficients start at 3.182×10^{-14} cm^2/s for the fresh cells during reduction to 1.240×10^{-15} cm^2/s for the twentieth CV cycle, showing how the diffusion coefficient during a number of reduction cycles rapidly fades. During oxidation the diffusion coefficient is even smaller and fades to 0.09×10^{-21} cm^2/s from an initial 2.249×10^{-21} cm^2/s. The recorded discharge capacities at relatively fast discharge rates compared to the charge rates is partly due to the increased lithium ion diffusion coefficient during reduction over the oxidation process.

Table 8.7: Anodic and cathodic diffusion coefficients for fresh, after five cycles and after ten CV cycles, for sample NR_c.

	Anodic D_{Li} ($\times 10^{-21} cm^2/s$)			Cathodic D_{Li} ($\times 10^{-14} cm^2/s$)		
Sample	Fresh cell	Ten cycles	Twenty cycles	Fresh cell	Ten cycles	Twenty cycles
NR_c	2.249	1.265	0.090	3.182	0.202	0.124

8.4 Conclusion

The synthesised nanorods from chapter 7 were used as the cathode material in lithium cells to see if the capacity at higher rates and cyclability could be improved due to the decreased size. The cells were tested and found to achieve a theoretical capacity at discharge rates of 0.125C. Useful capacities of over 200mAh/g were recorded at discharge rates of 0.33C for the NR sample and 0.5C for the NR_c sample, however this was at a voltage of around 1.5V average. It was found that the decreased particle size increased the conductivity of the powder and the cycle life was increased to 20 cycles. After ten cycles a capacity of over 550mAh/g was recorded for both samples at a discharge rate of 0.01C. The different morphology was also found to hold its shape when the initial metal fluoride compound was reduced however this did not stop the electrode from cracking and the capacity fading. The next step would look at trying to increase the integrity of the electrode to increase capacity and to try and find alternative electrolytes.

Chapter 9

Discussion

9.1 Introduction

The previous chapters show that aluminium fluoride can be used as a cathode material for lithium batteries and provides a basis to understanding the mechanism during cycling. It also describes a new synthesis procedure to synthesise nanorods and tests them as the active material in a lithium cell. This chapter will discuss the core of the work and discuss how the thesis could be taken forward.

9.2 Discussion

The initial results of the thesis show that aluminium fluoride can be used as a cathode material, for primary lithium batteries or potentially secondary lithium batteries. The mechanism involved in the reduction of AlF_3 during the discharge process is due to a three electron reduction to form LiF and Al, as confirmed by SAED and ex situ XRD. This nanocomposite was then shown to oxidise to reform AlF_3, however this was not very efficient in the initial samples that had low conductivity. When the

conductivities were improved the initial discharge rate was increased substantially while still achieving relatively high specific capacities although the voltage was not high. It was the reduction in particle size and the adding of either a carbon coating or carbon nanocomposite that produced theoretical capacities. However, these theoretical capacities were limited to discharge rates slower than 0.1C. By increasing the conductivity further, by reducing the particle size and introducing carbon the theoretical capacity was recorded at discharge rates of 0.125C. These samples also produced specific energy densities of over 700Wh/kg at discharge rates as high as 0.33C. It may be possible to further increase the discharge rate specific energy density by either improving the electrode / current collector interacting surface area and or by doping with metal ions. It was found that doping FeF_3 with Cobalt dramatically increased the discharge rate specific capacities and the cycle life [133].

For the samples tested in this work the specific capacity decreased rapidly over cycle life. The oxidation of LiF and Al to form AlF_3 was shown to happen but was not efficient enough in the uncoated samples to produce capacities close to theoretical after the first charge. By improving the conductivity it was found that the impedance of the cell during the LiF and Al phase decreased. This improvement increased the initial charge capacity but not by enough that produced near theoretical capacities on the second discharge. However, it was found by synthesising nanorods that had a much improved surface area the second charge discharge capacities were close to theoretical. This can be attributed to the increased surface area and decreased diffusion distances. As this was the only variables that were changed from the initial samples. The increased surface area allows the formation of LiF and Al to occur in a more dispersed area where the electrons and ions are free to manoeuver to, whereas in the lower surface area samples there is an aggregation of LiF and Al. The LiF and Al at the bottom of the aggregation is surrounded by more LiF and Al which oxidises slowly hindering the utilisation of all the available material reducing the charge capacity. However, over a number of cycles due to cracking of the electrode

and material dissolution into the electrolyte this capacity also fades. This dissolution can be hindered slightly by the coating of carbon as it prevents direct electrolyte contact but due to the change of structure from tetragonal AlF_3 to cubic LiF and Al the carbon coating breaks down and fails to protect the active material. It was thought the nanocomposite would improve cycle life, however, though the cycle life was improved slightly it was not improved significantly enough to suggest that it was a solution. It was thought that the carbon nanocomposite could also act like a barrier to the interface between active material and electrolyte and stop dissolution. It could not be confirmed that it did due to the cycle life still falling rapidly but that could have been due to the cracking of the electrode rather than the nanocomposite not shielding the material from the electrolyte. It would need to be tested with an electrode that does not crack, to see what the effect of the carbon nanocomposite has on cycle life with a $LiPF_6$ electrolyte. For the ex situ XRD samples it was found that after repeated cycling there was a formation of Li_3AlF_6 with the LiF, Al and AlF_3. This was found to be formed by the reaction of AlF_3 and LiF. It was hindered by the carbon coating but was still present after repeated cycling. It was not found on the initial discharge or on the initial charge but found after a number of cycles. This suggests that the LiF reacted over time to AlF_3 that had already undergone oxidation. The LiF instead of oxidising with Al would oxidise with the AlF_3 to form Li_3AlF_6. There was no presence of any other impurities during cycling that would indicate the formation of an SEI layer. If one was formed it was detrimental to the working of the cell due to the rapid capacity fade. However, this could have been due to other issues not just the formation of an SEI layer.

The initial one stage flat plateau seen at the lower discharge densities was due to the one step reduction of Al^{3+} to Al^0. However the discharge profile turned to having a sloping profile at increased cycle life and increased discharge currents. The sloping profile recorded at increased cycle number was due partly to the formation of Li_3AlF_6 that is a known solid liquid solution and partly concentration polarisation. At the

increased discharge rate the sloping profile can be associated with concentration polarisation.

The voltage recorded for the one stage plateaus was between 2V and 2.45V depending on the conductivity of the sample. This is not the voltage predicted by the redox potential table but is quite consistent with the thermodynamic calculation of 2.89V. The deviation from this value is due to the intrinsic poor kinetics of the material and ohmic drop, by increasing the conductivity the ohmic drop reduces and the voltage increases. It is interesting to note that the thermodynamic calculations of the potential when considering aqueous aluminium is 1.23V (Al(aq) has a gibbs free energy of -481.2kJ). This could be a reason why the voltage profile drops to around 1.3V after a number of cycles and has a profile associated to a solid liquid solution. However, more experimental analysis would be needed to confirm this.

Another issue with the cycle life and charging was voltage hysteresis found upon charging. The high charge voltage required for the samples was reduced as the conductivity increased as in samples NR and NR_c but was still much higher than the discharge voltage and over the cycle life only increased further. This could be attributed to the increased polarisation through the cell as the cycle life increased as it was possible to record near theoretical capacities over a few discharges. The polarisation was a combination of increased charge transfer resistance through the electrode due to the reduced conductivity of the pathways formed during the conversion reactions and an decrease in the rate of lithium diffusion. The decrease in the lithium diffusion rate was thought to be down to the inherent poor kinetics of the aluminium fluoride which also resulted in an increased charge transfer resistance.

The CV curves of the BM, NC and NR_c samples all showed distinct peaks which can be associated to the reduction and oxidation processes. The higher the conductivity of the sample the higher the diffusion coefficient of the lithium ions were through the electrode. This resulted in more defined peaks at the recorded poten-

tials. This increase in diffusion manifested itself in the higher energy densities that were recorded for the particular samples. The samples with the smaller particle sizes were found to have increased diffusion coefficients due to the small diffusion lengths. Sample NR_c had the highest diffusion coefficient due to the diffusion lengths being shorter than 50nm in one particular axis. It can also be seen that the cathodic peak is much larger than the anodic peak indicating that the diffusion coefficient, as calculated, is much smaller during the oxidisation process. This is also confirmed with the impedance spectra. This indicates that there is a development during oxidisation which inhibits the diffusion of lithium ions. This could be the formation of Li_3AlF_6 which is unlikely at the first cycle, the formation of a surface layer on the LiF and Al which hinders oxidisation or the reduction of diffusion pathways due to the structural changes during the conversion reaction. It is the improvement at this LiF and Al stage which could result in improved cycle life.

The synthesised particles were found to be quick and easy to fabricate and were of good phase as shown by the XRD spectra. Above 700°C the structure changed from a hexagonal to a rhombohedral lattice system and had a reduced surface area. The surface area of the synthesised particles varied with the amount of surfactant used as it stopped the agglomeration of particles. The higher the percentage of surfactant used the higher the surface area and smaller the nanorods. Whilst the synthesised particles had a higher surface area and conductivity due to the small size they had a smaller or similar tap densities of 0.73 (NR) and 0.91 (NR_c) g/cm^3 than samples CP, BM, BM_c and NC which had 1.34, 1.12, 1.06 and 0.89 g/cm^3 respectively. A specific energy density for sample NR_c of 2345Wh/kg would require a volume of 1370 cm^3 whereas a volume of only 893 cm^3 would be required for sample BM and a specific energy density of 2058Wh/kg; the resulting Wh/L would be 1711 and 2305 respectively. This shows that even though the Wh/kg of the NR sample is higher than the BM sample due to the tap density the actual volumetric energy density is larger for the BM sample, meaning that it would be more beneficial to use the BM

sample in electric vehicle batteries due to the less space the cathode material would need in the cell itself.

These results indicate that even if the problems are insurmountable in terms of developing a rechargeable battery, the material can still be used very effectively as a cathode material in a primary battery, with a very high energy density. With a few improvements the material may also be able to have a high power density.

There are a number of issues found at the initial investigation stages of this material but with specific energy densities over 2250 Wh/kg at a voltage of around 2.4V, with a clearly rechargeable mechanism and a low material cost, every effort should be made to investigate more fully the problems that arose in this research thesis.

9.3 Future Work

It is clear that AlF_3 can be used as a cathode material for primary batteries and with further research could potentially be a cathode material in rechargeable batteries. However, in order to be used in rechargeable batteries the cycling life will need to be improved.

The routes that were not taken in the development of this project would be ideal places to start investigating to improve the cycle life of this material. It involved further investigation of the mechanism after repeated cycling. Focusing on understanding the liquid and solid solution phase of the reactants and products to understand why they appear and under what conditions. The formation of a potential SEI layer and the reaction of the reductants and oxidants with particular electrolytes would be a large undertaking and produce some valuable results. This would work closely with trying to optimise the electrolyte as it seems that there are adverse reactions taking place and or the SEI layer is inhibiting lithium ion and

diffusion and electron conductivity while reducing the amount of active material that is present to be reduced or oxidised.

With a thorough investigation of the electrolyte, SEI layer and discharge and charge mechanism a ternary phase diagram could be produced to understand the different compositions and phases throughout the reaction.

Future work would also concentrate on trying to fabricate an electrode or particles that can withstand the volume changes through repeated cycling either while still maintaining good electrical conductivity with the current collector and the conductive matrix it is imbedded in. To further increase the rate capability the doping of the synthesised aluminium fluoride should be tried. This has the potential to improve conductivity and if particular dopants are used there may be the possibility that the cycle life is increased. The dopants may not react during discharge or charge keeping a shell structure that the reductants and oxidants can form around.

Due to the predisposition of consumers and their perception of the safety of lithium there would be a need to use this material with a non lithium metal anode. This would then require research into a lithiated carbon or silicon anode (two out a possible many anodes) that could be used with high surface area highly conductive aluminium fluoride. The anode would need to be chosen to maximise the voltage of the cell. Another way is to fabricate a LiF and Al nanocomposite which could act as the lithiated cathode for the use with a non lithiated non metal anode. This would require improving the conductivity and reducing the surface area of LiF and Al nanoparticles while creating a composite which is highly conductive, able to expand to accommodate volume changes and oxidises easily with the removal of electrons, but only with each other.

Chapter 10

Conclusion

This chapter will discuss the conclusions that have been drawn from the work carried out.

10.1 Conclusions

The initial aim of this thesis was to develop a material that has a higher energy density than current commercialised cathode materials, with the potential of having a high power density and long cycle life. The cathode material that was developed was chosen to be aluminium fluoride. This was because of its high theoretical capacity and low material cost. The long term vision of a material developed in this thesis was to be used in electric vehicles. In that case the idea was to look for a material that was low cost and could potentially have a large energy density, this could bring down the cost in electric vehicles batteries from $500 per kWh which is the USABC medium term goal [134]. In order to do this the material needs to be cheap and have a high energy density.

Aluminum fluoride was thought to have a discharge voltage between 1.39V and

2.89V. Initial results show that the first discharge plateau from ball milled samples is around 2.15V. This results in a specific energy density greater than 2000 Wh/kg, which is substantially larger than many commercial materials. It was shown that this initial voltage profile was improved even further to 2.45V by using a nanocomposite and by using coated nanorods. This brought the energy density to values over 2300Wh/kg which is considerably higher than $LiCoO_2$ (555 Wh/kg) and even Li/CF_x (2143 Wh/kg) primary cells [121]. This if could be maintained over a number of cycles would be an excellent candidate for a future rechargeable battery. The initial tests determined the rate capability during discharge and found that 0.1C was the maximum where theoretical capacity could be reached for commercially bought materials. These materials had to be ball milled. Ball milling was shown to increase the conductivity of the powder enough to produce a theoretical discharge capacity at 0.1C, however, increasing the discharge capacity led to capacities less than 55% of theoretical. However, by increasing the conductivity even further by introducing a small coating or by forming a carbon nanocomposite nearly 80% capacity could be achieved at a faster discharge rate of 0.125C. The conductivity of the sample had a bearing on the cycling capacity as it was shown that the more conductive samples had larger capacities for longer cycles, however there was still rapid capacity fade. The capacity fade was initially negated by using the nanocomposite as over 50% capacities were being cycled for the first few cycles, however this soon ended up being less than 4% after ten cycles. This intial capacity fade was thought to be down to cracking of the electrode. The cracking of the electrode would break the electrical conduction network created by the carbon and increase impedance through the cell. This impedance would result in a polarisation through the cell and reduce the capacity, as well as some electrode material breaking from the main bulk electrode becoming redundant in the oxidation or reduction process. It was also found that the formation of Li_3AlF_6 was also partly responsible for capacity fade as LiF would react with AlF_3 reducing the amount of active material left to oxidise or reduce.

During analysis of the reduction and oxidation process it was confirmed that the one stage profile was due to a three electron reduction of aluminium fluoride to lithium fluoride and aluminium which resulted in the recorded theoretical capacity. However, it was observed that upon recharging the cell not all the LiF and Al oxidised to reform AlF_3, which was a result of the reduced capacity after the initial charge. This oxidation process occurred at a voltage much higher than the discharge profile which was partly due to an increased impedance through the cell. This increased impedance could have been caused by the large surface/interfacial region of the ionic bonding LiF and metallic bonding Al. This region would require a large energy to overcome and start the oxidation process. This resulted in the high charge voltage profile. By further increasing the cut off voltage the capacity could have been increased but another electrolyte would have to be utilised as 4.5V borders on the oxidisation potential of $LiPF_6$. By further increasing the conductivity of the aluminium fluoride it was thought that cycling capacity could be extended as well as the rate capability.

The aluminium fluoride nanorods that were synthesised were dependant on the calcination temperature. It was found that aluminium fluoride was always formed if calcined under an inert atmosphere such as Argon. However, the calcination temperature dictated what structure was formed. At temperatures below 600°C a hexagonal lattice system was formed where as above 600°C a rhombohedral lattice system was formed. It was also found that the calcination time also affected the morphology of the rods. Shorter fatter rods were synthesised at longer calcination times than shorter calcination times, these longer shorter rods also had higher surface areas.

These nanorods were then tested in lithium cells to see if they improved performance. The nanorods were tested coated and uncoated. The coated samples produced what looked like a mesoporous spheres made up of the agglomeration of lots of nanorods.

The conductivity of the powders were initially much higher than that of the ball milled samples. This was attributed to the reduced diffusion distances. Initial discharge results produced specific capacities of over 800 mAh/g for discharge rates of 0.17C for the coated sample and 715 mAh/g for the uncoated sample, a huge rise in capacity at those current densities over the ball milled samples. This was believed to be due to the improved conductivity. The charge rates were also able to be increased substantially indicating that there was a benefit to the initial morphologies after the first discharge. It was also shown that the difference in potentials during discharge and charge was much less than the previously tested samples. This was a contribution to the increased capacities recorded on the second discharge. The recorded impedance was also much less than the previous samples after the first discharge, indicating that the products of the reduction process did not degrade the electrode as much. This resulted in near theoretical capacities on the second discharge. However the high capacities did not last long and after 20 cycles this was reduced to less 10% of theoretical. The impedance of the cell increased as the cycle number increased indicating an increased polarisation caused by the charge transfer resistance increasing and the diffusion coefficient decreasing. The cracking of the electrode was one reason this happened.

The initial aim was met with the recording of very high initial capacities for aluminium fluoride as a cathode material. The objectives were met, however, the rapid capacity fade is a subject that needs to be investigated further to make this electrode material useable for applications which require long cycle life. The material is rechargeable albeit over a few cycles, but with future investigation the material could become one for future portable electronic devices or electric vehicles.

References

[1] K. Dumaisnil. Internship Report, 2010.

[2] Micheal. M. Thackeray. *Encyclopedia of Energy.* Elsevier Inc, 2004.

[3] K. Xu. Nonaqueous Liquid Electrolytes for Lithium-Based Rechargeable Batteries. *Chemical Reviews*, 104:4303 – 4417, 2004.

[4] http://inventors.about.com/library/inventors/blbattery1.htm. Battery Power.

[5] J. M. Tarascon and M. Armand. Issues and challenges facing rechargeable lithium batteries. *Nature*, 414:359 – 367, 2001.

[6] J. B. Goodenough and Y. Kim. Challenges for Rechargeable Li Batteries. *Chemistry of Materials*, 22:587 – 603, 2009.

[7] A. Manthiram. Materials Challenges and Oppurtunities of Lithium Ion Batteries. *The Journal of Physical Chemistry Letters*, 2:176 – 184, 2011.

[8] J.-M. Tarascon. et al. New concepts for the search of better electrode materials for rechargeable lithium batteries. *C. R. Chemie*, 8:9 – 15, 2005.

[9] chem.skku.ac.kr. Structure of $LiCoO_2$. 2010.

[10] C. A. Vincent and B. Scrosati. *Modern Batteries: An introduction to electrochemical power sources.* Wiley and Sons, 1997.

[11] Multiple. *Advances in Lithium-Ion Batteries*. Kluwer Academic / Plenum, 2002.

[12] M. Park. et al. A review of conduction phenomena in Li-ion batteries. *Journal of Power Sources*, 195:7904 – 7929, 2010.

[13] Multiple. *Lithium Batteries*. Kluwer Academic, 2004.

[14] Ionic Crystals. Spinel Structure. Internet, 2010.

[15] G. G. Amatucci and N. Pereira. Fluoride based electrode materials for advanced energy storage devices. *Journal of Fluorine Chemistry*, 128:243 – 262, 2006.

[16] B. L. Ellis. et al. Positive electrode materials for Li-Ion and Li-Batteries. *Chemistry of Materials*, 22:691 – 714, 2010.

[17] K. M. Abraham and Z. Jing. A Polymer Electrolyte-Based Rechargeable Lithium/Oxygen Battery. *The Journal of the electrochemical society*, 143:1 – 5, 1996.

[18] T. Ogasawara. et al. Rechargeable Li_2O_2 Electrode for Lithium Batteries. *Journal of the American Chemical Society*, 128:1390 – 1393, 2006.

[19] S. D. Beattie. et al. High-Capacity LithiumAir Cathodes. *Journal of the Electrochemistry Society*, 156:A44 – A47, 2009.

[20] Aurlie Dbart. et al. α-MnO_2 Nanowires: A Catalyst for the O_2 Electrode in Rechargeable Lithium Batteries. *Angewandte Chemie International Edition*, 47:4521 – 4524, 2008.

[21] Rauh. R. D. et al. A Lithium/Dissolved Sulfur Battery with an Organic Electrolyte. *The Journal of the Electrochemistry Society*, 126:523 – 527, 1979.

[22] H. Yamin and E. Peled. Electrochemistry of a nonaqueous lithium/sulfur cell. *Journal of Power Sources*, 9:281 – 287, 1983.

[23] D. Peramunage and S. Licht. A Solid Sulfur Cathode for Aqueous Batteries. *Science*, 261:1029 – 1032, 1993.

[24] J. H. Shin and E. J. Cairns. N-Methyl-(n-butyl)pyrrolidinium bis(trifluoromethanesulfonyl)imide LiTFSI poly(ethylene glycol) dimethyl ether mixture as a Li/S cell electrolyte. *Journal of Power Sources*, 177:537 – 545, 2008.

[25] X. Ji. et al. A highly ordered nanostructured carbonsulphur cathode for lithiumsulphur batteries. *Nature Materials*, 8:500 – 506, 2009.

[26] F. Badaway. et al. Carbon Metal Fluoride Nanocomposites. *Journal of the Eletrochemical Society*, 150:A1318 – A1327, 2003.

[27] S.A. Needhama. et al. Synthesis and electrochemical performance of doped $LiCoO_2$ materials. *Journal of Power Sources*, 174:828 – 831, 2007.

[28] H. Li. et al. Reversible Formation and Decomposition of LiF Clusters Using Transition Metal Fluorides as Precursors and Their Application in Rechargeable Li Batteries. *Advanced materials*, 15:736 – 739, 2003.

[29] H. Li. et al. Li-Storage via Heterogeneous Reaction in Selected Binary Metal Fluorides and Oxides. *Journal of the electrochemical society*, 151:A1878 – A1885, 2004.

[30] I. Plitz.. et al. Structure and Electrochemistry of Carbon-Metal Fluoride Nanocomposites Fabricated by Solid-State Redox Conversion Reaction. *Journal of the electrochemistry society*, 152:A307 – A315, 2005.

[31] M. E. Gamboa-Aldeco J. O'M. Bockris, A. K.N. Reddy. *Modern Electrochemistry 2A: Fundamentals of Electrodics*. Kluwer Academic, 2000.

[32] A. J. Bard and L. R. Faulkner. *Electrochemical Methods: Fundamentals and applications*. Wiley and Sons, 2001.

[33] K.B. Oldham and J.C. Myland. *Fundamentals of electrochemical Science*. Academic Press, Inc, 1994.

[34] A.J. Mitter. *The structural and electrochemical dynamics of the electrode-electrolyte interphase of metal fluoride nancomposite positive electrodes for Li-Batteries*. PhD thesis, New Brunswick Rutgers, 2012.

[35] Y. Guo. et al. Nanostructured Materials for Electrochemical Energy Conversion and Storage Devices. *Advanced Materials*, 20:2878 – 2887, 2008.

[36] Y. Wang and G.Cao. Developments in Nanostructured Cathode materials for High Performance Lithium-Ion Batteries. *Advanced Materials*, 20:2251 – 2269, 2008.

[37] P. Bruce. et al. Nanomaterials for Rechargeable Lithium Batteries. *Angewandte Chemie*, 47:2930 – 2946, 2008.

[38] A. S. Arico. et al. Nanostructured materials for advanced energy conversion and storage devices. *Nature Materials*, 4:366 – 377, 2005.

[39] F. Jiao and P. G Bruce. Mesoporous crystalline β-MnO_2 a reversible positive electrode for rechargeable lithium batteries. *Advanced Materials*, 19:657 – 660, 2007.

[40] P. Balaya. et al. Nano Ionics in the context of lithium batteries. *Journal of Power Sources*, 159:171 – 178, 2006.

[41] M. Nonglak. et al. Size dependent Lithium miscibility gap in nanoscale $Li_{1-x}FePO_4$. *Electrochemical and solid-state letters*, 10:A134 – A138, 2007.

[42] M. S. Whittingham. Lithium batteries and cathode materials. *Chemistry Review*, 104:4271 – 4301, 2004.

[43] S. W. Oh. et al. Nanoporous structured $LiFePO_4$ with spherical microscale particle having a high volumetric capacity for lithium ion batteries. *Electrochemical and solid-state letters*, 12:A181 – A185, 2009.

[44] H. Ren. et al. Synthesis of $LiNi_{1/3}Co_{1/3}Mn_{1/3}$ as a cathode material for lithium battery by the rheological phase method. *Journal of Power Sources*, 177:439 – 444, 2008.

[45] B. J. Hwang. et al. Template free reverse micelle process for the synthesis of a rod like $LiFePO_4$ composite cathode material for lithium batteries. *Journal of Power Sources*, 194:515 – 519, 2009.

[46] E. Hosono. et al. Synthesis of single crystalline spinel nanowires for a lithium ion battery with high power density. *Nano letters*, 9:1045 – 1051, 2009.

[47] D. H. Kim and J. Kim. Synthesis of $LiFePO_4$ nanoparticles in polyyol medium and their electrochemical properties. *Electrochemical solid state letters*, 9:A439 – A442, 2006.

[48] C. Li. et al. Cathode materials modified by surface coating for lithium ion batteries. *Electrochimica Acta*, 51:3872 – 3883, 2006.

[49] L.J.Fu. et al. Surface modifications of electrode materials for lithium ion batteries. *Solid State Sciences*, 8:113 – 128, 2006.

[50] J. Maier. Nanosized mixed conductors. *Solid State Ionics*, 148:367 – 374, 2002.

[51] T. Li. et al. Reversible Three-Electron Redox behaviour of FeF_3 Nanocrystals as High-Capacity cathode-active materials for Li-Ion Batteries. *Journal of Physical Chemistry*, 114:3190 – 3195, 2010.

[52] H. Zhang. et al. Three-dimensional bicontinuous ultrafast-charge and -discharge bulk battery electrodes. *Nature Nanotechnology*, online publication:online, 2011.

[53] F. C. Bazito and R. M. Torresi. Cathodes for Lithium Batteris: The benefits of using nanostructured materials. *Journal of the Brazilian Chemical Society*, 17:4:627 – 642, 2006.

[54] P. G. Bruce. Energy storage beyond the horizon: Rechargeable lithium batteries. *Solid State Ionics*, 179:752 – 760, 2008.

[55] Multiple. *Lithium-Ion batteries Solid-Electrolyte Interphase*. Imperial College Press, 2004.

[56] Multiple. *Lithium-Ion batteries Solid-Electrolyte Interphase: Identification of Surface Films on Electrodes in Non-Aqueous Electrolyte Solutions: Spectrographic, Electronic and Morphological Studies*. Imperial College Press, 2004.

[57] Multiple. *Lithium-Ion batteries Solid-Electrolyte Interphase: The Cathode-Electrolyte Interface in a Li-Ion Battery*. Imperial College Press, 2004.

[58] Roland Berger Strategy Consultants. Powertrain 2020 - The Li-Ion Battery Value Chain Trends and implications. Technical report, Roland Berger Strategy Consultants, 2011.

[59] H. Arai. et al. Cathode performance and voltage estimation of metal trihalides. *Journal of power sources*, 68:716 – 719, 1997.

[60] H. Zhang. et al. Nanostructured nickel fluoride thin film as a new Li storage material. *Solid State Sciences*, 10:1166 – 1172, 2008.

[61] Z. W. Fu. et al. Electrochemical Reaction of Lithium with Cobalt Fluoride Thin Film Electrode. *Journal of the Electrochemical Society*, 152:E50 – E55, 2005.

[62] F. Cosandey. et al. EELS Spectroscopy of Iron Fluorides and FeF_x/C Nanocomposite Electrodes Used in Li-Ion Batteries. *Microscopy and Microanalysis*, 13:87 – 95, 2007.

[63] Y. Makimura. et al. Electrochemical behaviour of low temperature grown iron fluoride thin films. *Electrochemistry Communications*, 8:1769 – 1774, 2006.

[64] Y. Makimura. et al. Pulsed laser deposited iron fluoride thin films for lithium-ion batteries. *Applied Surface Science*, 252:4587 – 4592, 2006.

[65] N. Yamakawa. et al. Investigation of the Conversion Reaction Mechanisms for Binary Copper(II) Compounds by Solid-State NMR Spectroscopy and X-ray Diffraction. *Chemistry of Materials*, 21:3162 – 3176, 2009.

[66] R. E. Doe. et al. First-Principles Investigation of the Li-Fe-F Phase Diagram and Equilibrium and Nonequilibrium Conversion Reactions of Iron Fluorides with Lithium. *Chemistry of Materials*, 20:5274 – 5283, 2008.

[67] P. Poizot. et al. Nano-sized transition-metal oxides as negative-electrode materials for lithium-ion batteries. *Nature*, 407:496 – 499, 2000.

[68] Y. Li. et al. Mesoporous Co_3O_4 Nanowire Arrays for Lithium Ion Batteries with High Capacity and Rate Capability. *Nano letters*, 8:265 – 270, 2008.

[69] P. Liao. et al. A Mssbauer effect study of combinatorially prepared Al_2O_3/Fe and LiF/Fe multilayers. *Journal of Physics: Condensed Matter*, 20, 2008.

[70] H. L. Skriver and N. M. Rosengaard. Surface energy and work function of elemental metals. *Physical Review B*, 46:7157 – 7168, 1992.

[71] M. N. Obrovac and J. R. Dahn. Implications of finite-size and surface effects on nanosize intercalation materials. *Physical Review B*, 61:6713 – 6719, 2000.

[72] A. Van der Vena and M. Wagemaker. Effect of surface energies and nanoparticle size distribution on open circuit voltage of Li-electrodes. *Electrochemistry Communications*, 11:881 – 884, 2009.

[73] L. Wang. et al. First-principles study of surface properties of $LiFePO_4$: Surface energy, structure, Wulff shape, and surface redox potential. *Physical Review B*, 76, 2007.

[74] O. Delmer. et al. High temperature lithium cells using conversion oxide electrodes. *Journal of Applied Electrochemistry*, 40:1365 – 1370, 2010.

[75] N. Yamakawa. et al. Identifying the Local Structures Formed during Lithiation of the Conversion Material, Iron Fluoride, in a Li Ion Battery: A Solid-State NMR, X-ray Diffraction, and Pair Distribution Function Analysis Study. *Journal of the American Chemical Society*, 131:10525 – 10536, 2009.

[76] S. Grugeon. et al. An update on the reactivity of nanoparticles Co-based compounds towards Li. *Solid State Sciences*, 5:895 – 904, 2003.

[77] S. Laruelle. et al. On the Origin of the Extra Electrochemical Capacity Displayed by MO/Li Cells at Low Potential. *Journal of the Electrochemical Society*, 149:A627 – A634, 2002.

[78] P. Poizot. et al. Electrochemical reactivity and reversibility of cobalt oxides towards lithium. *COMPTES RENDUS DE L ACADEMIE DES SCIENCES SERIE II FASCICULE C-CHIMIE*, 3:681 – 691, 2000.

[79] A. Gmitter. et al. Formation, dynamics, and implication of solid electrolyte interphase in high voltage reversible conversion fluoride nanocomposites. *Journal of Materials Chemistry*, 20:4149 – 4161, 2010.

[80] Y. N. Zhou. et al. LiF/Co Nanocomposite as a New Li Storage Material. *Electrochemical and Solid State Letters*, 9:A147 – A150, 2006.

[81] J. Cabana. et al. Beyond Intercalation-Based Li-Ion Batteries: The State of the Art and Challenges of Electrode Materials Reacting Through Conversion Reactions. *Advanced Materials*, 22:E170 – E192, 2010.

[82] F. Badaway. et al. Carbon-Metal Fluoride Nanocomposites Structure and Electrochemistry of FeF_3:C. *Journal of the Electrochemical Society*, 150:A1209 – A1218, 2003.

[83] P. Lavela. et al. Elucidation of Capacity Fading on $CoFe_2O_4$ Conversion Electrodes for Lithium Batteries Based on Mssbauer Spectroscopy. *Journal of the Electrochemical Society*, 156:A589 – A594, 2009.

[84] J. Li. et al. Impact of Binder Choice on the Performance of α-Fe_2O_3 as a Negative Electrode. *Journal of the Electrochemical Society*, 155:A812 – A816, 2008.

[85] P. Poizot. et al. Searching for new anode materials for the Li-ion technology: time to deviate from the usual path. *Journal of Power Sources*, 97 - 98:235 – 239, 2001.

[86] S. Grugeon. et al. Combining Electrochemistry and Metallurgy for New Electrode Designs in Li-Ion Batteries. *Chemistry of Materials*, 17:5041 – 5047, 2005.

[87] E. Hosono. et al. The high power and high energy densities Li ion storage device by nanocrystalline and mesoporous Ni/NiO covered structure. *Electrochemistry Communications*, 8:284 – 288, 2006.

[88] Y. Yu. et al. Nickel-Foam-Supported Reticular $CoOLi_2O$ Composite Anode Materials for Lithium Ion Batteries. *Angewandte Chemie International Edition*, 44:7085 – 7089, 2005.

[89] J.L. Gmez-Cmer. et al. Precipitation of CoS vs Ceramic Synthesis for Improved Performance in Lithium Cells. *Journal of the Electrochemical Society*, 155:A189 – A195, 2008.

[90] H. Bryngelsson. et al. How dynamic is the SEI? *Journal of Power Sources*, 174:970 – 975, 2007.

[91] A. Dbart. et al. A Transmission Electron Microscopy Study of the Reactivity Mechanism of Tailor-Made CuO Particles toward Lithium. *Journal of the Electrochemical Society*, 148:A1266 – A1274, 2001.

[92] P. Poizot. et al. Rationalization of the Low-Potential Reactivity of 3d-Metal-Based Inorganic Compounds toward Li. *Journal of the Electrochemical Society*, 149:A1212 – A1217, 2002.

[93] R. Dedryvre. et al. Contribution of X-ray Photoelectron Spectroscopy to the Study of the Electrochemical Reactivity of CoO toward Lithium. *Chemistry of Materials*, 16:1056 – 1061, 2004.

[94] J.-T. Li. et al. XPS, time-of-flight-SIMS and polarization modulation IRRAS study of Cr_2O_3 thin film materials as anode for lithium ion battery. *Electrochimica Acta*, 54:3700 – 3707, 2009.

[95] G. Gachot. et al. Deciphering the multi-step degradation mechanisms of carbonate-based electrolyte in Li batteries. *Journal of Power Sources*, 178:409 – 421, 2008.

[96] Y. Zeng. et al. TG-MS analysis on thermal decomposable components in the SEI film on Cr_2O_3 powder anode in Li-ion batteries. *Ionics*, 15:91 – 96, 2009.

[97] A. Gmitter. et al. High Concentration Dinitrile, 3-Alkoxypropionitrile, and Linear Carbonate Electrolytes Enabled by Vinylene and Monofluoroethylene Carbonate Additives. *Journal of the Electrochemical Society*, 159:A370 – A379, 2012.

[98] A. J. Gmitter. *The Structural and Electrochemical Dynamics of the Electrode-Electrolyte Interphase of Metal Fluoride Nanocomposite Positive Electrodes for*

Li Batteries. PhD thesis, New Brunswick Rutgers, The State University of New Jersey, 2012.

[99] H. Lin. et al. The effects of quenching treatment and AlF_3 coating on $LiNi_{0.5}Mn_{0.5}O_2$ cathode materials for lithium-ion battery. *Materials Chemistry and Physics*, 119:519 – 523, 2010.

[100] C. B. Park. et al. Improvement of structural and electrochemical properties of AlF_3-coated $Li[Ni_{1/3}Co_{1/3}Mn_{1/3}]O_2$ cathode materials on high voltage region. *Journal of Power Sources*, 178:826, 2008.

[101] Sun. K. Y. et al. Significant improvement of high voltage cycling behavior AlF_3-coated $LiCoO_2$ cathode. *Electrochemistry Communications*, 8:821 – 826, 2006.

[102] J.-H. Kim. et al. Effect of aluminum fluoride coating on the electrochemical and thermal properties of $0.5Li_2MnO_30.5LiNi_0.5Co_0.2Mn_0.3O_2$ composite material. *Journal of Alloys and Compounds*, 10.1016/j.allcom.2011.11.117:Article in press, 2011.

[103] Website. Aluminium Fluoride, August 2011.

[104] Bervas. M. et al. Investigation of the Lithiation and Delithiation Conversion Mechanisms of Bismuth Fluoride Nanocomposites. *Journal of the electrochemical society*, 153:A799 – A808, 2006.

[105] Devine. T.M and Zhang. X. Identity of passive film formed on Aluminium in Li-Ion battery electrolytes with $LiPF_6$. *Lawrence Berkely National Laboratory*, 05, 2008.

[106] X. Zhang. et al. Corrosion of Aluminum Current Collectors in Lithium-Ion Batteries with Electrolytes Containing $LiPF_6$. *Journal of the Electrochemical Society*, 152:B448 – 454, 2005.

[107] S.S Zhang and T.R. Jow. Aluminium corrosion in electrolyte of Li-ion battery. *Journal of Power Sources*, 109:458 – 464, 2002.

[108] P. Atkins and J. De Paula. *ATKINS' Physical Chemistry*. Oxford University Press, 2006.

[109] C.C. Holmes. *Fourier Transform Infrared Spectroscopy*. Department of Physics and Astronomy, University of British Colombia, May 2011.

[110] University Of Iowa. SEM methodology. Website, 2012.

[111] Atomic World. Basic principle of transmission electron microscope, 2012.

[112] R. F. Egerton. *Physical Principles of Electron Microscopy*. Springer, 2005.

[113] Wikipedia. Selected Area Electron Diffraction, November 2012.

[114] B. Carr. et al. Nanoparticle Tracking Analysis Characterizes Biomaterials, November 2012.

[115] Z. Chena and J. R. Dahna. Reducing Carbon in $LiFePO_4$/C Composite Electrodes to Maximize Specific Energy, Volumetric Energy, and Tap Density. *Journal of The Electrochemical Society*, 149:A1184 – A1189, 2002.

[116] B. Y. Chang and S. M. Park. Electrochemical Impedance Spectroscopy. *The Annual Review of Analytical Chemistry*, 3:207 – 209, 2010.

[117] Q. Zhuang. et al. *Lithium Ion Batteries - New Developments*. InTech, 2012.

[118] Q. Zhang. et al. Carbon-coated fluorinated graphite for high energy and high power densities primary lithium batteries. *Journal of Power Sources*, 195:2914 – 2917, 2010.

[119] I. Mochida. et al. Anodic performance and insertion mechanism of hard carbons prepared from synthetic isotropic pitches. *Carbon*, 39:399 – 410, 2001.

[120] A. Jaiswal. et al. Nanoscale $LiFePO_4$ and $Li_4Ti_5O_{12}$ for High Rate Li-ion Batteries. *Journal of the Electrochemical Society*, 156:A1041 – A1046, 2009.

[121] Y. Li. et al. The improved discharge performance of Li/CF_x batteries by using multi-walled carbon nanotubes as conductive additive. *Journal of Power Sources*, 196:2246 – 2250, 2010.

[122] A.-L. Dalverny et al. Interface electrochemistry in conversion materials for Li-ion batteries. *Journal of Material Chemistry*, 21:10134, 2011.

[123] R. Doe et al. First Principles Study of the Li-Bi-F Phase Diagram of Bismuth Fluoride Conversion Reactions with Lithium. *Electrochemical and Solid State Letters*, 12:A125 – A128, 2009.

[124] Z. Wang. et al. *Diffusion and Reactivity of Solids*. Nova Science Publishers, 2007.

[125] N. Herron. et al. Preparation and Structural Characterization of Two New Phases of Aluminum Trifluoride. *Chemistry Materials*, 7:75 – 83, 1995.

[126] D.B. Shinn. et al. The Thermal Decomposition of Ammonium Hexafluoroferrate(III) and Ammonium Hexafluoroaluminate. A New Crystalline Form of Aluminum Fluoride. *Inorganic Chemistry*, 5:1927 – 1933, 1966.

[127] C. Alonso. et al. Preparation and Characterization of Different Phases of Aluminum Trifluoride. *Chemistry Materials*, 12:1148 – 1155, 2000.

[128] C.H. Barclay. et al. Reactivity of fluorinated γ-alumina and β-aluminium(III) fluoride surfaces towards hydrogen halides and tert-butyl chloride. *Journal of the Chemical Society, Dalton Transactions*, 1:40 – 47, 2002.

[129] E. Kemnitz. et al. Amorphous Metal Fluorides with Extraordinary High Surface Areas. *Angewandte Chemie International Edition*, 42:4251 – 4254, 2003.

[130] N. Herron. et al. Organic cation salts of the tetrafluoroaluminate anion. Yes, it does exist, and yes, it is tetrahedral. *Journal of the American Chemical Society*, 115:3028 – 3029, 1993.

[131] R.H. Hina. et al. Conversion of dichlorodifluoromethane with hydrogen over Pd/AlF_3 and Ru/AlF_3 prepared by solgel method. *Journal of Molecular Catalysis A: Chemical*, 207:27 – 33, 2004.

[132] Q. Wang. et al. Preparation and Electrochemical Performance of $LiFePO_4$-based Electrode Using Three-Dimensional Porous Current Collector. *International Journal of Electrochemical Science*, 7:8753 – 8760, 2012.

[133] L. Liu. et al. Excellent cycle performance of Co-doped FeF_3/C nanocomposite cathode material for lithium-ion batteries. *Journal of Materials Chemistry*, 22:17539 – 17550, 2012.

[134] United States Advanced Battery Consortium, November 2012.

[135] A. K. Padhi. et al. Phospho-olivines as Positive-Electrode Materials for Rechargeable Lithium Batteries. *Journal of the Electrochemical Society*, 144:1188 – 1194, 1997.

[136] A. V. Plakhotnyk. et al. Hydrolysis in the system $LiPF_6$ propylene carbonate - dimethyl carbonate H_2O. *Journal of Flourine Chemistry*, 126:27 – 31, 2004.

[137] R. Amin and J. Maier. Effect of annealing on transport properties of $LiFePO_4$: towards a defect chemical model. *Solid State Ionics*, 178:1831 – 1836, 2008.

[138] B. Kang and G. Ceder. Battery materials for ultrafast charging and discharging. *Nature*, 458:190 – 193, 2009.

[139] D. K. Kim. P. et al. Spinel $LiMn_2O_4$ Nanorods as Lithium Ion Battery Cathodes. *Nano letters*, 8:3948 – 3952, 2008.

[140] ePLBH. High energy product - General product specification, August 2011.

[141] F. Jiao. et al. Synthesis of Ordered Mesoporous Li-Mn-O Spinel as a Positive Electrode for Rechargeable Lithium Batteries. *Angewandte Chemie*, 47:9711 – 9716, 2008.

[142] G. Ceder. Identification of cathode materials for lithium batteries guided by first principles calculations. *Nature*, 392:334, 1998.

[143] G. Chen.et al. Improving the Performance of Lithium Manganese Phosphate Through Divalent Cation Substitution. *Electrochemical and solid-state letters*, 11:A190 – A194, 2008.

[144] G. Du. et al. Fluorine-doped $LiNi_{0.5}Mn_{1.5}O_4$ for 5 V cathode materials of lithium-ion battery. *Materials Research Bulletin*, 43:3607 – 3613, 2008.

[145] G. Wang. et al. One-dimensional nanostructures as electrode materials for lithium-ion batteries with improved electrochemical performance. *Journal of Power Sources*, 189:543 – 546, 2009.

[146] H. Wang. et al. Enhancements of rate capabilitynext term and cyclic performance of spinel $LiNi_{0.5}Mn_{1.5}O_4$ by trace Ru-doping. *Electrochemistry Communications*, 11:1539 – 1542, 2009.

[147] H.M. Wu. et al. Surface modification of $LiNi_{0.5}Mn_{1.5}O_4$ by ZrP_2O_7 and ZrO_2 for lithium-ion batteries. *Journal of Power Sources*, 195:2909 – 2913, 2010.

[148] H.M. Wu. et al. One-step synthesis $LiMn_2O_4$ cathode by a hydrothermal method. *Journal of Power Sources*, 161:1260 – 1263, 2006.

[149] W. F. Howard and R. M. Spotnitz. Theoretical evaluation of high-energy lithium metal phosphate cathode materials in Li-ion batteries. *Journal of Power Sources*, 165:887 – 891, 2007.

[150] J. Chen. et al. The hydrothermal synthesis and characterization of olivines and related compounds for electrochemical applications. *Solid State Ionics*, 178:1676 – 1693, 2008.

[151] J. W. Fergus. Recent developments in cathode materials for lithium ion batteries. *Journal of Power Sources*, 195:939 – 954, 2010.

[152] J.H. Kim. et al. Comparative Study of $LiNi_{0.5}Mn_{1.5}O_{4-\delta}$ and $LiNi_{0.5}Mn_{1.5}O_4$ Cathodes Having Two Crystallographic Structures: Fdm and $P4332$. *Chemistry Materials*, 16:906 – 914, 2004.

[153] J.R. Dahn. et al. Thermal stability of Li_xCoO_2, Li_xNiO_2 and 2-MnO_2 and consequences for the safety of Li-ion cells. *Solid State Ionics*, 69:265 – 270, 1994.

[154] K. Mizushima. et al. Li_xCoO_2 (0<x<-1): A new cathode material for batteries of high energy density. *Materials Research Bulletin*, 15:783 – 789, 1980.

[155] M. Konarovaa and I. Taniguchi. Synthesis of carbon-coated $LiFePO_4$ nanoparticles with high rate performance in lithium secondary batteries. *Journal of Power Sources*, 195:3661 – 3667, 2010.

[156] M. S. Whittingham. Materials Challenges Facing Electrical Energy Storage. *MRS Bulletin*, 33:441 – 456, 2008.

[157] M.M. Thackeray. et al. Lithium insertion into manganese spinel. *Materials Research Bulletin*, 18:461 – 472, 1983.

[158] Multiple. *Lithium Ion Batteries*. Kodansha Ltd and Wiley-VCH Verlag GmbH, 1998.

[159] N. L. Doan and I. Taniguchi. Cathode performance of $LiMnPO_4$/C nanocomposites prepared by a combination of spray pyrolysis and wet ball-milling followed by heat treatment. *Journal of Power Sources*, 196:1399 – 1408, 2010.

[160] Q. Iangffeng. et al. Template-Free Hydrothermal Synthesis of Nanoembossed Mesoporous $LiFePO_4$ Microspheres for High-Performance Lithium-Ion Batteries. *Journal of Physical Chemistry*, 114:3477 – 3482, 2010.

[161] Q. Zhong. et al. Synthesis and Electrochemistry of $LiNi_xMn_{2x}O_4$. *Journal of the Electrochemistry Society*, 144:205 – 213, 1997.

[162] R. Santhanam and B. Rambabu. Research progress in high voltage spinel material. *Journal of Power Sources*, 195:5442 – 5451, 2010.

[163] S. Yang. et al. Hydrothermal synthesis of lithium iron phosphate cathodes. *Electrochemistry Communications*, 3:505 – 508, 2001.

[164] S.-Y. Chung. et al. Electronically conductive phospho-olivines as lithium storage electrodes. *Nature Materials*, 1:123 – 128, 2002.

[165] S.H. Ye. et al. Improvement of the high-rate discharge capability of phosphate-doped spinel $LiMn_2O_4$ by a hydrothermal method. *Electrochemica Acta*, 55:2972 – 2977, 2010.

[166] Sun Qiang. et al. Synthesis and electrochemical performance of 5V spinel $LiNi_{0.5}Mn_{1.5}O_4$ prepared by solid-state reaction. *Transactons of Non Ferrous Metals Society of China*, 19:176 – 181, 2008.

[167] T. Ohzuku and R. J. Brodd. An overview of positive-electrode materials for advanced lithium-ion batteries. *Journal of Power Sources*, 174:449 – 456, 2007.

[168] W. Kleist. et al. A simple aqueous phase synthesis of high surface area aluminum fluoride and its bulk and surface structure. *Inorganica Chimica Acta*, 359:4851 – 4854, 2006.

[169] W. Weppner and R. A. Huggins. Determination of the Kinetic Parameters of Mixed Conducting Electrodes and Application to the System Li_34Sb. *Journal of the Electrochemical Society*, 124:1569 – 1578, 1977.

[170] Website. University of Cambridge, August 2011.

[171] Reuters Website. Reuters Industry Summits, August 2011.

[172] X. Huang. et al. Electrochemical performance of $LiFePO_4$ nanorods obtained from hydrothermal process. *Materials Characterization*, 61:720 – 725, 2010.

[173] X. Sun and C. A. Angell. Doped sulfone electrolytes for high voltage Li-ion cell applications. *Electrochemistry Communications*, 11:1418 – 1421, 2009.

[174] Y.-H. Chena. et al. Porous cathode optimization for lithium cells. *Journal of Power Sources*, 195:2851 – 2862, 2010.

[175] Y.-K. Sun. et al. Synthesis and Electrochemical Properties of ZnO-Coated $LiNi_{0.5}Mn_{1.5}O_4$ Spinel as 5 V Cathode Material for Lithium Secondary Batteries. *Electrochemical and Solid State Letters*, 5:A99 – A102, 2002.

[176] Wu Xu Deyu Wang, Jie Xiao and Ji-Guang Zhang, editors. *Investigation of $LiNiPO_4$ as a Cathode Material for Lithium Ion Battery*, 2009.